



**Mechanical behavior characterization of planar and non-planar  
sandwich composite panels with agglomerated cork core**

**Experimental and Numerical Study**

**Nuno Maia de Carvalho Soares**

Thesis to obtain the Master of Science Degree in  
**Aerospace Engineering**

Supervisors: Prof. Pedro Miguel Gomes Abrunhosa Amaral  
Prof. Nuno Miguel Rosa Pereira Silvestre  
Eng. Joel Roque Pinheiro

**Examination Committee**

Chairperson: Prof. Fernando José Parracho Lau  
Supervisor: Prof. Pedro Miguel Gomes Abrunhosa Amaral  
Member of the Committee: Prof. José Arnaldo Pereira Leite Miranda Guedes

**March 2017**



*To my parents,  
who always had nothing to give me everything.*



# Resumo

Pretende-se analisar o comportamento mecânico de uma estrutura compósita sanduíche laminada, cujo núcleo é aglomerado de cortiça reforçado com faces de fibra de vidro e resina epoxi. Painéis planos e não-planos são produzidos e é feita uma comparação entre o seu comportamento em ensaios de compressão e de vibração, considerando uma configuração específica baseada no projeto DesAIR. Foi desenvolvido um modelo numérico, para o qual as propriedades correctas para as faces e para o núcleo são determinadas analítica e experimentalmente. Com as propriedades correctas obtidas para efeitos de simulação, o modelo numérico foi progressivamente melhorado, enquanto painéis planos e não-planos foram produzidos e testados experimentalmente. Ensaios experimentais de compressão e vibração foram conduzidos e os resultados obtidos. Posteriormente, os resultados numéricos equivalentes foram obtidos através de uma análise de elementos finitos e após um estudo de convergência. Através da comparação das curvas de carga-deslocamento para o ensaio de compressão e dos modos e valores de frequência para o ensaio de vibração, pode-se facilmente concluir que o modelo numérico é válido. No entanto, o desvio inerente é relativamente alto para fins de engenharia, o que se deve a vários factores que ocorrem durante o processo de produção do painel e durante os testes experimentais, factores esses que não podem ser simulados com precisão pelo *software* de elementos finitos usado. Como desenvolvimentos futuros, o autor propõe a criação de um modelo estocástico a ser implementado no *software* de elementos finitos.

**Palavras-chave:** compósitos sanduíche laminados, painéis planos e curvos, núcleo de aglomerados de cortiça, comportamento mecânico, compressão, vibração, análise de elementos finitos.



# Abstract

This dissertation aims towards the mechanical behavior analysis of laminated sandwich composite structures, whereas the core is agglomerated cork reinforced with fiber glass and epoxy resin skins. Planar and non-planar panels are produced and a comparison between their behavior under compression and under vibration is performed, whereas a specific configuration based on the DesAIR project was used. A numerical model was developed, for which the correct properties for the skins and core were determined analytical and experimentally. With the correct properties obtained for simulation, the numerical model was progressively improved, while planar and non-planar panels were being produced and experimentally tested. Experimental compression and vibration tests were conducted and the results obtained. Afterwards, the numerical results were obtained through a finite elements analysis and after a convergence study. Through the comparison of the load-displacement curves for the compression test and of the modes and frequency values for the vibration test, one might easily conclude that the numerical model is valid. However, the inherent deviation is relatively high for engineering purposes, which is due to several factors that occur during the panel's production and during the experimental tests, factors those that cannot be accurately simulated by the used finite elements software. As future developments, the author proposes the creation of a stochastic model to be implemented on the finite elements software.

**Keywords:** laminated sandwich composites, planar and curved panels, agglomerated cork core, mechanical behavior, compression, vibration, finite elements analysis.



# Acknowledgements

To my supervisor Prof. Pedro Amaral and to my co-supervisor Prof. Nuno Silvestre for their immediate acceptance regarding my MSc. Dissertation, on which they have demonstrated care and interest right from the beginning. I am deeply grateful for all the advices that were given to me and for their outstanding availability for regular meetings, during the academic year and out of it. Their dedication to my research was remarkable.

To Eng. Joel Pinheiro at Frontwave Stone Technology for his valuable inputs and guidance throughout the entire work on this MSc. Dissertation, as well as for his outstanding and immediate availability while working fulltime at the company. My appreciation goes also to all the team at Frontwave Stone Technology for their unconditional support and expertise on the area.

To José Marcelino at Almadesign for all his support and for providing all the needed documents regarding the DesAIR project.

To Prof. Maria Emília Rosa at IST for her insight regarding cork's structure and manufacture process of its planks, and for generously providing me with bibliography on this subject.

To Carlos Diogo Henriques at IST for his help regarding the production of moulds on the CNC.

To Prof. Virgínia Infante at IST for her guidance regarding the mechanical testing on a INSTRON machine, from the preparation of the specimens for testing, to the further supervising and processing of the obtained raw data.

To Prof. André Carvalho at IST for his guidance regarding the vibrational testing of panels and for his interest and dedication on my research.

To Eng. Paweł Bujalski at MIT and to Eng. Guillermo Sánchez at Álava Ingenieros for all their practical information and help regarding the understanding of the VIC software provided by Correlated Solutions. Their contacts and expertise were crucial for the improvement of the strain values outputted from the VIC.

To António Duarte at IST for his help regarding the simulation using Abaqus 6.13®.

To my colleagues Filipa Correia, Gonçalo Gomes, João Ribeiro and Rodrigo Sequeira for the moments of discussion regarding each other's dissertation topic and also for the moments of joy, while working together at Frontwave Stone Technology. We will always remain as the Big5 Team.

To Tiago Baião for his help regarding Matlab.

Last, but not least, to my entire family and friends in Portugal and around the world, for all their unconditional love and dedication, particularly to my girlfriend, to my sister and to my parents.

To my girlfriend Gisela Cheoo for everything that we shared together and for being always there when I need. I could have never asked for a better person to have by my side!

To my sister for standing me, but always standing by me. Thank you for being always there.

To my parents, without whom I would be nothing! There are no words to express my gratitude for all that you have done for me and, if by any chance they were, they would never be enough. Obrigado! Amo-vos por tudo!



# Index of Contents

Resumo.....	iii
Abstract.....	v
Acknowledgements.....	vii
Index of Figures.....	xi
Index of Tables.....	xv
List of Symbols and Abbreviations.....	xvi
1. Introduction .....	1
1.1. Scope.....	1
1.2. Objectives .....	2
1.3. Organization .....	2
2. Literature Review .....	5
2.1. Sandwich composites.....	5
2.1.1. Components.....	5
2.1.2. Deformation and Failure Modes.....	6
2.2. Cork and cork core composites.....	8
2.2.1. Macroscopic structure .....	8
2.2.2. Microscopic structure .....	9
2.2.3. Extraction of cork and production of agglomerates .....	10
2.2.4. Mechanical properties.....	11
2.2.5. Engineering applications .....	13
2.3. The DesAIR Project.....	16
3. Experimental Tests.....	19
3.1. Materials and production method .....	19
3.2. Mechanical tests of the components.....	24
3.2.1. Determination of the skins properties.....	24
3.2.2. Determination of the core properties .....	28
3.3. Mechanical tests of the panels.....	34
3.3.1. Compression test.....	34
3.3.2. Vibration test.....	38
3.4. SEM Analysis .....	42
4. Numerical Simulation.....	43
4.1. Compression tests.....	43
4.1.1. FE mesh, support and loading conditions .....	43
4.1.2. Results and discussion .....	50
4.1.3. Comparison between the experimental and the numerical results.....	52
4.2. Vibration .....	54

4.2.1.	FE mesh, support and loading conditions .....	54
4.2.2.	Results and discussion .....	56
4.2.3.	Comparison between the experimental and the numerical results.....	58
5.	Conclusions.....	61
5.1.	Achievements.....	61
5.2.	Future developments .....	63
6.	Bibliographic References.....	65
7.	Appendixes .....	69
7.1.	Appendix A1 .....	69
7.2.	Appendix A2 .....	72
7.2.1.	Analytical Values .....	72
7.2.2.	Experimental Values .....	73
7.3.	Appendix A3 .....	77
7.3.1.	Experimental values .....	77
7.4.	Appendix A4 .....	81
7.5.	Appendix A5 .....	82
7.6.	Appendix A6 .....	83
7.7.	Appendix A7 .....	85

# Index of Figures

Figure 1: Sandwich construction with honeycomb core [2].....	5
Figure 2: Schematic representation of axial section of cork oak tree [9]. .....	9
Figure 3: Schematic representation of cork cells along the three corresponding directions [5].....	9
Figure 4: SEM images of natural cork cells in the radial (a) and tangential (b) sections, as well as corrugated cork cells (c) on the tangential section (adapted from [5]). .....	10
Figure 5: Microstructure of the cork cell wall (adapted from [5]). .....	10
Figure 6: Stress-strain curve obtained for cork along all directions and for a compression test [9].	12
Figure 7: Stress-strain curve obtained for cork along all directions and for a tensile test [9].....	12
Figure 8: ARD Rear-Cone TPS during construction (left) and after recovery (right), where the Norcoat-Liège tiles can be seen as respectively brown (natural colour) and black (burned material after re-entry) [17] [18]. .....	14
Figure 9: Schiaparelli, also known as the ExoMars Entry, Descent and Landing Demonstrator Module, being mated with the Trace Gas Orbiter (TGO), in the facility of Thales Alenia Space in France on 11 April 2015 [19]. .....	14
Figure 10: Schiaparelli's front heatshield (left) and rear heatshield (right), where the Norcoat-Liège tiles can be seen as brown (natural material colour) [23]. .....	15
Figure 11: The developed design concept for the DesAIR Project (adapted from [27]). .....	16
Figure 12: DesAIR Project moc-up, where the chosen curved panel configuration is highlighted, obtained from Solidworks® and directly provided by Almadesign company. ....	17
Figure 13: Side view of the 5 mm thickness CoreCork® NL20 agglomerate used. ....	19
Figure 14: Top view of the 300 g/m <sup>2</sup> glass fibers used.....	20
Figure 15: View of the epoxy resin 1050 and its hardener 1058S used.....	21
Figure 16: Flat panel (left) and curved panel (right) dimensions. As it can be seen, both panels have 450 mm of length and 225 mm of width and 6 mm of total thickness, from which 5 mm correspond to the core and 0.5 mm correspond to each one of the two skins. ....	22
Figure 17: Mould and counter-mould drawn on Solidworks®. ....	22
Figure 18: Mould and counter-mould production using the OUPLAN CNC Router Steel® model. ....	22
Figure 19: Exploded view of the curved panel configuration drawn in Solidworks®. ....	23
Figure 20: Example of one curved panel specimen before trimming (panel at the front) and one curved panel final specimen after trimming and sanding (panel at the back). ....	24
Figure 21: Specimen's dimensions (in mm) for the obtainence of the skins properties, drawn in Solidworks®. ....	25
Figure 22: Skins material specimens tangentially oriented, before (left) and after (right) the ink spraying. The same procedure was used for the axially oriented specimens. ....	25
Figure 23: First specimen T1 during (left) and after (right) the tensile test. ....	26

Figure 24: Specimen's dimensions (in mm) for the core compression properties, drawn in Solidworks®.....	29
Figure 25: Core material specimens sectioned for the compression test in all directions.....	29
Figure 26: First specimen R1 during the compression test.....	30
Figure 27: Specimen's dimensions (in mm) for the core tensile properties and for the radial direction (left) and for the tangential and axial directions (right), drawn in Solidworks®.....	30
Figure 28: Core material specimens sectioned for the tensile test in the radial direction (left) and in the tangential and axial directions (right).....	30
Figure 29: First specimen R1 during (left) and after (right) the tensile test.....	31
Figure 30: First specimen T1 during (left) and after (right) the tensile test.....	31
Figure 31: Comparison between the stress-strain curves obtained for the boiled cork (analytical curves) and for the cork agglomerate (experimental curves) under compression (left) and under tension (right).....	33
Figure 32: Comparison between the final stress-strain curves obtained for the boiled cork (analytical curve) and for the cork agglomerate (experimental curve), considering the compression and the tensile behavior.....	33
Figure 33: Dimensions (in mm) of the steel bar produced for the compression test. Created with Solidworks®.....	34
Figure 34: Steel bars produced for the compression test, where the tab grabbing area is highlighted.....	34
Figure 35: Level placed on the top of the upper tab for its horizontal levelling.....	35
Figure 36: Compression test set-up performed for the curved panel.....	35
Figure 37: Experimental curves for the compressive vertical load as a function of the compressive vertical displacement (RF2-U2 curves), obtained for the flat and the curved panels under a compression test.....	36
Figure 38: Face failure visible on both the flat (left) and the curved (middle) panels. Also, a section view on a flat panel is given (right), in which the face failure can be seen on the most fragile skin.....	38
Figure 39: Vibration test laboratory and respective set-up.....	39
Figure 40: Vibration test set-up and performed for the curved panel, where the LASER and shaker are visible.....	40
Figure 41: Schematics of the vibration test (considering a top view).....	40
Figure 42: Detailed view along the composite's thickness and under an amplification of $\times 45$ , where the cork cells impregnated with resin can be seen (inside of the white border), as well as the cork cells (outside of the white border). Impregnated resin can be identified on other cells on this image, even though on a smaller scale.....	42
Figure 43: Fitting of all the available hyperelastic models in comparison with the experimental test data curve. It is possible to see that the Ogden N5 curve is the one that best fits the Experimental curve.....	46
Figure 44: Material orientation axes, as seen in Abaqus 6.13® software and for the curved panel...	46

Figure 45: Diagram of forced acting on the block (left) and of the friction force as a function of F (right) [41].	48
Figure 46: Mesh with finite elements of 5 mm size, as seen in Abaqus 6.13® software and for the curved panel under a compression test.	49
Figure 47: Numerical model convergence verification for the flat (left) and for the curved (right) panels, where the finite elements size was reduced from 100 mm to 5 mm for both.	50
Figure 48: Vertical displacement U2 (left) and vertical load RF2 (right) for the flat panel and considering the last increment of the analysis. The size of the finite elements that compose the mesh is 5 mm.	51
Figure 49: Vertical displacement U2 (left) and vertical load RF2 (right) for the curved panel and considering the last increment of the analysis. The size of the finite elements that compose the mesh is 5 mm.	51
Figure 50: Total CPU time for the numerical finite elements analysis of both the flat and the curved panels, where the potency tendency curve can be seen for each one of both cases.	52
Figure 51: Comparison between the experimental and the numerical curves for the compressive vertical load as a function of the compressive vertical displacement (RF2-U2 curves), obtained for the flat and the curved panels under a compression test.	53
Figure 52: Special features used for the vibration test numerical model, as seen in Abaqus 6.13® software and for the curved panel. The punctual mass is placed on the reference point RP-1 and the soft springs are placed on the four edges with the four distinct CSYS referential.	55
Figure 53: Load-displacement curves obtained for three specimens of a Nylon fishing line and respective linear regressions (adapted from [42]).	55
Figure 54: Grid pattern used for the VIC-3D analysis.	70
Figure 55: VIC-3D analysis for one of the curved panel's specimens.	70
Figure 56: Stress-strain curves obtained for the tensile tested specimens oriented on the tangential axis (left) and on the axial axis (right).	74
Figure 57: Transversal strain-longitudinal strain curves obtained for the tensile tested specimens oriented on the tangential axis (left) and on the axial axis (right).	74
Figure 58: Stress-strain curves obtained for the specimens oriented 10° off the tangential axis (left) and 10° off the axial axis (right).	76
Figure 59: Stress-strain curves obtained for the specimens oriented on the radial axis (up, left), on the tangential axis (up, right) and on the axial axis (down, centre).	78
Figure 60: Average stress-strain curves obtained from Figure 59 and for each one of the three directions.	78
Figure 61: Stress-strain curves obtained for the specimens oriented on the tangential axis (left) and on the axial axis (right).	80
Figure 62: Average stress-strain curves obtained for each one of the three directions.	80
Figure 63: Amplitude (up) and phase (down) diagrams, obtained for the first flat panel specimen under a vibration test.	82

Figure 64: Amplitude (up) and phase (down) diagrams, obtained for the first curved panel specimen under a vibration test. ....	82
Figure 65: Analytical SEM Hitachi S2400 at IST's MicroLab [46]. ....	83
Figure 66: Overview along the composite's thickness next to the top skin and under an amplification of $\times 20$ and $\times 45$ , where the fibers, the resin and the cork cells are identified. ....	84
Figure 67: x axis translation (left) and x axis rotation (right), rigid body vibration modes for the flat panel. ....	85
Figure 68: y axis translation (left) and z axis rotation (right), rigid body vibration modes for the flat panel. ....	85
Figure 69: y axis rotation (left) and z axis translation (right), rigid body vibration modes for the flat panel. ....	85
Figure 70: 1 <sup>st</sup> (left) and 2 <sup>nd</sup> (right) vibration modes for the flat panel. ....	86
Figure 71: 3 <sup>rd</sup> (left) and 4 <sup>th</sup> (right) vibration modes for the flat panel. ....	86
Figure 72: 5 <sup>th</sup> (left) and 6 <sup>th</sup> (right) vibration modes for the flat panel. ....	86
Figure 73: 7 <sup>th</sup> (left) and 8 <sup>th</sup> (right) vibration modes for the flat panel. ....	86
Figure 74: z axis translation (left) and y axis translation (right), rigid body vibration modes for the curved panel. ....	87
Figure 75: x axis rotation (left) and x axis translation (right), rigid body vibration modes for the curved panel. ....	87
Figure 76: z axis rotation (left) and y axis rotation (right), rigid body vibration modes for the curved panel. ....	87
Figure 77: 1 <sup>st</sup> (left) and 2 <sup>nd</sup> (right) vibration modes for the curved panel. ....	87
Figure 78: 3 <sup>rd</sup> (left) and 4 <sup>th</sup> (right) vibration modes for the curved panel. ....	88
Figure 79: 5 <sup>th</sup> (left) and 6 <sup>th</sup> (right) vibration modes for the curved panel. ....	88
Figure 80: 7 <sup>th</sup> (left) and 8 <sup>th</sup> (right) vibration modes for the curved panel. ....	88

# Index of Tables

Table 1: Most common failure modes of sandwich composite structures (adapted from [2] [4]).	7
Table 2: Young's modulus values obtained for boiled cork planks in compression [5].	12
Table 3: Analytical and experimental skins properties obtained for the numerical model.	28
Table 4: Slope (m) and coefficient of correlation (R2) of the linear regression curves defined for each panel under a compression test.	36
Table 5: Experimental compressive vertical displacement (U2) values for increments of 500 N on the compressive vertical load (RF2). for the flat and the curved panels under a compression test.	37
Table 6: First frequencies of vibration (in Hz or cycles per time) obtained for the flat and curved panels tested, where 3 specimens were tested for each type of panel.	41
Table 7: Range of values for the coefficient of static and dynamic friction for dry and lubricated interfaces. Highlighted are the values used as base for the considered interface (adapted from [41]).	48
Table 8: Slope (m) and coefficient of correlation (R2) of the linear regression curves defined for each panel under a compression test and for a mesh of finite elements with 5 mm size. Results are shown considering the experimental (column A) and the analytical (column B) properties for the skins.	51
Table 9: Slope (K) and coefficient of correlation (R2) of the linear regression curves defined for each specimen.	55
Table 10: Numerical convergence verification for the first frequencies of vibration (in Hz or cycles per time) obtained for the flat panel, where the finite elements size was reduced from 100 mm to 5 mm. Highlighted are the divergence phenomena.	56
Table 11: Numerical convergence verification for the first frequencies of vibration (in Hz or cycles per time) obtained for the curved panel, where the finite elements size was reduced from 100 mm to 5 mm. Highlighted are the divergence phenomena.	57
Table 12: Comparison between the first frequencies of vibration (in Hz or cycles per time) obtained for the flat panels, where the deviation is shown, considering the experimental results as reference. Results are shown considering the experimental (column A) and the analytical (column B) properties for the skins.	59
Table 13: Comparison between the first frequencies of vibration (in Hz or cycles per time) obtained for the curved panels, where the deviation is shown, considering the experimental results as reference. Results are shown considering the experimental (column A) and the analytical (column B) properties for the skins.	59
Table 14: Properties of the matrix and the fibers, according to the manufacturers [32] [43] [44].	72
Table 15: Dimensions, weight and density calculation of the tangentially oriented specimens (T1 to T7) and of the axially oriented specimens (A1 to A7), sectioned for the skins material tensile	

test. The relative error for the calculated density is shown on the last column, by comparison with the analytical value of 1 169 kg/m <sup>3</sup> .....	73
Table 16: Young's Modulus (Ex) and Coefficient of Determination (R2) values obtained for each specimen and for both the tangential (up) and the axial (down) directions. Mean values are shown in the last column. ....	74
Table 17: Poisson's Coefficient (νxy) and Coefficient of Determination (R2) values obtained for each specimen and for both the tangential (up) and the axial (down) directions. Mean values are shown in the last column. ....	75
Table 18: Dimensions, weight and density calculation of the 10 <sup>9</sup> off the tangential axis oriented specimens (10oT1 to 10oT7) and of the 10 <sup>9</sup> off the axial axis oriented specimens (10oA1 to 10oA7), sectioned for the skins material tensile test. The relative error for the calculated density is shown on the last column, by comparison with the analytical value of 1 169 kg/m <sup>3</sup> . ....	75
Table 19: Shear Modulus (G) and Coefficient of Determination (R2) values obtained for each specimen and for both the tangential (up) and the axial (down) directions. Mean values are shown in the last column. ....	76
Table 20: Dimensions, weight and density calculation of the radially oriented specimens (R1 to R7), of the tangentially oriented specimens (T1 to T7) and of the axially oriented specimens (A1 to A7), sectioned for the core material compression test. The relative error for the calculated density is shown on the last column, by comparison with the analytical value of 200 kg/m <sup>3</sup> [29].....	77
Table 21: Dimensions, weight and density calculation of the radially oriented specimens (R1 to R7), of the tangentially oriented specimens (T1 to T5) and of the axially oriented specimens (A1 to A5), sectioned for the core material tensile test. The relative error for the calculated density is shown on the last column, by comparison with the analytical value of 200 kg/m <sup>3</sup> [29].....	79
Table 22: Dimensions, weight and density calculation of flat panel's (0-1 to 0-3) and the curved panel's (38-1 to 38-3) specimens, sectioned for the vibration and compression tests. The relative error for the calculated density is shown on the last column, by comparison with the analytical value of 361.50 kg/m <sup>3</sup> [29].....	81

# List of Symbols and Abbreviations

## Greek Symbols

$\alpha_i$	Material parameter
$\beta$	Linear mixture parameter
$\gamma_{10^\circ}$	Intralaminar shear strain measured on a 10° off-axis tensile test
$\gamma_{xy}$	Nominal shear strain on the xy-plane
$\varepsilon_{xx}$	Nominal strain on the longitudinal direction
$\varepsilon_{yy}$	Nominal strain on the transversal direction
$\theta$	Orientation angle of fibers in relation to the longitudinal direction
$\bar{\lambda}_1$	First principal stretch of the Cauchy-Green deformation tensor
$\bar{\lambda}_2$	Second principal stretch of the Cauchy-Green deformation tensor
$\bar{\lambda}_3$	Third principal stretch of the Cauchy-Green deformation tensor
$\lambda_m$	Coefficient of locking stretch
$\mu_i$	Material parameter
$\mu_s$	Static friction coefficient
$\mu_k$	Kinetic friction coefficient
$\nu_{xy}$	Poisson's coefficient
$\rho$	Density
$\sigma_m$	Maximum strength
$\sigma_x$	Nominal longitudinal stress
$\tau_{10^\circ}$	Intralaminar shear stress measured on a 10° off-axis tensile test

## Roman Symbols

$A$	Transversal area
$C_{ij}$	Material parameter
$d$	Machine displacement on the longitudinal direction
$D_i$	Material parameter
$E_x$	Young's modulus on the longitudinal direction
$f$	Volume Fraction of Fibers
$F_s$	Static friction force
$F_m$	Maximum static friction force
$F_k$	Kinetic friction force
$F$	Applied load or force
$G_{xy}$	Shear modulus
$\bar{I}_1$	First strain invariant of the Cauchy-Green deformation tensor

$\bar{I}_2$	Second strain invariant of the Cauchy-Green deformation tensor
$J$	Elastic volume strain
$K$	Spring stiffness
$l$	Length
$l_m$	Maximum strength elongation
$l_0$	Initial length on the longitudinal direction
$L$	Displacement
$m$	Slope
$N$	Normal force
$R^2$	Coefficient of determination
$t$	Thickness
$U$	Strain energy potential
$V$	Volume
$w$	Width
$W$	Weight

## Subscripts and Superscripts

$x$	Longitudinal direction or direction of loading
$y$	Transversal direction to the direction of loading
$z$	Axial or thickness direction
$i$	Matrix line
$j$	Matrix column
$M$	Matrix (epoxy resin 1050/1058S)
$F$	Fibers (glass fibers)
$C$	Composite
$s$	Skin
$c$	Core
$p$	Panel
$N$	Number of increments

## Abbreviations

A	Axial
ARD	Atmospheric Re-entry Demonstrator
ASTM	American Society for Testing and Materials
CNC	Computer Numerical Control
CPU	Central Processing Unit
DOF	Degree of Freedom
EDM	Entry, Descend and Landing Demonstrator Module

ESA	European Space Agency
FE	Finite Elements
FEA	Finite Elements Analysis
FOD	Foreign Object Damage
LASER	Light Amplification by Stimulated Emission of Radiation
LPF	Load Proportionality Factor
ODB	Output Database
PP	Polypropylene
PU	Polyurethane
PVC	Polyvinyl Chloride
R	Radial
RF2	Compressive Vertical Load
SFC	Specific Fuel Consumption
SEM	Scanning Electron Microscope
T	Tangential
TPS	Thermal Protection System
U2	Compressive Vertical Displacement
VIC	Video Image Correlation



# 1. Introduction

## 1.1. Scope

Humanity always had the need to improve the characteristics of the materials that were provided by nature and freely available in the environment. This first notion of composite material aroused around 1500 BC when early Egyptians and Mesopotamian settlers developed bricks for construction. These bricks consisted of a mixture of clay and sand, bounded together with chopped straw [1]. From this era on, composite materials have had an extreme development and, today, the search for new and improved composites is still one of the main quests in engineering. What might be regarded as a never-ending quest towards the best composite, is mainly due to their ability of improving needed mechanical properties while accurately decreasing weight. Lightweight but stronger materials are one of the main requisites for several fields, like aerospace and aeronautic, which has led to a major development of composites right from the end of the First World War.

Nowadays, the main reason for the continuous new composites research is the ratio between the high mechanical resistance and the reduced weight, due to their huge influence in the specific fuel consumption (SPC) of the vehicle. However, also several other composite's characteristics have to be taken into consideration. With the current technology, composites can be shaped into almost any desired design, that can be used to make the final products more or less aerodynamic, aeroelastic, etc. In addition, research is being conducted on the usage of new materials, which were never used before for this purpose and that have special characteristics for the needed applications, such as natural materials. For example, cork, when used as a core on a sandwich composite and when reinforced with for example glass fibers, presents several enviable properties, due to its cellular structure. Aside from the improved cellular properties of natural materials, their usage on composite structures also undertakes improved environmental performance, which is the key towards a sustainable future. So, cellular materials and particularly the proposed material, cork, could be used on the aerospace field as a substitute to the materials that are conventionally used as cores of sandwich constructions, which are mainly foams and aluminium honeycombs.

Therefore, being this sandwich composite material a rather new one and currently still under development, its fully mechanical behavior characterization is not yet easily available, such as it is for most metals, for example. Thus, due to the innovative character of the new sandwich configuration proposed for this dissertation, studies have to be conducted to properly characterize the materials used on it, because it would ultimately dictate in which way it could be used for the desired application. Apart from the innovative type of sandwich composite, also the type of structure to be analysed is a rather innovative one, which is a non-planar or curved panel. Thus, when one combines the analysis of a non-linear material, such as cork is, with the analysis of a sandwich composite which has this material as core and, ultimately, with the analysis of this composite as a non-planar structure, several innovative aspects in terms of engineering are being addressed simultaneously.

The type of sandwich composite structure object of the present dissertation, falls within the framework of the DesAIR Project, which is the result of a consortium of several entities: Almadesign, Amorim Cork Composites, Frontwave, Embraer, Couro Azul, INEGI and the University of Beira Interior UBI. Therefore, this thesis also provided the author with the opportunity of being part of this project and to be in contact with several companies and with the inherent technical challenges. Aside from what was stated, the biggest motivations for this dissertation are both the innovative character inherent to this recent topic, as well as the imminent future work that could be still further developed. Ultimately, the author hopes to awake the curiosity of the scientific community towards the several engineering applications of this sandwich structure, particularly on aerospace engineering.

## **1.2. Objectives**

This dissertation aims towards the experimental and numerical study of a lightweight sandwich composite structure, through its mechanical behavior characterization. The core of the sandwich is composed of agglomerated cork, a natural material with remarkable properties, and its skins are made of fiber glass and epoxy resin. The chosen structure is non-planar or curved, where also a planar or flat with the same dimensions and materials is analysed, for comparison purposes.

Regarding the experimental tests, tensile and compression tests were initially performed to characterize the mechanical behavior of the skins and the core material, in accordance with the respective ASTM standards. On a next phase, specimens of the final sandwich composite and both flat and curved panels were produced and compression and vibration tests were performed. This tests were selected due to their relevancy on the type of mechanical solicitations witnessed by the structure and for the further validation of the numerical model. Other relevant tests could have been made, such as tensile or bending tests.

Regarding the numerical simulation, three-dimensional finite elements models were developed using the software Abaqus 6.13®, to simulate the compression and the vibration tests performed experimentally. The main objective of the numerical study was the obtainence of the compressive vertical load-displacement curves and the determination of the first natural frequencies and modes of vibration for both panels, as well as a comparison between both. The concordance between the experimental and the numerical results was addressed since, once it can be verified and proven as valid, it allows for the usage of numerical models such as the one developed on this dissertation, to characterize the mechanical behavior of sandwich panels and even more complex structures, where natural origin materials with non-linear behavior are used as core.

## **1.3. Organization**

The present dissertation is divided into five chapters, where a brief description of each one's content is performed further on.

On the present chapter, *Chapter 1*, three sections are of interest. First, a brief introduction on the motivation to develop the proposed topic is performed, then the methodology and objectives are discretized and finally the organization of the document is shortly explained, at this section.

After the first introduction at *Chapter 1*, a literature review is performed on *Chapter 2*. This section starts with an overview on composites and laminated sandwich composites, where first the structure and the components of a sandwich panel are explained, followed by a description of its deformation and failure modes and mechanisms. Then, being the sandwich's core material cork agglomerate produced from cork planks, cork is widely described. A deeper importance is given to its mechanical properties under tension and compression, which are going to be relevant for further analysis. At the end of this section, cork's applications on the engineering field are referred. Due to this dissertation purposes, only the relevant applications are addressed, whereas a distinction is made between aeronautic and aerospace. An overview on history and several examples are mentioned for both. The DesAIR Project is introduced at the end of *Chapter 2*, from which the curved panel configuration and dimensions are taken, for the development of the desired cork core laminated composites.

At *Chapter 3*, the experimental analysis is performed. First the experimental procedure is described. All the used materials for the specimen's production are listed and their choice is justified. Then, the production method for the specimens is also explained, for both the flat and the curved panels. An explanation regarding the need for a small-scale test is also given. At the end of this section, a detailed explanation on the INSTRON machine, the VIC software and the correlation program is presented. After this, the experimental tests are performed. The first experimental tests given are the ones in which the material properties for the skins and the core are determined, for further accurate simulation purposes. These properties are determined analytically and by means of several experimental tests, using several specimens of each material. At the end, a comparison is performed for each one of them and the desired properties and curves are given. Finally, the experimental compression and vibration tests are performed. The procedure for the test is described in both cases and the results are shown.

At *Chapter 4*, the numerical non-linear analysis is performed. First, the general finite elements model is developed for both the flat and the curved panels, to reproduce the mechanical behavior of the specimens that were tested on the previous chapter. Materials, interactions between parts and border conditions are given and proper justified. After the general numerical model is obtained, the compression and vibration numerical tests are performed and the respective obtained results are shown. For both tests, a convergence and a computational time analysis are given. After the numerical results are obtained, a comparison is made between the results obtained experimentally at *Chapter 3* with the results obtained numerically at this *Chapter 4*. The validation of the finite elements model is justified and conclusions are undertaken.

Finally, overall conclusions that can be withdrawn from this dissertation are synthetized in *Chapter 5*, as well as some suggestions for further improvements on subsequent studies on the topic. The bibliographic references and the appendixes are given afterwards.



## 2. Literature Review

### 2.1. Sandwich composites

Sandwich composites are structures built up of two or more materials, whose properties are different, arranged as superposed layers and bounded by an adhesive element. This creates a new composite material with improved properties, when compared to the elements at their original state. Therefore, sandwich structures consist of a pair of thin, stiff and strong skins, separated by a thick and lightweight core, whose main function is to carry the loads from one skin to the other. The adhesive attachment that bounds these elements has the function of transmitting shear and axial loads from and to the core (*Figure 1*) [2]. The existence of the core between the two skins increases the moment of inertia of the panel without significant weight increases, which creates a panel that has in general more bending stiffness, buckling loads stiffness and specific mechanical strength, when compared to the core or skins material alone.

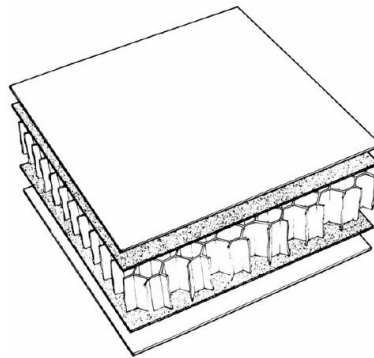


*Figure 1: Sandwich construction with honeycomb core [2].*

#### 2.1.1. Components

The components of a sandwich composite are the skins, the core and the adhesives and resins bonding process. Several materials can be used for each one of these components, according to the final composite's desirable properties, which will be further briefly described.

The **skins** (also known as faces, facings or covers) are relatively thin layers when compared with the sandwich's core and whose behavior is elastic, stiff and strong, since they are the only interface that protects the core from impact and other sorts of exterior damages. Also, due to this fact, usually the skins present a high surface quality finishing. Their purpose is to give shape to the sandwich composite and to carry tensile, compression and shear in-plane stresses. To withstand these stresses applied to the composite, normally a material with density and Young Modulus higher than the core is used. For this purpose, several materials are used as skins. For this purpose, fibers or fiber-reinforced plastics are the most widely used, like carbon or glass fibers. However, other materials (such as plywood) are used for this purpose and even metals (such as steel or aluminium alloys) are often usually used.

By opposition to the skins, the **core**'s main function is to carry the loads from one skin to the other, supporting them and preventing them from having an in-plane and out-of-plane displacement. Thus, since it does not carry most of the in-plane stresses, the core can be thicker and can have a much lower density when compared with the skins. The core might also provide thermal and acoustic isolation, as well as energy absorption during impact. Core materials might be classified into homogeneous (usually are foam cores) and non-homogeneous (usually are textile and pin cores, cup-shaped and corrugated cores and honeycomb cores).

Foam cores support homogeneously the composite skins, but their behavior under shear and compression loads is weak. Insulation properties of these cores are usually excellent and polyvinyl chloride (PVC), polyurethane (PU) and polypropylene (PP) are three of the most commonly used materials on this type of cores. Textile or pin cores provide a local support for the skins, with small production costs. These types of cores can be also combined with homogeneous cores to improve mechanical properties. However, this leads directly to higher production costs. Cup-shaped and corrugated have very small production costs. However, on the corrugation's transverse direction the mechanical properties are quite low, which precludes its usage for several applications. Honeycomb cores provide a bidirectional support for the skins, with average production costs. Due to their reduced weight and improved mechanical properties, when compared to the other non-homogeneous cores, honeycomb cores are the most commonly used for engineering applications. Aluminium is one of the most commonly used materials on this type of cores. Apart from this classification, the natural cores category arises. Natural materials usually have low densities and low production costs, due to their availability and easy extraction. Cork, balsa and bamboo are three examples of used materials on this type of cores.

The **adhesive** is the interface between the skin and the core material, which attaches both and serves as transition element, from which the loads are carried out and then dispersed. Usually, adhesives are liquid to allow for an easy incorporation during the production process. Polyurethane (PU) and epoxy are the most commonly used adhesives in sandwich construction.

### 2.1.2. Deformation and Failure Modes

A sandwich panel may fail according to several modes, whereas the most relevant and common ones will be referred, even though some other less common failure modes exist [2] [3].

**Face yielding** (*Table 1.A*) is a skin failure mode and it occurs when an axial load is applied to the top skin of the composite, which yields the skin if the axial stress reaches the in-plane strength of the material, leading to the occurrence of failure. The compressive face is usually the critical one [4].

**Intra-cell dimpling or buckling** (*Table 1.B*) is a skin failure mode and it is only applicable to cellular cores. It occurs when the skins are very thin and the cell size is large, which means that the honeycomb core may induce the skin buckling in the places where the core is unsupported. This buckling is then propagated across adjacent cells, inducing face wrinkling and leading to failure [2].

**Face wrinkling** (*Table 1.C*) is a skin failure mode and it is a buckling mode of the skin [2]. Buckling may occur either inwards the core (core compression failure) or outwards the core

(adhesive bond failure and later debonding), depending on the relative strengths of the core in compression and of the adhesive in flatwise tension.

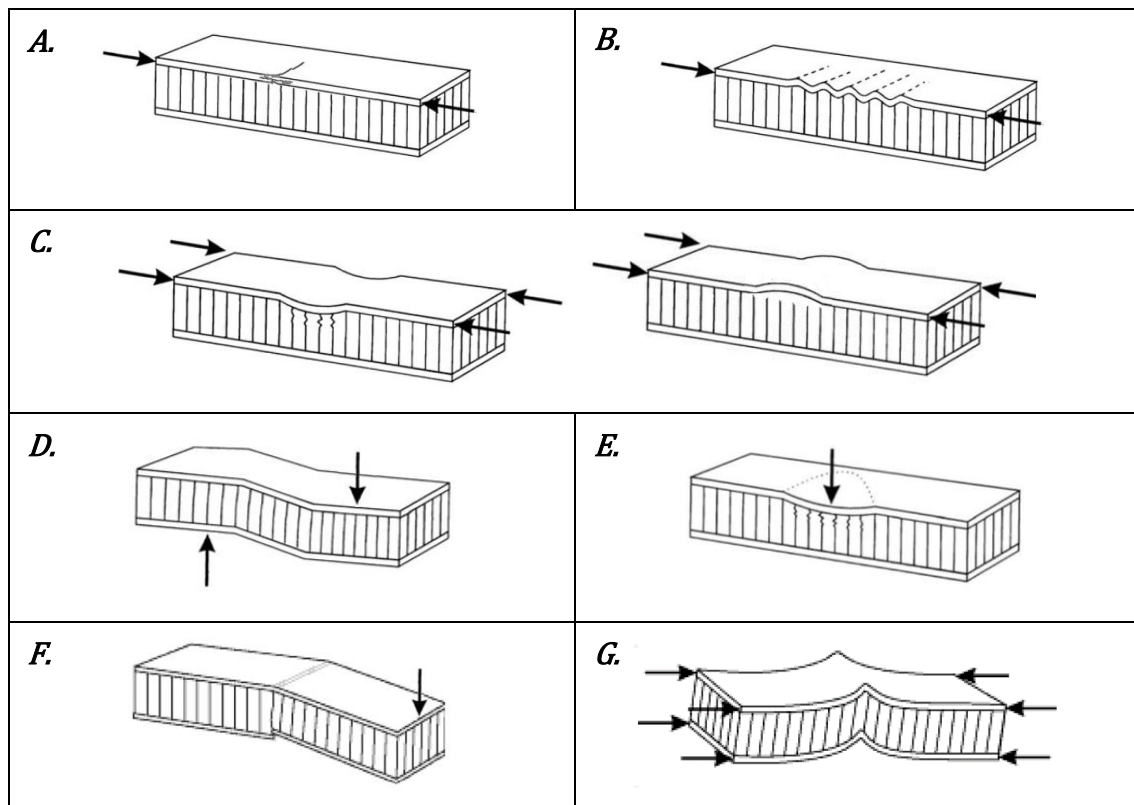
**Core transverse shear failure** (*Table 1.D*) is a core failure mode and it occurs when the shear strength of the core or the composite thickness are not enough. If the core is much thicker and pliable than the skins, the shear stress can be taken as linear through the face and constant in the core. Assuming brittle behavior, failure occurs when the applied shear stress equals the shear strength of the core [2]. Due to its anisotropy, low density cork cores are susceptible to this failure mode, since their shear strength varies according to the loading direction.

**Core crushing or local indentation** (*Table 1.E*) is a core failure mode and it occurs in point bending tests, for example, due to the indenter at the contact point. Failure occurs due to the local core crushing under the indenter, which happens when the compressive strength of the core material or the bending stiffness of the skin are too low. Local indentation differs from skin wrinkling because the top skin deflects after failure with a wavelength of the same scale as the indenter top skin contact length, whereas in skin wrinkling the deflection of the top skin has larger wavelengths [2].

**Face failure** (*Table 1.F*) occurs when the composite or the skin thickness, as well as the skin strength are insufficient, which may lead to failure in either the compression or the tension face.

**Panel or global buckling** (*Table 1.G*) occurs when either the composite thickness or the core shear stiffness are too low. Global buckling may lead to shear crimping, which is caused when either the shear modulus of the core material or the shear strength of the adhesive is low.

*Table 1: Most common failure modes of sandwich composite structures (adapted from [2] [4]).*



## 2.2. Cork and cork core composites

Cork (also known as suberose tissue or phellem) is a natural material obtained from the *Quercus suber L.* oak tree, from which it is periodically harvested, usually between 9 or 12 years and after a diameter of at least 25 cm is reached [5]. The cork tree is typical from the Western Mediterranean region, so it can be found in several regions of countries such as Portugal, Spain and Southern France, due to the specific climate conditions witnessed, such as a dry climate with high sunshine periods and low rainfall, but high humidity [5] [6]. Cork has a very important contribution to the economy and ecology of several Mediterranean countries, and its oak tree occupies a worldwide area of 2 139 942 ha, being Portugal the country with more percentage (about 34% of the world total), corresponding to an area of over 736 000 ha [7]. Portugal is the world leader in exportations in the cork sector and had a share of 63,9% in 2013, followed by Spain with 16,1% [7].

### 2.2.1. Macroscopic structure

The life cycle of the cork tree produces three type of suberose tissues: virgin cork, reproduction cork from second strip and reproduction cork from subsequent strips. However, there are several differences between the referred harvests. The virgin cork is irregular in structure, thickness and density and it is hard and rough, meaning that it is only suitable for boards, insulation, gaskets, shoe soles and other similar applications. The first reproduction cork is more regular but it still has insufficient quality for general applications. Just on the second reproduction cork and subsequent strips properties become consistent, which allows its usage for more accurate applications, such as stoppers production [5]. Therefore, trees must be from 15 to 30 years old before the first harvesting can occur and the maximum average biological age of the cork tree is approximately 200 years [8], which means that cork can be extracted approximately 15 to 20 times from the oak tree.

From the inner bark of the cork tree, suberose tissue is continuously created. This tissue is formed specifically by phellogen tissue, which has meristematic capability, meaning that it is responsible for the creation of new cells and for their further growth in the protoplasm [5]. Therefore, phellogen tissue continues to thicken and increasing the tree perimeter throughout the tree's life, even though this growth stops from October until April, which creates visible dark zones in the tissue (*Figure 2*). From April on, radial and axial growth starts simultaneously and cork is extracted when the growth is at its highest, i.e., during summer, when the phellogen is at its full meristematic activity allowing easy separation of the outer bark. Cork extraction affects the tree by decreasing the ring width, reducing its biological activity and the death of the newly exposed inner bark tissues, with formation of a new periderm approximately one month after cork is extracted [5].

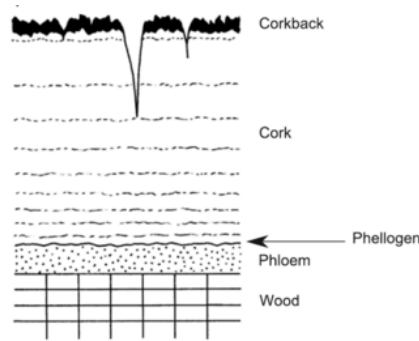


Figure 2: Schematic representation of axial section of cork oak tree [9].

### 2.2.2. Microscopic structure

The first time that the cork microscopic structure was observed under the microscope was in the middle of the XVII century, when Robert Hooke discovered the cells (empty spaces contained by walls), due to the examination of a thin cutting of cork [10]. However just after it was observed with the scanning electron microscope (SEM), its full microscopic structure could be known and it has revealed some interesting properties, which explain its behavior and therefore justify its several applications. Cork possesses an alveolar structure of closed cells with no empty spaces between them, similar to a honeycomb structure [5]. However, properties vary along the three directions in which cork cells are oriented, as well as the appearance of the cells (*Figure 3*).

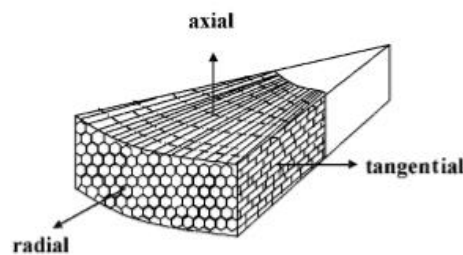


Figure 3: Schematic representation of cork cells along the three corresponding directions [5].

As one can observe from *Figure 3*, cork's cellular structure implies that it is an anisotropic material. However, and also due to the random orientation of the lateral cell walls (i.e., parallel to the radial direction), the axial and tangential directions can be considered as approximately equivalents, meaning that cork can be considered as a transversally isotropic material [5]. Cork SEM observation proved that, in the radial section, cells appear most frequently as heptagons, hexagons and pentagons (*Figure 4.a*). On the other hand, in the axial and tangential sections, cork cells are similar to a rectangle. However, in spite of the apparent rectangular shape, cells appear most frequently as hexagons (*Figure 4.b*). Typically, three cell wall edges meet at each corner [5]. A relevant characteristic of cork cells is that their cellular structure is always undulated on the base, but only corrugated on the lateral faces (*Figure 4.c*), with two or three complete corrugations per cell [5] [11]. This natural corrugation varies from almost straight to heavily corrugated or even collapsed and it is thought that they might result from compression during cellular growth. The later the cork is, the thicker and stronger the cell walls [5] [12]. This means that much less corrugation is observed.

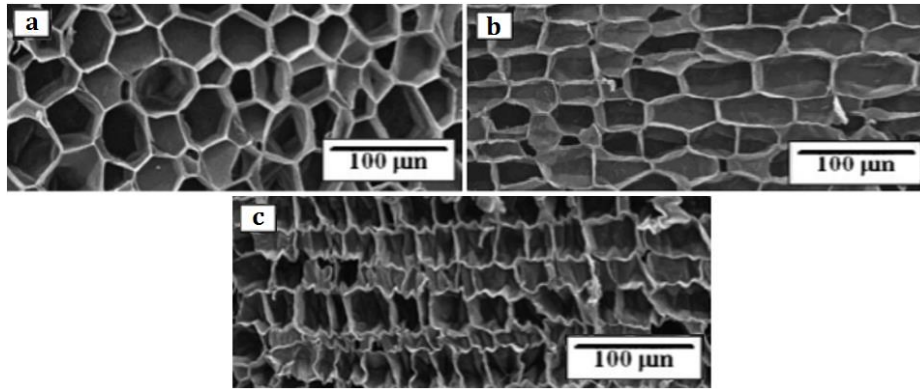


Figure 4: SEM images of natural cork cells in the radial (a) and tangential (b) sections, as well as corrugated cork cells (c) on the tangential section (adapted from [5]).

Cork cells are closed and hollow. The cell membranes are very thin and contain mostly suberin, lignin and cellulose [8], whereas their protoplasm contains cerin, fridelin, amorphous material and a large quantity of gas [5], presumably similar to air (Figure 5), which leads to a very low specific weight: it lengthens easily under stress and shortens when compressed.

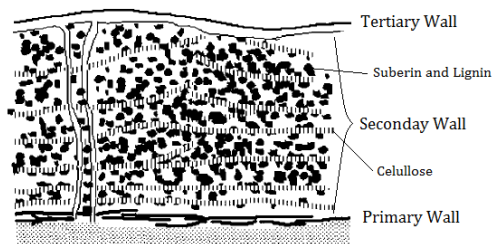


Figure 5: Microstructure of the cork cell wall (adapted from [5]).

### 2.2.3. Extraction of cork and production of agglomerates

The natural cork bark passes through a sort of different processes before it can be used for its several applications [12]. At the start of the process, natural cork is extracted as planks from the oak tree, normally during summer, and then gathered and stored in a warehouse. After this, the first step is to put the planks in water vapour for about one hour, which makes the cork cell walls relaxation and straightening of the bent planks [5]. With boiling it gets more pliable and the lenticels (which are unsuberized cells of cork cambium-gaseous exchange, i.e., the periderm, composed by cork cambium, cork and phelloderm) are fully expanded. Cork cells in the beginning are wrinkled and collapsed but, after boiling, the interior gas in the cells expands to create a very tight and uniform cell structure. After boiling, corrugation occurs. Then the boiled planks are trimmed into smaller, uniform and rectangular planks, which are then visually inspected and selected to guarantee the best appearance and properties [5]. Most of the sorting is done by hand into classes according to quality, thickness and size. The finest quality material will be used to make natural cork products like wine bottle stoppers and the poorer quality material will be ground and used to make agglomerated cork.

To produce agglomerated cork, waste cork passes through a machine in which it is broke into smaller pieces, which are then washed and dried. After this, they pass through successive

grinders to further reduce the cork particles size and, after another washing and drying process, they are screened and their size is uniformized. After the screening process, the agglomerated cork is produced by means of pressure and temperature application, in which adhesive agents are placed to bind the several small particles. After this process, pure and compound agglomerate cork can be produced. Pure agglomerated cork is formed by packing the particles into a mould and by making superheated steam at circa 300 °C flow inside the mould or by baking the mould at circa 250 °C for four to six hours [5]. After this process, the cork particles are bind together into a solid block by activating their natural resins. On the other hand, compound agglomerated cork is made by uniformly coating the cork granules with a thin layer of an additional adhesive agent. The coated cork granules are pressed into a mould and slowly heated, being the temperature dependent on the type of adhesive used [5]. After the blocks are removed from the mould, they are stacked together to allow air circulation. After this, the agglomerated cork blocks are cut for the needed application. For example, sheets may be cut from rectangular blocks.

#### **2.2.4. Mechanical properties**

Cork mechanical properties are quite unique. When compressed, the obtained cork stress-strain curve exhibits three different zones (*Figure 6*), typical from flexible cellular materials. The first zone goes from 0% until around 7% of the nominal strain and it corresponds to the linear elastic behavior, where the cell wall experiences elastic bending until the elastic collapse. At this point, the second zone starts and goes from 7% to around 70% of the nominal strain. At the beginning of this zone, the stress is almost constant but, due to the progressive buckling of the cell walls, the stress values rise as the nominal strain rises. Finally, the third and last zone is reached at around 70% of the nominal strain, where the material reaches the maximum stress value and the cell walls start to crush, which leads to a step rise on the stress-strain curve, due to their complete collapse [5].

When cork is compressed, different effects occur for different directions. When it occurs in the radial direction, the cell walls fold, the amplitude of corrugations increases and the cell bases perpendicular to the radial direction align, which results in a small and positive value for the Poisson's coefficient, due to this small expansion in the non-radial direction. On the other hand, when it occurs in the non-radial direction, the lateral cell walls bend and straighten. At high strains, the undulation pattern is inverted, which results in a negative value for the Poisson's coefficient, due to the shrinkage in the radial direction.

The thickness of the planks influences cork properties. Again, considering compression, planks with higher thickness show reduced compression strength. The higher Young's modulus values are obtained for medium thickness cork, independently of the considered direction (*Table 2*), which means that medium thickness planks are the ones with more strength. Smaller thickness planks have higher mechanical strength due to the larger proportion of late cork cells in thin planks, with more thick and less corrugated cell walls. By opposition, higher thickness planks have lower mechanical strength due to the cell dimensions differences and corrugation pattern [5]. When a plank

is under compression, the amplitude of corrugations rises until the cells walls collapse, whereas under tension, the amplitude of corrugations diminishes until the cell walls collapse.

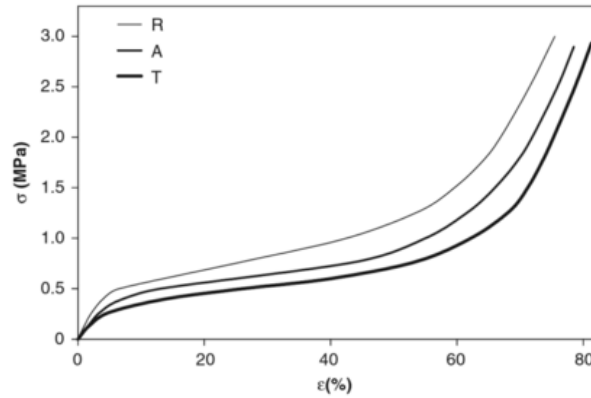


Figure 6: Stress-strain curve obtained for cork along all directions and for a compression test [9].

Table 2: Young's modulus values obtained for boiled cork planks in compression [5].

Cork Thickness	Radial Direction	Axial Direction	Tangential Direction
Small	11.5±1.0	10.9±0.6	8.6±0.7
Medium	13.2±0.7	12.0±1.5	9.6±1.4
Large	9.9±0.4	9.2±0.5	7.9±1.3

Heat treatment in air and in water, known respectively as heating and boiling, also influences cork properties. Considering the first, when a plank of cork is subjected to a temperature from 100 to 150°C for one day, due to the water loss, the compression strength of cork increases. However, when subjected to temperatures from 100 to 300°C during more than one day and up to two weeks, due to the thermomechanical degradation, the compression strength of cork is considerably reduced, also due to the specific Young's modulus reduction [5]. Considering now the second, water absorption softens the cell walls, which creates pressure differences between adjacent cells. This pressure gradient induces afterward tensile stresses, which then straighten the walls.

When tensioned, the obtained cork stress-strain curve exhibits a similar behavior for all the three directions (Figure 7). However, an intermediate region with oscillations often appears on the radial direction. This is due to the appearance of successive microscopic cracks that keep propagating across the surrounding cells, until this propagation is global [5].

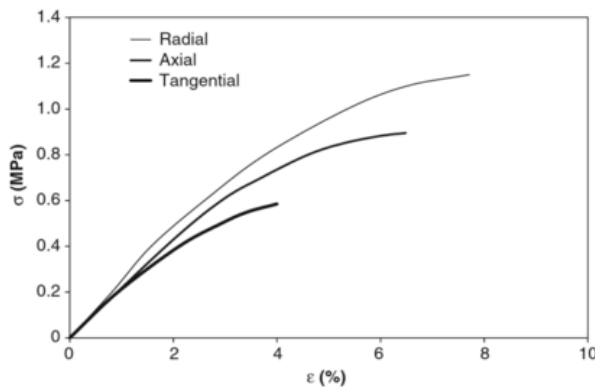


Figure 7: Stress-strain curve obtained for cork along all directions and for a tensile test [9].

## 2.2.5. Engineering applications

Composites with cork cores are progressively being seen as an alternative to other lightweight core materials usually used in aerospace applications, such as polymeric foam cores [13]. The use of cork as a core on a sandwich composite improves the final composite properties in terms of weight reduction, corrosion resistance and the capacity to withstand high mechanical loads, when compared with other similar materials. Thus, cork and cork core composites have a set of commonly known and widespread applications on the actual world, such as wine bottles stoppers and floor and wall coverings. It is also used on several other fields, such as in the sport field (it is mainly used in kayaks and surfboards, but its applications are far behind that), in the health field (it is used in vaccine adjuvants) and soon it might be even used in the defence field, due to its shock resistance [14]. However, despite all these shortly applications stated as examples, cork is also a sustainable material to be used in the aerospace and the aeronautical fields. Thus, due to this dissertation purposes, these specific applications will be carefully analysed on this section.

### *Aerospace Applications*

Regarding the space field of applications, cork core composites have been progressively more used on the last decades, due to their properties. In the space context, low weight purposes become even more relevant than in the aircraft context, since they might reduce substantially the launching cost. Being cork a lightweight material and also due to its capacity to withstand very high temperatures and also with vibrations attenuation, “cork agglomerates have been acting as a thermal protection system (TPS) ablative material in the form of tiles covering the most part of the vehicle” [13]. Therefore, cork agglomerates used as ablative materials protect the vehicle from high thermal energy sources, such as the Sun. Ablation is a combination of thermo-chemical and mechanical processes, which consume some TPS material present on the heat-shield surface, in order to dissipate the energy that would otherwise be absorbed as heat [15].

One of the first documented usages of cork as an insulation material for this application was for the space shuttle Columbia's external fuel tank, which was partly insulated by 225 kilograms of portuguese cork [16]. Later, other cork based materials were developed and used for TPS. One of this materials is known as Norcoat-Liège, which is constituted by hot-pressed cork particles agglomerated with phenolic resin and nowadays commercialized by the Airbus Group [13]. This material is manufactured in panels with thicknesses varying from 1 to 19 mm. Besides that, it has a density of 480 kg/m<sup>3</sup>, much lower than silica-based TPS materials (1600 kg/m<sup>3</sup>) and it supports high temperatures (2000 °C) and heat fluxes (5 MW/m<sup>2</sup>) [13].

The first space mission that used Norcoat-Liège as an ablative material was the Atmospheric Re-entry Demonstrator (ARD) developed by the European Space Agency (ESA), whose main purpose was to study the re-entry phase, in order to gather the maximum available data for further mission's developments [13] [17]. ARD was launched by an Ariane 5 rocket on 21 October 1998 and then later recovered on the Pacific Ocean [17]. Post-flight analysis was conducted and allowed the qualification of the TPS design and materials, in which Norcoat-Liège was included (*Figure 8*).

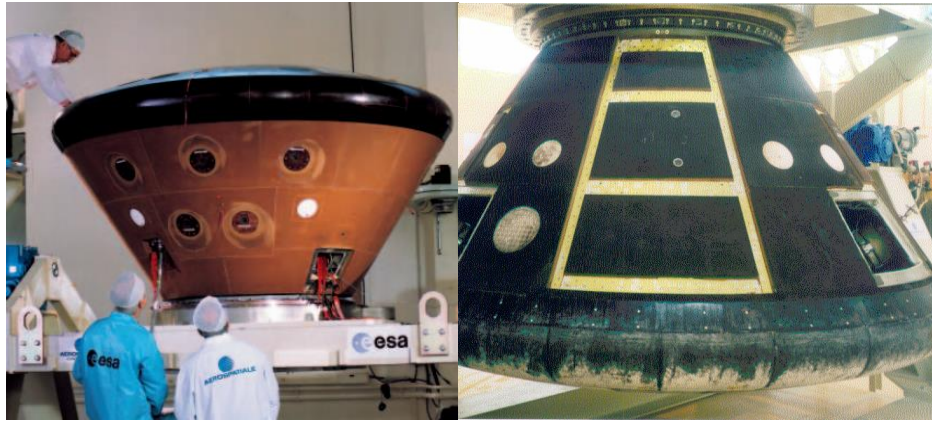


*Figure 8: ARD Rear-Cone TPS during construction (left) and after recovery (right), where the Norcoat-Liège tiles can be seen as respectively brown (natural colour) and black (burned material after re-entry) [17] [18].*

After the proven success of the Norcoat-Liège at the ARD mission, ESA has elected this material as the ablative material for the TPS of space vehicles. One of the most recent examples is the first mission of the ExoMars programme, which was launched on 14 March 2016 on a Proton Rocket, provided by the Russian Federal Space Agency (Roscosmos) [19]. This vehicle arrived on Mars in October 2016 and it consisted of a Trace Gas Orbiter (TGO) plus an Entry, Descent and Landing Demonstrator Module (EDM), known as Schiaparelli (*Figure 9*). Even though that the separation manoeuvre, the hypersonic atmospheric entry and the parachute phases of Schiaparelli's descent went according to plan, the EDM ended up crashing on the surface of Mars due to problems that occurred on the final phase of the descend and which are still being analysed. However, as one can see from the name TGO, the main objective of this mission was achieved with success, which was to search for evidences of methane and other trace atmospheric gases [20].



*Figure 9: Schiaparelli, also known as the ExoMars Entry, Descent and Landing Demonstrator Module, being mated with the Trace Gas Orbiter (TGO), in the facility of Thales Alenia Space in France on 11 April 2015 [19].*

Schiaparelli was protected from heat flux and deceleration by an aerodynamic heatshield. The front heatshield weighted 80 kg and it consisted of a carbon sandwich structure built by Airbus Defence and Space that was then covered with 90 tiles of the Norcoat-Liège material (*Figure 10*) [21]. On the other hand, the rear heatshield weighted only 20 kg and it consisted of 93 tiles of 12 different shapes, also built from the same material (*Figure 10*) [21]. Schiaparelli was separated from the TGO

on 16 October 2016 at 14:42 GMT and it entered the Martian atmosphere three days after with a velocity of circa 21 000 km/h [22]. Since the Norcoat-Liège heatshield can withstand temperatures up to 1 850 °C, the velocity was reduced until 1 650 km/h, by when the rear heatshield's parachute was deployed [22]. Even though the failure of this mission is still being analysed, experts say that probably the parachute's deployment occurred too soon, which then led to the free-fall of the EDM. However, until now, no issues were reported regarding the Norcoat-Liège material [22].

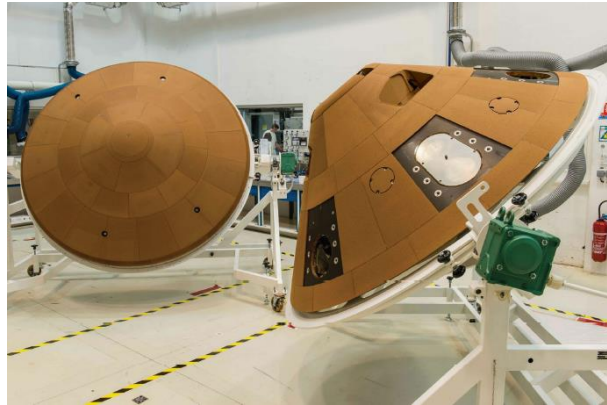


*Figure 10: Schiaparelli's front heatshield (left) and rear heatshield (right), where the Norcoat-Liège tiles can be seen as brown (natural material colour) [23].*

### ***Aeronautic Applications***

“Apart from space applications, little effort has been done towards the use of cork composites in high performance aircraft structural components” [13]. Nowadays, the state-of-the-art composite sandwich structures used in aircraft are made from synthetic foam cores or honeycomb materials, reinforced with carbon fibers and epoxy resin skins, because those materials offer high bending stiffness and are very lightweight [24]. However, they also radiate noise, which is not a desirable feature in an airplane, so the solution is to fill the interior with 100 to 150 mm of glass fabric, which then increases the weight of the structure and reduces the space inside the cabin [24]. Therefore, cork agglomerates arise as the ideal core material also for aeronautic applications.

However, just on the beginning of this decade some studies with cork core composite panels reinforced with epoxy resin were undertaken, as an alternative to both conventional cork agglomerates and high strength core materials usually used in aircraft [25]. Therefore, cork core composites reinforced with epoxy resin were submitted to several three-point bending tests, which shown that, when compared to other similar materials such as foams, their core shear stress limit was significantly better, which means that the crack propagation region is significantly reduced [25]. As one can easily conclude from this result, the usage of cork composites reinforced with epoxy resin is then an ideal material for aircraft applications and others, and it might be in the leading edge of several applications preferred materials [25].

As relevant for aircraft structures are impact tests, since several types of foreign object damage FOD are always imminent, such as bird and lightning strikes. Impact tests performed with the same composite material and further compared with the same similar materials suggested that there is an higher energy absorption capacity with minimum damage occurrence with cork core

reinforced with epoxy resin composites, which results in improved crashworthiness properties when impact loading is expected during service [13] [25]. Also, cork's properties and microscopic structure proportionate an excellent recovery capacity, which also verifies the observed results.

As well of major importance in aerospace applications, particularly in the already referred space field, are the thermal properties of the materials used. Therefore, thermal conductivity tests performed with the same composite material and further compared with the same similar materials suggested that the thermal insulating properties are good and similar to other type of core materials [25]. However, cork agglomerates with lower densities present better thermal properties, which is of major importance when considering the design of lightweight mechanical structures, such as aerospace components [25]. Another curious fact is that cork based composites have a higher ratio between the flutter speed and the mass of the panel, which means that this can be a lighter solution for the same problem and diminish the flutter of the structure [25]. Researchers at the University of Delaware claim they have achieved a 250% improvement in damping performance using cork-based materials, with no sacrifice in mechanical properties, when compared to the conventional used materials in the aircraft industry [24].

### 2.3. The DesAIR Project

DesAIR is a project that was officially presented on April 2015 and whose major aim is to develop new high performance composite solutions for aircraft interiors, with a wide range of applications and integrating natural materials through the development of specific manufacturing processes [26]. This project identified that the solutions currently used, such as reinforcement fibers with a thermosetting polymeric matrix, have several sustainability problems. Considering this, a coherent and systematic scientific approach was followed to obtain a sustainable solution based on the usage of a 100% natural, renewable and recyclable material as a core material: cork. The final solution is a product providing thermal, acoustical and vibration insulation, water resistance and recyclability. The material integration and manufacturing processes were then showcased in a business jet galley concept demonstrator (*Figure 11*) [27]. For the new concept development of this galley, several studies regarding the internal structure of the sandwich composite were performed and ergonomic and design studies were conducted. However, most of the performed studies regarded only the galley, its inserts and the floor, but not the four non-planar panels identified.

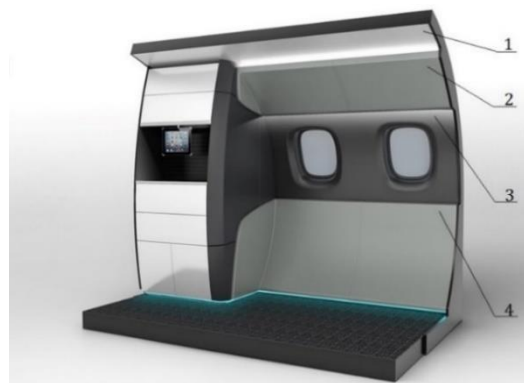


*Figure 11: The developed design concept for the DesAIR Project (adapted from [27]).*

Thus, one of the main objectives of this dissertation will be the mechanical behavior analysis of one of these non-planar panels. According to this dissertation requirements, all the referred panels indexed from 1 to 4 on *Figure 11* will be laminated sandwich composite structures, in which the core is made of agglomerated cork and the skins of glass fibers and epoxy. Considering the conceptual model of the galley provided by Almadesign, through the Solidworks® program, for example, the moc-up was analysed (*Figure 12*). After a careful analysis of the Solidworks® model, the final panel to be studied was selected, which is the one identified by number 4 on *Figure 11* and highlighted on *Figure 12*. After the chosen panel's dimensions were taken and after its configuration was carefully discussed and analysed, two simplifications must be done for the experimental tests to be possible.

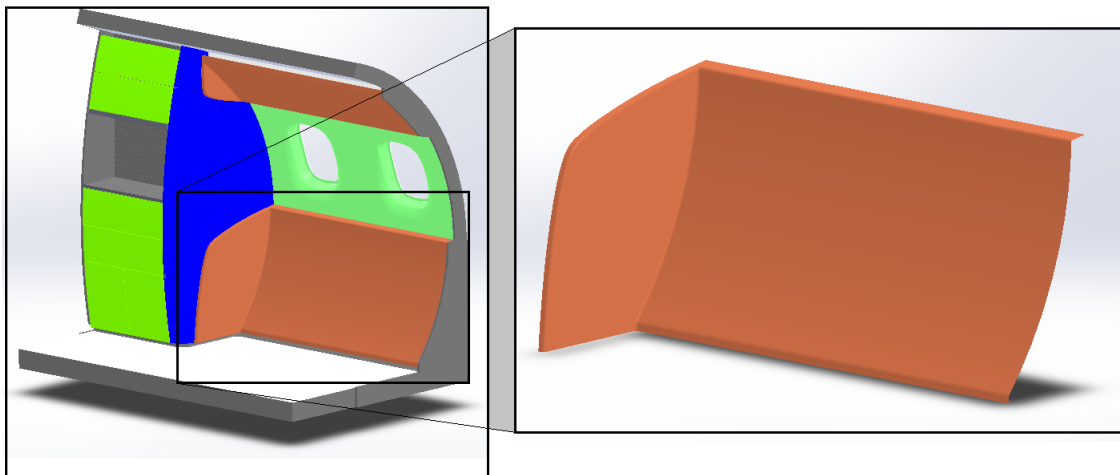


*Figure 12: DesAIR Project moc-up, where the chosen curved panel configuration is highlighted, obtained from Solidworks® and directly provided by Almadesign company.*

The first simplification is due to the INSTRON machine in which the non-planar panel will be tested and whose dimensions are reduced comparing to the entire panel's length and width. So, a reduced scale test has to be performed, meaning that the panel's length and width have to be reduced proportionally to a configuration that fits the testing machine's dimensions. The second and last simplification is because the non-planar panel has more than one curvature radius, which means that it is curved multiple times towards different axes, as it can be seen at *Figure 12*. Thus, only one curvature will be considered for the chosen non-planar panel configuration. This curvature will be the one that follows the curvature of the plane's fuselage, if one considers the galley as inserted on it. More details about these two simplifications will be discussed at *Chapter 3*.

This dissertation pretends to test the behavior of the referred sandwich composite under compression and to perform also a vibration analysis. For both the compression and the vibration analysis, experimental tests will be performed at the laboratory and a finite elements analysis will be carried out for both tests. The main objective of this dissertation is the numerical model development and its validation by means of the experimental tests performed.



## 3. Experimental Tests

### 3.1. Materials and production method

Regarding the application on the DesAIR Project, one has to see that the main requirement is for the final structure to be as much lightweight as possible. Even though other factors have also to be considered (such as cost, final properties and availability, for example), the most relevant factor is indeed the weight of the final curved panel. Furthermore, even though it would be of interest to study the different properties of the curved panel and its behavior for different possible configurations and materials, this is not the purpose of this dissertation. Thus, the final sandwich structure to be analysed will use cork agglomerate, glass fibers and epoxy resin as materials. Then, the purpose of this section is to state the specific type of materials used, giving a brief justification regarding the DesAIR Project given requirements.

Regarding the type of agglomerated cork used for the sandwich panel core, the CoreCork® material from Amorim Cork Composites [28], also part of the DesAIR Project Consortium, was used. This material consists of a cork agglomerate and currently exist several variants on the market. The chosen CoreCork® material was the NL20, which has a percentage of polyurethane resin of less than 10% in weight [29]. To justify the choice of this material, one has to know the differences between the numbers that follow the NL acronym. Those numbers refer to the density of the material, meaning that lower numbers have lower densities, when compared with higher numbers (for example, a NL10 core has a density of 120kg/m<sup>3</sup> and a NL20 has 200kg/m<sup>3</sup>). So, the ideal choice for a lightweight application such as this one, should be choosing NL10. However, since the resin uptake for NL10 is 270g and for NL20 is 170g (per m<sup>2</sup> at 1 mm thickness), this means that a NL20 core absorbs approximately 2/5 less resin than a NL10. Therefore, the final weight using NL10 would also be increased, which decreases its shear resistance due to the known fragile behavior of the resin. Thus, the best choice is the CoreCork® NL20 material, with a thickness of 5 mm (*Figure 13*).



*Figure 13: Side view of the 5 mm thickness CoreCork® NL20 agglomerate used.*

Regarding the materials used for the sandwich curved panel skins, glass fibers and epoxy resin were the ones used.

Concerning the type of chosen fibers, glass fibers from Hexcel [30] were used, since they are the most common type of fiber and used for several applications, particularly due to their warpage and creep reduction, which is more evident at high temperatures. Fibers are evaluated in terms of number of layers, type and grammage. Starting with the number of layers, just a layer of glass fiber

was used for both sides skins, because the curved panel studied is not a main structural element, so the resistance needed to fulfil the requirements can be achieved with only a fiber layer, since the addition of further layers would also increase the cost and weight with no direct relevant benefits. Regarding the fiber type, the fabric used for this application was a 2×2 twill woven fabric. These woven fabrics are made on looms in a variety of weights, weaves and widths and they provide good strength in the roving axial orientation (0°/90°). However, the tensile strength of woven fabrics is a bit compromised because fibers are crimped as they pass over and under one another during the weaving process (i.e., under tensile loading these fibers tend to straighten and that causes stresses within the matrix system). Several different types of weaving are used for bidirectional fabrics, from plain weaves to harness, satin or twill weaves. This last type of weave will be used since these weaves tend to be more drapable than the others. Regarding the grammage, it is a measure of thickness and density, expressed in gram per square metre, and it is directly proportional to the resin absorption. For this experiment, a woven fabric with 300 g/m<sup>2</sup> was used, since good composite mechanical properties are already achieved with this fiber, which means that, even though the properties would be improved by using for example 600 g/m<sup>2</sup> fibers, the relationship cost-benefit would make this option unacceptable. With higher grammage fibers, more resin needs to be used and, consequently, the weight of the final structure also increases. For example, if 600 g/m<sup>2</sup> fibers are used instead of 300 g/m<sup>2</sup>, the resin that needs to be used duplicates and the final weight of the final fiber and resin structure quadruplicates. Thus, 300 g/m<sup>2</sup> 2×2 twill woven fabric glass fibers were used (*Figure 14*).



*Figure 14: Top view of the 300 g/m<sup>2</sup> glass fibers used.*

Concerning the type of chosen resin, epoxy resin from Resoltech [31] were used, in particular the epoxy resin 1050, hardened with the epoxy resin 1058S (*Figure 15*). Considering a 16 hours cycle at 60°C and taking a closer look at the properties of the several 1050 epoxy resin types, one can easily observe that the hardener 1059S is the only one that has a set of properties better than the 1058S [32]. However, according to the chosen application, glass temperatures of more than 50°C will not be reached in normal cases and will be even hard to reach in emergency ones, so both hardeners are similar in this parameter. Regarding the flexion test, 1058S is more rigid than 1059S, which translates physically in less elongation measured on the panel, being its maximum strength lower. This is an advantage, since the vibrations witnessed by the panel will be inferior, so this resin will be used. Since the method of spreading resin is by hand lay-up and regarding that the gel time, which is the time that takes for the viscosity to duplicate, is 10 minutes for 1059S and almost the double for 1058S, 1058S was used, since it gives more time for the resin hand lay-up process [31].



*Figure 15: View of the epoxy resin 1050 and its hardener 1058S used.*

According to the type of fiber and resin, there is an ideal relationship between the quantities of resin to the used for the chosen fiber, which varies from 50% to 70% of the total weight. If the quantity of resin used is too low, then dry zones around the fibers are more easily created and the efforts are carried out towards the longitudinal direction. In addition, if the quantity of resin used is too high, then fragile zones are more easily created between the cracks, fastening their propagation, since the resin is more fragile than the fibers. Taking for example the prepregs, since they are uniform due to their pre-impregnation production method, the proportion of resin used during production is around 50% of the total weight. On the current hand lay-up method, since the uniformity achieved is not as good as it is for the prepregs, the proportion of resin used has to be always around 65% of the total weight, because it is better to have more resin on the final composite than dry zones. To consider also the resin that is lost and stays in the cup after the mixing of the epoxy resin 1050 with the epoxy resin hardener 1058S, the final percentage of resin that will be considered throughout all the experiments will be 68% of the total weight.

Knowing the different materials that will be used to produce the sandwich composite structure, before a detailed explanation regarding the production method, it is important to refer some relevant facts. First, the real dimensions of the chosen panel to be studied (which is the one identified by number 4 on *Figure 11*) are too big to fit the machines in which the tests will be performed. Therefore, real-scale tests cannot be performed, so the dimensions have to be reduced in order for small-scale tests to take place and for accuracy not to be lost. Being said, the moc-up panel dimensions were reduced by a scale of 1:3, which correspond to the further simulation and testing dimensions configuration (*Figure 16*). After the panel dimensions are known, it is important to refer that one of the objectives of this thesis is to compare the curved panel configuration with the flat panel. Therefore, several flat and curved panels were produced, according to *Figure 16* dimensions.

For the flat panels, their production is possible by just following the experimental procedure that will be explained further on. However, for the curved panels, their production is strongly dependent on the production of a mould and a counter-mould, where the various sandwich composite layers could be then laid upon and where pressure could be then further applied. Thus, for this purpose, two moulds were produced on the OUPLAN CNC Router Steel® model [33], whereas the milling material chosen was a bluish green board of extruded polystyrene foam, also known as XPS. This was the chosen material because it is recommended for people new to milling and for most

surface milling jobs. Also, the fact that it is inexpensive, lightweight and mills quickly with rather inexpensive tools, made this material the best choice for these moulds. It is important to refer that, using this material for the moulds, problems were not noticed during the several composite production phases, not even during the most critical phase, which is when pressure is applied. Thus, XPS is one of the best choices for these moulds production. Having this settled, Solidworks® models for the mould and counter-mould were created (*Figure 17*) and then converted through ArtCAM Pro 8.1®, for them to be read by the CNC machine. Then, both the roughening and the finishing were performed using a specific FF15 ball-nose 2-fluted milling cutter (DIN 327/L) with HSS-Co 8% material, 12 mm of diameter and 110 mm of length. After the finishing process, the mould and the counter-mould were obtained (*Figure 18*) and, on this stage, the composite is ready to be produced.

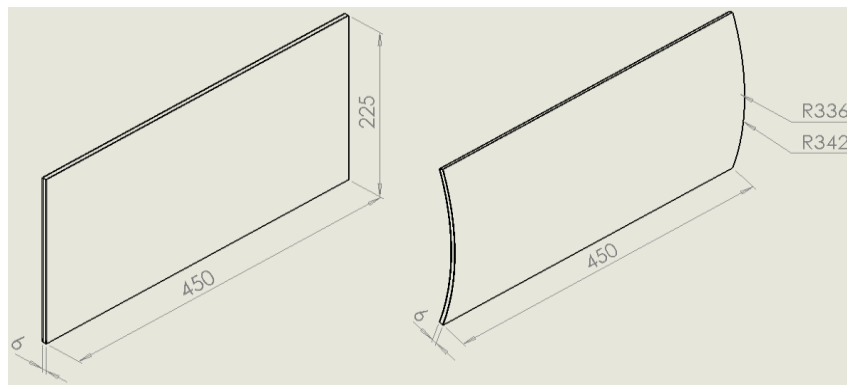


*Figure 16: Flat panel (left) and curved panel (right) dimensions. As it can be seen, both panels have 450 mm of length and 225 mm of width and 6 mm of total thickness, from which 5 mm correspond to the core and 0.5 mm correspond to each one of the two skins.*

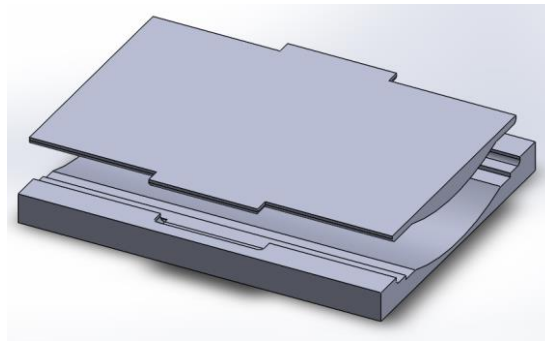


*Figure 17: Mould and counter-mould drawn on Solidworks®.*

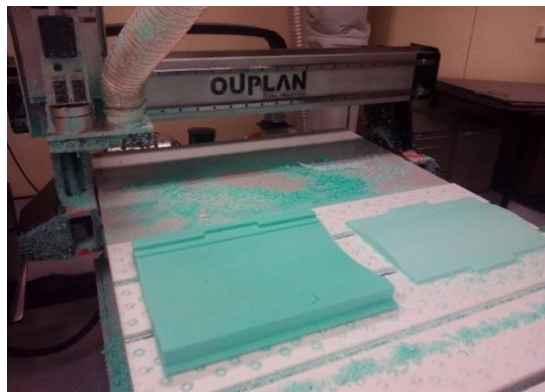


*Figure 18: Mould and counter-mould production using the OUPLAN CNC Router Steel® model.*

For the production of the sandwich composite specimens, the only method that was used was the hand lay-up process, since it is the simplest and oldest open moulding method, even though it is a labour-intensive process. For this process, the room temperature where the composite is going to be made was set at approximately 25 °C and at a relative humidity level of approximately 50%. When these requisites are met, then the lamination process can start. Since the layer's superposition is the same for both the flat and the curved panels, the production process is identical. The only relevant difference is the need for a mould for the curved panel, as it was already explained. Therefore, for the next description, it will only be explained the curved panel production process. To start with this explanation, first it is useful to observe *Figure 19*, where an exploded view from the layer's superposition can be seen, as well as the chosen axes directions, that will be used as reference for further analysis from this point on.

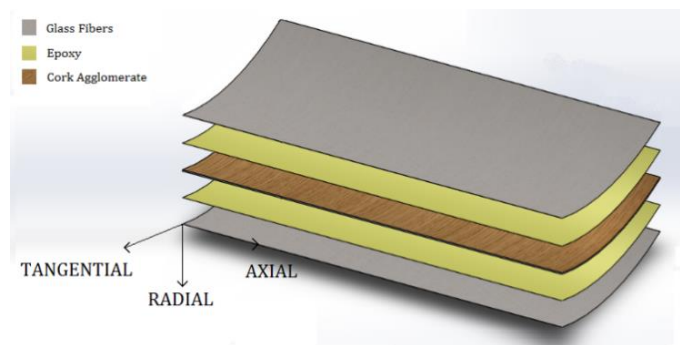


*Figure 19: Exploded view of the curved panel configuration drawn in Solidworks®.*

Back to the hand lay-up process, first the needed quantities of resin must be weighted. Thus, the quantities of epoxy resin 1050 and hardener 1058S are computed according to the length and width of the final composite and according to the grammage of the glass fibers, considering also the matrix resin uptake of 220 g/m<sup>2</sup>. Then these two quantities are weighted on a digital scale and mixed together using a spatula during less than one minute. When homogenization is finally achieved, the resin is ready to be poured onto the glass fibers already laid on the negative mould placed on the table. After the resin is poured on the glass fibers and the outer skin of the final composite is done, then the cork matrix is laid upon and the same procedure is repeated for the inner skin. Then the positive mould is laid on top of the negative mould, with all the previous composite layers inside. This hand lay-up process has to be performed in about 19 minutes [32], since it is the gel time of the used resins, which is more than enough time for it to be performed carefully. The gel time is the time that takes for the mixture to be incapable of flow and change from a liquid to a stable rubbery state, almost vitrified [34].

After the gel time is reached, the curing process is ready to be initiated by a catalyst in the resin system, which hardens the fiber reinforced composite. On the curing process, no external heat is used and a pressure of circa 0.015 atm (or 1500 Pa)  $\pm$  10% is applied over the night until the next day (so, for about 12 hours) and maintaining the same room temperature. Afterwards, the pressure is removed and the post curing process is ready to be performed using an industrial oven. According to the manufacturer, the post cure time should be 16 hours at 60°C [32]. After this, the cured panel is taken from the oven and its edges, which contain excess of fibers and resin due to the hand lay-up

production process (*Figure 20*), need to be trimmed. As last process, the trimmed panel is passed through a sanding machine, to give a proper surface finishing without sharper edges. At the end of these sequence of processes, the specimens are obtained (*Figure 20*) and are ready to be further tested. However, before the relevant experimental mechanical tests on the flat and curved panels are explained, one must proceed to a mechanical characterization of the panel's components, which will be further needed for simulation purposes. Thus, the experimental mechanical tests on the materials that compose the skins and the core of the sandwich composite will be addressed on section 3.2, whereas the experimental mechanical tests on the total sandwich composite will be addressed on section 3.3.



*Figure 20: Example of one curved panel specimen before trimming (panel at the front) and one curved panel final specimen after trimming and sanding (panel at the back).*

## **3.2. Mechanical tests of the components**

For effects of further simulation, one must know the properties of the materials alone, so that they can be inserted in the respective part and then further simulated. Therefore, before the relevant experiments for this thesis were performed, the properties of the skins and of the core material were determined, through the creation and further testing of several specimens. These specimens were tested in all the three relevant directions (the radial, the axial and the tangential directions), with the purpose of knowing how the material properties behave on the chosen direction. Considering the structural axes defined on *Figure 19*, the relationship between them with the material axes is the following: the tangential direction is the number 1 direction, the axial direction is the number 2 direction and the radial direction is the number 3 direction. More information regarding the INSTRON, the VIC and the correlation program used are on *Appendix A1*.

### **3.2.1. Determination of the skins properties**

The skins of the sandwich composite, since they consist of bidirectional 300 g/m<sup>2</sup> glass fibers impregnated in epoxy resin and hardener 1050/1058S, will have properties that differ along the three-orthogonal axis of symmetry. Thus, the skins material is orthotropic and elastic. So, for the obtainence of both the analytical and the experimental properties for the skins properties, the theory for an orthotropic material was reviewed from reference [35] and from pages 26-31. Therefore, for simulation purposes, the needed nine independent material coefficients for an orthotropic material

are  $E_1, E_2, E_3, G_{23}, G_{13}, G_{12}, \nu_{12}, \nu_{13}, \nu_{23}$ . For the radial direction, which corresponds to the thickness dimension, the fibers effect can be neglected, meaning that the properties can be accurately approximated as the epoxy resin and hardener 1050/1058S properties, directly provided by the manufacturer [32]. However, for the other directions, the fibers effect cannot be neglected and the previous approximation is no longer valid, which means that the properties must be determined.

### ***Specimens and set-up***

For the obtinence of the tangential and axial properties, several specimens of the skins material were produced (*Figure 21*), based on the available standards for the effect.

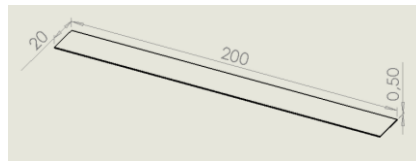


*Figure 21: Specimen's dimensions (in mm) for the obtinence of the skins properties, drawn in Solidworks®.*

For the tensile properties obtinence, the standard ASTM D3039/D3039M was used as main reference for the tensile test, to obtain the Young's Modulus and the Poisson's Coefficient of the skins material in the tangential and axial directions. For this tensile test, seven specimens were sectioned according to *Figure 21* dimensions. The dimensions of each specimen were measured using a digital paquimeter and they were also weighted using a digital scale. The obtained results, as well as the calculated density for each one of them and for both the axially and the tangentially oriented specimens, are given on *Appendix A2*.

After the preparation and identification of all the specimens, they were coloured with a white spray and then several dots were made using a black spray (*Figure 22*), as it is needed for the deformation calculation with the VIC 2D software. Further on, the specimens were placed on the INSTRON 3369 machine and, simultaneously with the VIC 2D software, the tensile test was performed at a crosshead speed of 2 mm per minute and until the material failure (*Figure 33*). More information regarding the INSTRON and the VIC is given on *Appendix A1*.



*Figure 22: Skins material specimens tangentially oriented, before (left) and after (right) the ink spraying. The same procedure was used for the axially oriented specimens.*

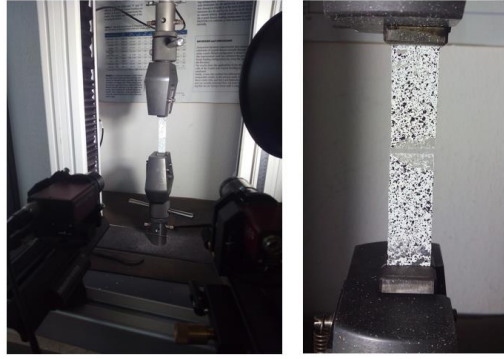


Figure 23: First specimen T1 during (left) and after (right) the tensile test.

### ***Data measurement and post-processing***

After the test of each specimen, an excel document is obtained from both the VIC and the INSTRON. From the VIC 2D, the excel document outputs the mean strains measured from the changes in the black dots from one snap to the next one and using the first snap as reference. The strains given by the VIC 2D are Lagrangian strains and, just for the first order gradients, they are calculated by:

$$\begin{cases} \varepsilon_{xx} = \frac{\partial u}{\partial x} + \frac{\left(\frac{\partial u}{\partial x}\right)^2 + \left(\frac{\partial v}{\partial x}\right)^2}{2} \\ \varepsilon_{yy} = \frac{\partial v}{\partial y} + \frac{\left(\frac{\partial u}{\partial y}\right)^2 + \left(\frac{\partial v}{\partial y}\right)^2}{2} \\ \varepsilon_{xy} = \frac{\frac{\partial u}{\partial y} + \frac{\partial v}{\partial x} + \frac{\partial^2 u}{\partial x \partial y} + \frac{\partial^2 v}{\partial x \partial y}}{2} \end{cases} \quad (\text{Equation 1})$$

, where the index  $x$  is the direction of load and the index  $y$  is the direction of contraction.

From the INSTRON machine, the excel document outputs the load being applied by the machine from one instant to the next one. Therefore, the tensile stress ( $\sigma_x$ ) is calculated from the applied load ( $F$ ) and the specimen's cross sectional area ( $A$ ) by ( $\sigma_x = \frac{F}{A}$ ) and, to synchronize the data obtained from the VIC 2D (i.e., extensions as function of a time  $t_1$ ) with the data obtained from the INSTRON machine (i.e., stresses as function of a time  $t_2$ ), a time correlation program developed in Python 3.5 was used (see *Appendix A1*). The result is an excel file with several points that define the stress-strain curves for the tested specimens. By linearizing these curves, the Young's Modulus ( $E_x$ ) can be taken from the Hooke's Law:

$$\sigma_x = E_x \varepsilon_{xx} \quad (\text{Equation 2})$$

Therefore, the Young's Modulus can be calculated from the linear regression, for each specimen and for both directions, from which the mean value is approximately 28 334 MPa for the tangential direction and 25 904 MPa for the axial direction. For more information see *Appendix A2*.

Also, the Poisson's Coefficient ( $\nu_{xy}$ ) can be calculated from the tensile test data, outputted directly from the VIC 2D and presented on the excel document, since it depends only on the ratio between the longitudinal strain ( $\varepsilon_{xx}$ ) and the transversal strain ( $\varepsilon_{yy}$ ):

$$\varepsilon_{yy} = -\nu_{xy} \varepsilon_{xx} \Leftrightarrow \nu_{xy} = -\frac{\varepsilon_{yy}}{\varepsilon_{xx}} \quad (\text{Equation 3})$$

Therefore, the Poisson's Coefficient can be calculated from the linear regression, for each specimen and for both directions, from which the mean value is approximately 0.1916 for the tangential direction and 0.1911 for the axial direction. For more information see *Appendix A2*.

For the shear properties obtainence, the *Ten-deg Off-axis Test for Shear Properties in Fiber Composites* [36] was used as main reference for the tensile test, since the Ten-deg Off-axis Test is an accurate test method for the intralaminar shear characterization of fiber composites, in order to obtain the intralaminar Shear Modulus of the skins material in the tangential and axial directions. For this tensile test, again seven specimens were sectioned according to *Figure 21* dimensions and the obtained results are given on *Appendix A*.

The same procedure and test parameters used before for the tensile test of the axially and tangentially oriented specimens, were again repeated for these specimens. However, it is important to refer that the fibers were directed about  $10^\circ$  off the load direction. Following the *Ten-deg Off-axis Test for Shear Properties in Fiber Composites* [36], for the obtainence of the Shear Modulus, the relevant properties are the intralaminar shear stress and the intralaminar shear strain along the fiber direction, which are respectively calculated from the following equations:

$$\begin{cases} \tau_{10^\circ} = \frac{1}{2} \sigma_{xx} \sin(2\theta) = 0.171 \sigma_{xx} \\ \gamma_{10^\circ} = (\varepsilon_{yy} - \varepsilon_{xx}) \sin(2\theta) + \gamma_{xy} \cos(2\theta) = 0.342(\varepsilon_{yy} - \varepsilon_{xx}) + 0.940 \gamma_{xy} \end{cases} \quad (\text{Equation 4})$$

, where  $\theta$  is the orientation angle between the applied stress (load direction) and the fiber direction (which is  $10^\circ$ ),  $\tau_{10^\circ}$  is the intralaminar shear stress and  $\gamma_{10^\circ}$  is the intralaminar shear strain.

Thus, with the applied loads outputted from the INSTRON's excel document and with the strains outputted from the VIC 2D's excel document, the intralaminar shear stresses and strains can be respectively calculated for each time value. Again, since the data obtained from the INSTRON machine and from the VIC 2D has different time intervals, the time correlation program was used to synchronize both values. Once more, a linear regression must be done on the obtained stress-strain curves, so that the slope of this curve is the Shear Modulus ( $G$ ) and the Hooke's Law is again valid:

$$\tau_{10^\circ} = G_{xy} \gamma_{10^\circ} \Leftrightarrow G_{xy} = \frac{\tau_{10^\circ}}{\gamma_{10^\circ}} \quad (\text{Equation 5})$$

Therefore, the Shear Modulus can be calculated from the linear regression, for each specimen and for both directions, from which the mean value is approximately 1 603 MPa for the tangential direction and 3 024 MPa for the axial direction. For more information see *Appendix A2*.

## ***Results and discussion***

The final analytical and experimental properties to be inserted on the numerical model are compared on *Table 3*. Since on the radial direction the effect of resin will overcome the practically irrelevant effect of the fibers, the experimental values for  $E_3$ ,  $\nu_{13}$ ,  $\nu_{23}$ ,  $G_{13}$  and  $G_{23}$  were not determined and the resin properties were directly inserted, as it was referred before.

Table 3: Analytical and experimental skins properties obtained for the numerical model.

	$E_1$ [MPa]	$E_2$ [MPa]	$E_3$ [MPa]	$\nu_{12}$ [ ]	$\nu_{13}$ [ ]	$\nu_{23}$ [ ]	$G_{12}$ [MPa]	$G_{13}$ [MPa]	$G_{23}$ [MPa]
Analytical	16 533	16 533	3 460	0.284	0.3	0.3	1 582	1 331	1 331
Experimental	9 852	9 042	3 460	0.192	0.3	0.3	1 878	1 331	1 331
Deviation [%]	40.41	45.30	-	32.39	-	-	18.71	-	-

From *Table 3* it is possible to conclude that the deviation of the obtained properties is as high as circa 45% for the  $E_2$  value. The relatively high deviation's values, which arise when the experimental properties are compared with the analytical and using the last ones as reference, are essentially due to the analytical assumption that the adhesion between the fibers and the matrix is perfect. However, between the microscopic particles that compose the fibers, the space is not completely and 100% filled with the matrix content. The impregnation of the resin amongst the fibers is far from being perfect and, experimentally, there are several empty spaces which were not filled with resin. Thus, although the percentage of voids was accounted during the calculation of the volume fraction of fibers, its real extend is not completely predicted by the analytical solution.

Another relevant effect is due to the way in which the VIC 2D calculates the mean strains. The strain values on both the direction of loading and on the transverse direction might be somewhat noisy, and this will have a major effect on the values of the properties. These discrepancies might be due to three relevant factors. The first factor might be the images being too bright, which makes most of the image overdriven and very little detail in the speckles. The ideal image should have a background with a nice range of grey. The second factor might be the variation of the pattern, in which some speckles might be very big and the other ones very small. The big speckles are okay, but the small ones (from one to two pixels) might cause aliasing effects. Although the Low Pass Filter option was enabled, this might also have had some influence on the final mean strains values. Finally, the third factor might be due to the waviness of the strains plot. This is normally caused by the existence of refractive heat waves during the test, which might have been caused by the light used. This light, when it is hot, causes index of refraction changes in the air in the optical path, which might also lead to uncertainties on the final obtained result. Even though these factors were minimized to achieve an incrementally better and clean result, their effect was present during the tests. Therefore, the fairly small strains measured were probably blurred by the three referred factors, which led to the differences between the experimental and the analytical values. Although the deviation is relatively high, both the analytically and the experimentally determined properties for the skins were introduced on the numerical model. The results that will be presented further on the FEA will consider always the experimental skins properties. However, whenever a final comparison is made, the results obtained with the analytical properties will also be introduced.

### 3.2.2. Determination of the core properties

The core of the sandwich composite consists only of a NL20® cork agglomerate with 5 mm thickness. According to the production of agglomerated cork described at *Chapter 2*, the cork planks are laid aleatory, then compacted and impregnated with the resin. So, the properties of agglomerated

cork depend on the type of adhesive used, the granules and the technology of production and, since the granules on the cork agglomerate are oriented towards aleatory and different directions, the core will have properties that are similar along the three-orthogonal axis of symmetry. Thus, the core material is isotropic and hyperelastic, due to the cellular nature of the cork material itself. However, this hyperelasticity is just evident under compression, because under tension its behavior is mainly elastic, as it can be seen on *Figure 6* and *Figure 7*. These two figures, where the stress-strain curves obtained for boiled cork are given, are the only analytical results that are available. Therefore, since the complete NL20® cork agglomerate stress-strain curve is not available on the manufacture sheets, no relevant comparison with the analytical results would be made on this section.

Recalling once again *Figure 19* and bearing in mind that the purpose of the core's properties determination is only for simulation purposes, when simulating the non-linear behavior of a hyperelastic material, the only thing that needs be inserted is the complete stress-strain curve of the material. Therefore, compression and tensile tests must be performed. For the verification and validation of the isotropy of the core, the specimens were tested along the three-orthogonal axis of symmetry referred. So, for the obtainence of the experimental curve for the core properties, the theory for an hyperelastic material was reviewed from reference [35] and from pages 22-24.

### ***Specimens and set-up***

For the compression stress-strain curve obtainence, the standard ASTM C365-03 was used as main reference. For this compression test, again seven specimens were sectioned for each direction. The dimensions were based on the standard definitions and chosen for the particles to be of a representative size (*Figure 24* and *Figure 25*). Afterwards, the dimensions of each specimen were measured using a digital paquimeter and they were also weighted using a digital scale. The obtained results, as well as the calculated density for each one of them, are given on *Appendix A3*.

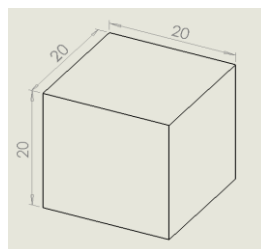


*Figure 24: Specimen's dimensions (in mm) for the core compression properties, drawn in Solidworks®.*



*Figure 25: Core material specimens sectioned for the compression test in all directions.*

Still for the compression test, it was performed using an INSTRON 5566 machine at a crosshead speed of 5 mm per minute (*Figure 26*). It is important to refer that no initial pre-load was

introduced on the specimen, because the agglomerated cork conditioning conditions are unknown. More information regarding the INSTRON and the VIC is given on *Appendix A1*.

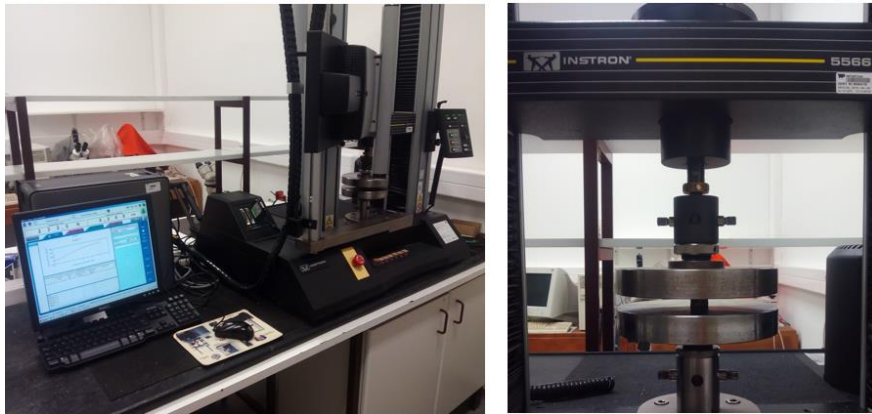


Figure 26: First specimen R1 during the compression test.

On the other hand, for the tensile stress-strain curve obtainence, the standard ASTM C297 and *TUB-Shower* [37] were used as main references for the radial direction, whereas the standard ASTM D638 and *Introduction to Tensile Testing* were used as main references for the tangential and axial directions. The specimens on the radial direction had to be perpendicularly tested, since the available agglomerated cork sheets only had maximum thicknesses of 20 mm, meaning that it was impossible to make specimens with circa 200 mm for tensile testing based on the ASTM D638 standard. Therefore, seven specimens were sectioned for the radial direction and five were sectioned for the tangential and axial directions. The dimensions were based on the standard definitions for each direction (*Figure 27* and *Figure 28*). Afterwards, the dimensions of each specimen were measured using a digital paquimeter and they were weighted using a digital scale. The obtained results, as well as the calculated density for each one of them, are given on *Appendix A3*.

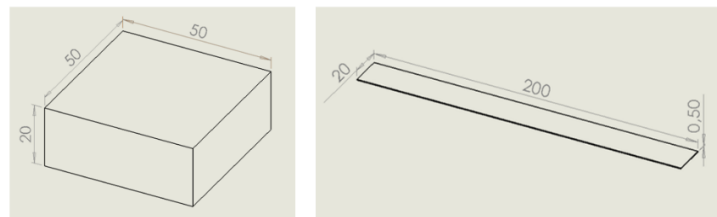
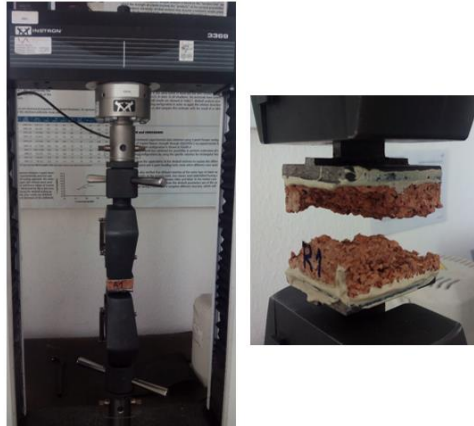


Figure 27: Specimen's dimensions (in mm) for the core tensile properties and for the radial direction (left) and for the tangential and axial directions (right), drawn in Solidworks®.



Figure 28: Core material specimens sectioned for the tensile test in the radial direction (left) and in the tangential and axial directions (right).

Still for the tensile test, and starting with the radial direction, iron pieces were glued to the specimens with an epoxy paste, before the test could even start. This procedure was performed in roughly 15 minutes and, after the specimens were glued to the iron pieces, they were left for rest during 24 hours, for the resin to cure. Afterwards, the specimens were placed on the INSTRON 3369 machine and the perpendicular tensile test was performed at a crosshead speed of 2 mm per minute (*Figure 29*). More information regarding the INSTRON and the VIC is given on *Appendix A1*.



*Figure 29: First specimen R1 during (left) and after (right) the tensile test.*



*Figure 30: First specimen T1 during (left) and after (right) the tensile test.*

Still for the tensile test, and moving to the tangential and axial directions, the specimens were sprayed with the pattern of black dots over a white background, as it was performed for the specimens of the skins material and as it was previously referred. Then, the specimens were placed on the INSTRON 3369 machine and the tensile test was performed at a crosshead speed of 2 mm per minute, where simultaneously photos of the specimen were taken using the VIC 2D snap software at a speed of one photo per second. It is important to refer that (as it was used for the skins tensile tests) 50 mm of the total length of the specimen were introduced on each one of the tabs, meaning that roughly 100 mm were being left for the calibration using VIC 2D (*Figure 30*).

### ***Data measurement and post-processing***

For the compression test and after the test of each specimen, an excel document is obtained from INSTRON, where the compressive load being applied by the machine and the displacement of the tabs from one instant to the next one are outputted. On this particular case, the displacement suffered by the tested specimens can be accurately approximated by the displacement of the

machine. This arises from the fact that a compression test is being performed and that known methods to measure the displacement are inappropriate, methods such as an extensometer (since its usage on materials such as cork would create a rigid zone, which would induce error on the final obtained result) or VIC 2D (since the camera wouldn't be able to capture a clear image of the vertical face of the specimen). As referred before, the compressive stress for each point ( $\sigma_x$ ) can be calculated from ( $\sigma_x = \frac{F}{A}$ ). The compressive extension for each point ( $\varepsilon_{xx}$ ) is calculated from the machine longitudinal displacement ( $d$ ) and the specimen's longitudinal initial length ( $l_0 \approx 20$  mm):

$$\varepsilon_{xx} = \frac{(l_0+d)-l_0}{l_0} = \frac{d}{l_0} \quad (\text{Equation 6})$$

The result of this process for each specimen is an excel file with several points that define the stress-strain curve of the tested specimens. Since in the beginning of each one of the tests, the tabs and the specimen are fitting each other (for the cork to stabilize and for the specimen to present parallelism on its compressed faces), a linear approximation must be performed for the first values. This procedure was performed for all the tested specimens. The obtained stress-strain curves for agglomerated cork in all directions and under compression are given on *Appendix A3*. Through the analysis of the stress-strain curves, as well as the absence of any type of visible fracture in the specimens and the observed almost instantaneous elastic recovery, the already referred hyperelastic behavior of the core material can now be confirmed. The average stress-strain curve for each direction is obtained through the mean of the stress-strain curve for each one of the seven specimens.

For the tensile test and for the radial direction, an excel document is again obtained from the INSTRON, where the load being applied by the machine and the displacement of the tabs from one instant to the next one are outputted. The VIC 2D software was not used for these specimens, because its implementation was hard due to the small vertical length that was going to be needed for the analysis. So, the displacement obtained directly from the machine was used. As referred before, the compressive stress for each point ( $\sigma_x$ ) can be calculated from ( $\sigma_x = \frac{F}{A}$ ) and the compressive extension for each point ( $\varepsilon_{xx}$ ) can be calculated from (*Equation 6*). On the other hand, for the tangential and axial directions, an excel document is obtained from both the VIC and the INSTRON. From the VIC the extension is directly withdrawn and from the INSTRON the tensile stress ( $\sigma_x$ ) is calculated from ( $\sigma_x = \frac{F}{A}$ ). To synchronize the data obtained from the VIC with the data obtained from the INSTRON, the already referred time correlation program developed in Python 3.5 was used.

The obtained stress-strain curves for agglomerated cork in all directions and under tension are given on *Appendix A3*. Through the analysis of the stress-strain curves, as well as the brittle fracture visible in the specimens, one might conclude that the material experiences elastic behavior under tension, as stated before. The average stress-strain curve for each direction is again simply obtained through the mean of the stress-strain curve obtained for each one of the tested specimens.

## ***Results and discussion***

From the determination of the core properties, the final analytical and experimental stress-strain curves to be inserted on the numerical model are compared on *Figure 31*.

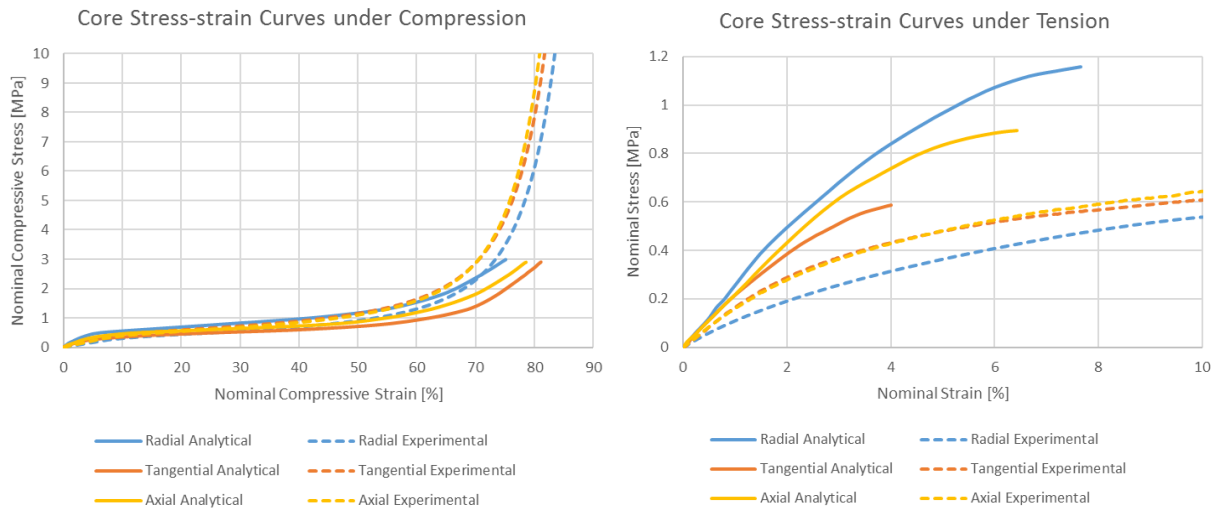


Figure 31: Comparison between the stress-strain curves obtained for the boiled cork (analytical curves) and for the cork agglomerate (experimental curves) under compression (left) and under tension (right).

Comparing both the analytical curves for boiled cork with the experimental curves obtained, one can easily observe that the mechanical behavior of agglomerated cork is considerably different than the one of cork. The hyperelastic behavior under compression persists and it is intensified, since the material can withstand higher compressive loads for the same compressive strain. Although this behavior can be verified almost throughout the entire curve and for all directions, it is more visible for higher strains. Under tension, even though the addition of resin occurred for the production of agglomerated cork and it would have been expected that its behavior was stiffer and more rigid than the one given for the boiled cork, it can be seen that the slope of the experimental curves are lower, when compared with the analytical curves. Thus, agglomerated cork can reach higher tensile strain values, when compared to the boiled cork planks, meaning that its behavior is more flexible. The final analytical and experimental stress-strain curves were based on the mean of the obtained results for each direction and will be the ones to be introduced on the numerical model (Figure 32). Since the experimental curves are the ones in which the agglomerated cork is considered, instead of the boiled cork considered analytically, the experimental curve will be the one considered for the FEA.

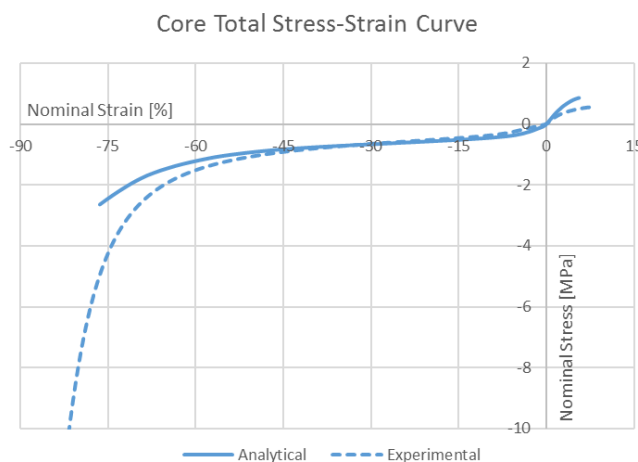


Figure 32: Comparison between the final stress-strain curves obtained for the boiled cork (analytical curve) and for the cork agglomerate (experimental curve), considering the compression and the tensile behavior.

### 3.3. Mechanical tests of the panels

Following the experimental procedure described on section 3.1., several specimens of both the flat and the curved panels were produced for the experimental tests. After their production, the dimensions of each specimen were measured using a digital paquimeter (and a ruler, when a digital paquimeter could not be used) and they were also weighted using a digital scale. The obtained results, as well as the calculated global composite's density for each one of them, are given in *Appendix A4*. Using the three referred panels of each type, two experiments were conducted for this thesis, compression and vibration tests, which will be widely discussed on this section. Since both tests had the same type of specimens and since their characteristics were widely discussed on section 3.1., where the materials and the production method were addressed, there is no need to give on the next sections any additional information regarding this topic.

#### 3.3.1. Compression test

The main objective of the experimental compression test is the obtainence of the experimental load-displacement curve. Thus, for the compressive vertical load obtainence the INSTRON 3369/5566 machines were used (according to its availability) and for the compressive vertical displacement obtainence the VIC Snap/-3D software were used. More information regarding the INSTRON and the VIC is given on *Appendix A1*.

##### *Set-up, data measurement and post-processing*

Before the compression test could start, several aspects were taken into consideration for the set-up. One of the first main difficulties regarding this test was related with the fact that the panel needed to be simply supported on the tab and not grabbed by it, for the test to be performed without introducing any extra states of tension, nor to crush the panel on the tab's influence area. Thus, and largely due to the considerable length of the panel, a steel bar with the same length of the panel was produced, one for the upper tab and other for the lower tab (*Figure 33* and *Figure 34*). This steel bar, when placed on the tab, allow for the test to be performed with the panel simply supported on the beam and maintaining the same border condition throughout the entire length of the panel.

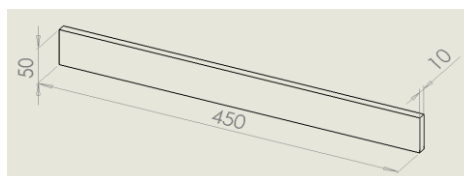


*Figure 33: Dimensions (in mm) of the steel bar produced for the compression test. Created with Solidworks®.*



*Figure 34: Steel bars produced for the compression test, where the tab grabbing area is highlighted.*

After the production of the steel bars, they were placed on the INSTRON machine tabs. To guarantee their horizontal placement as much as possible, a level was used and the correct positioning achieved (*Figure 35*). Due to the panel's considerable dimensions, both the upper and the lower tab had to be rotated 45° counter clockwise, for the panel to fit the INSTRON machine dimensions and to not be in contact with it during the whole duration of the assay. This rotation made the implementation of the VIC-3D harder, but far from being impossible.



*Figure 35: Level placed on the top of the upper tab for its horizontal levelling.*

Preliminary curved panels were produced to test if either it was better to place the black and white dots pattern on its concave or on its convex side, for the analysis using the VIC. After both tests were performed, it was possible to conclude that the best way is to test the panel with the pattern on the convex side, since the obtained result's projection errors were lower when compared to the panel with the pattern on the concave side. This result comes to confirm an already expected behavior, since the compression of the panel forces its curvature to get bigger. This means that, if the pattern is on the concave side, this side would get farther from the VIC-3D set of cameras, whereas it gets nearer if the panel is tested with the pattern on its convex side. With the pattern on the convex side, then the set of cameras will capture progressively more focused sets of dots, instead of progressively more defocused and distant dots. Thus, having the set-up for the compression test (*Figure 36*) and following once again the procedure already described, each one of the panels can be tested.

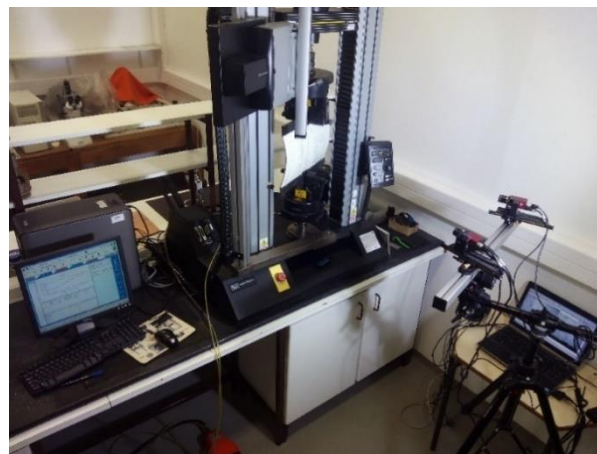


*Figure 36: Compression test set-up performed for the curved panel.*

After the test is performed for each one of the panels, the results from the INSTRON machine and the VIC system are synchronized by the time correlation program and the final set of points that define the compressive test of each panel are obtained. Due to the initial fitting of the tabs with the specimen, a linear approximation must be done. For all the linear regressions made, it is possible to

conclude that they fit almost perfectly the obtained data, since the coefficient of determination ( $R^2$ ) is approximately 0.99 for all of them. After this procedure was performed for all the specimens and for both the flat and the curved panels, the experimental curves could be obtained.

## Results and discussion

From the determination of the experimental curves for the compressive vertical load (RF2) as a function of the compressive vertical displacement (U2), the final results are given on *Figure 37*.

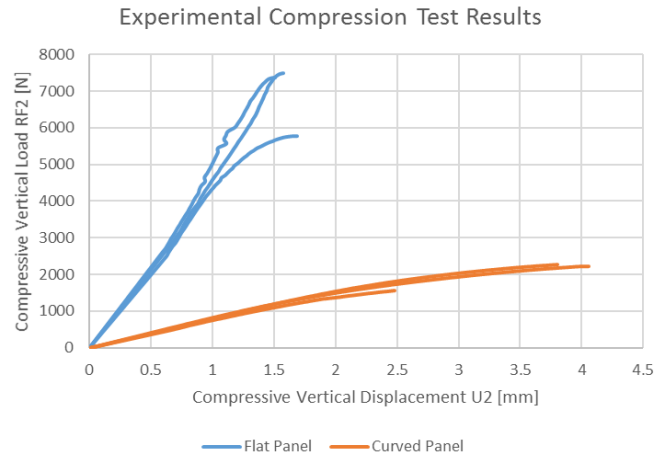


*Figure 37: Experimental curves for the compressive vertical load as a function of the compressive vertical displacement (RF2-U2 curves), obtained for the flat and the curved panels under a compression test.*

From the experimental curves of *Figure 37*, the first observed characteristic is that the three tested flat panels have an identical behavior between them, with no relevant discrepancies, fact that also occurs for the three tested curved panels. For all the panels that were tested, due to the skin's fiber and resin characteristics, which strengthen and confer rigidity to the final composite, a purely elastic behavior can be observed. Performing a linear regression on each one of the experimental curves of *Figure 37*, it is possible to obtain their expected behavior. As it was said before, the coefficient of determination ( $R^2$ ) value was also checked and it was found that the correlations can be approximated accurately as linear, due to the fact that  $R^2$  is always higher than 0.90 (except for one of the curved panels with a lower value). The slope  $m$  of these linear curves defined by  $y = mx$  can also be a measurement of stiffness, even though it does not give directly the Young's Modulus (*Table 4*). Considering the results of *Table 4* and the experimental curves of *Figure 37*, several sets of data points can be taken and analysed. Thus, *Table 5* presents the compressive vertical displacement (U2) value, for increments of 500 N on the compressive vertical load (RF2).

*Table 4: Slope ( $m$ ) and coefficient of correlation ( $R^2$ ) of the linear regression curves defined for each panel under a compression test.*

	Flat Panels			Mean	Curved Panels			Mean
	1	2	3		1	2	3	
$m$	4 682.09	4 981.92	3 933.42	4 532.48	685.15	681.37	643.49	670.01
$R^2$	0.988	0.984	0.911	-	0.960	0.918	0.874	-

*Table 5: Experimental compressive vertical displacement ( $U_2$ ) values for increments of 500 N on the compressive vertical load (RF2), for the flat and the curved panels under a compression test.*

RF2 [N]	U2 [mm]					
	Flat Panels			Curved Panels		
	1	2	3	1	2	3
500	0.117	0.114	0.125	0.681	0.636	0.606
1000	0.235	0.228	0.251	1.356	1.251	1.230
1500	0.352	0.341	0.376	2.326	1.947	2.012
2000	0.469	0.455	0.502	-	2.929	3.199
2500	0.587	0.569	0.627	-	-	-
3000	0.702	0.668	0.725	-	-	-
3500	0.794	0.760	0.820	-	-	-
4000	0.894	0.846	0.922	-	-	-
4500	0.986	0.932	1.047	-	-	-
5000	1.088	0.997	1.194	-	-	-
5500	1.191	1.076	1.401	-	-	-
6000	1.289	1.178	-	-	-	-
6500	1.373	1.275	-	-	-	-
7000	1.442	1.367	-	-	-	-

Due to the slope  $m$  of the linear regression curves, the flat panels are considerably stiffer than the curved panels. This behavior was predictable but it can now be quantified, since the mean value for  $m$  is circa 6.75 times higher for the flat panels, a very high value considering the reduced thickness of the final composite. With the introduction of curvature on the panel, its stiffness is progressively reduced, but this might outcome some advantages. These advantages are related with the displacement versus force relationship. Stiffer panels (such as the flat panels) withstand forces more than 6.75 times higher than less stiffer panels (such as the curved panels). However, stiffer panels withstand approximately 15% of the total displacement withstood by the tested curved panels. Therefore, as future development on this topic, an optimization study could be performed to achieve the best configuration for the needed application, through a compromise between both variables. Also from *Table 5* one might easily observe that the third flat panel and the first curved panel have experienced catastrophic failure earlier than the other panels of the same type. On both cases this was mainly due to the production method. For the third flat panel tested, the panel had a bit more warp than the other two, which might have lead to the small discrepancies witnessed. On the other hand, for the curved panel, the first one had considerably more bubbles and warp. Besides that, during the cure on the oven, there was even a superficial local that suffered stronger heat effects, when compared to the rest of the panel, which might have reduced the panel's stiffness.

### ***Failure mechanisms***

In addition to the experimental compression test, since this test was performed until the panel's catastrophic failure, an analysis on the failure mechanisms should also be carried out. For

both the flat and the curved panels, the failure mechanisms and its chronological sequence are somewhat identical, even though they can be more easily visualized on the curved panel. During the compression test, a sequence of failure mechanisms takes place until the final failure. Thus, when the compressive loads start to be applied, the panel's skins start to slowly wrinkle, phenomena that is more visible on the most fragile skin of the sandwich. Wrinkles on the skins tend to get bigger as the applied compressive loads increases until a point in which the panel's core is crushed by the most fragile skin and local indentation occurs. At this phase, the face in which the most fragile skin crushed the core suffers face failure, in which the direction is approximately parallel to the length of the panel and located approximately in the middle of the panel's width (*Figure 38*). This means that both the composite and the skins thicknesses, as well as the skins strength, were insufficient to withstand the applied compressive load, which led to the panel's face failure. On both panels, this face failure occurred always on the face that was under compression, by detriment of the one that was under tension. However, the panel's production method might again be the justification, in which a skin tends to always get thicker than the other one. This occurs during both the flat and the curved panel's production and is due to the pressure application phase. When pressure is applied, by the action of the vertical gravity forces and particularly due to the resin impregnation on the agglomerated cork core (see section 3.4), resin tends to infiltrate from the upper skin (where pressure is directly applied) down to the core and eventually reaching the lower skin. This means that the resin content introduced on the upper skin will be reduced, that the agglomerated cork core will be aleatorily impregnated with resin and that the lower skin will have more resin content than the upper skin. Thus, the lower skin will tend to get thicker, but also more fragile than the upper skin, which means that the panel will fracture first on the so called lower skin (*Figure 38*).

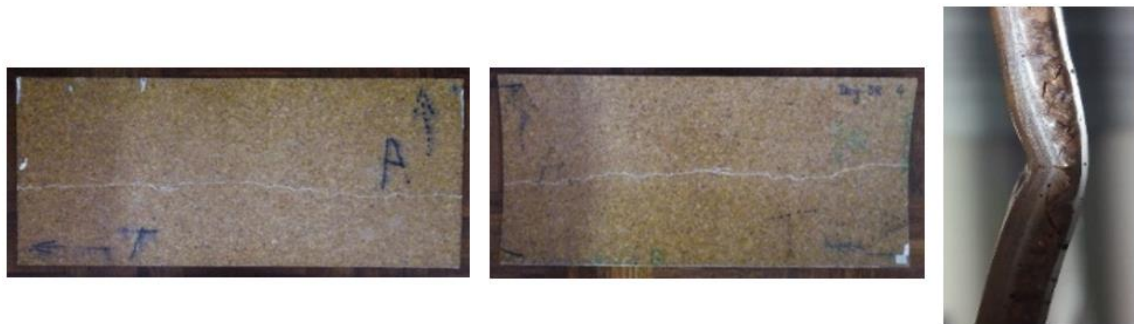


*Figure 38: Face failure visible on both the flat (left) and the curved (middle) panels. Also, a section view on a flat panel is given (right), in which the face failure can be seen on the most fragile skin.*

### 3.3.2. Vibration test

#### ***Set-up, data measurement and post-processing***

For the vibration test to be performed, some specifications and requirements must be met. First, to eliminate most of the external factors as possible, the test was performed on the university's vibration test laboratory, which is located underground, whereas the air-conditioning was shutdown and all the elevators and doors were closed, for the air to be as still as possible to not interfere with

the test. A truss structure of metal beams with a set of pulleys was used to support the panels during the test, panels that must be supported, for the test to be equivalent to the free in-space vibration test (*Figure 39*). This is made to avoid the constraints influence during the test. Therefore, two Nylon wires were placed at the two-top vertex of the panel, both with the same chosen length. This placement was made with cyanoacrylate glue, to create a rigid connection and to not add any type of extra weight to the panel. Magnets or other types of setup could have been used but, since their disadvantages outcome their advantages, for this thesis purpose glue is the best option.



*Figure 39: Vibration test laboratory and respective set-up.*

For this test, there were two available options to excite the panel and two available options to measure the displacement experienced by the panel. To excite the panel, a hammer or a shaker could have been used and they are usually connected to a force transducer (force). When compared, the hammer is less repeatability, since it is based on knocking the panel on the same spot and for several times. Therefore, it is very hard for a person to do this with the same force and always on the same spot, which leads to imprecisions in the result, so this method will not be used. If a machine was used instead of a person, this method might be better. Thus, for this experimental test a shaker was used, since it is the best available method to excite the panel. On the other hand, to measure the panel displacement, could have been used a LASER (velocity) or an accelerometer (acceleration). When an accelerometer is used, an extra weight is also introduced on the panel, which will increase its frequencies to higher values. This leads to different values of frequencies and it is not desirable, so this method will not be used. Therefore, the LASER beam is the most accurate way to measure the panel's displacement, since it does not add any extra mass as the accelerometer does and since it allows for more precision, because its focus does not change during the time where the experiment takes place. Thus, for this experimental test a LASER was used, since it is the best available method to measure the panel's displacement.

To analyse all the available vibration modes of the panel (i.e., both the even and the odd mode shapes), both the shaker and the LASER must be placed on opposite corners of the panel (*Figure 40*). If both were placed on the centre of the panel, then only the even mode shapes could be identified. The choice of these corners is not random, but the differences between changing the opposite corners in which these two components are placed are so small, that this choice is basically irrelevant. On the corner where the LASER is pointing at, a reflector surface was added to the panel, for the LASER beam

to be completely reflected back to the LASER beam source and accurately measured. On the other hand, on the corner where the shaker is placed, a thin metal disk is glued to the panel, whose purpose is to connect the force transducer with the panel. The force transducer is then connected to the shaker. Some time and effort must be spent on placing correctly the panel (to leave it as much horizontal as possible), the shaker (to leave the force transducer as much perpendicular to the panel as possible) and the LASER (to point the LASER towards the reflector surface).



Figure 40: Vibration test set-up and performed for the curved panel, where the LASER and shaker are visible.

After the stated requirements are met, the test is then ready to be started, if all the machines are connected by coaxial cables and turned on, according to the schematics of Figure 41. When the test starts, the computer outputs a random voltage signal, which is then amplified and transmitted to the panel by the shaker. Then, this signal is converted into displacements, measured by the LASER. The signal measured by the LASER is transmitted to the fiber interferometer, then to the velocity decoder and then amplified by the amplifier, before it is transmitted to the spectral analyser. On the other hand, the force signal measured by the force transducer is transmitted directly to the spectral analyser. The spectral analyser gives then the input signal for the computer. With this provided data from the random voltage signal firstly outputted, the computer program creates a phase and an amplitude diagrams. It is also important to refer that the program calculates the frequencies using Fourier transform. Saving the data from the outputted graphs, the user obtains a text document with a set of several points with a real and an imaginary value for each frequency value, which relates to the amplitude-phase diagram. The amount of frequency values to be measured is introduced in the program, whereas the range from point to point is always the same.

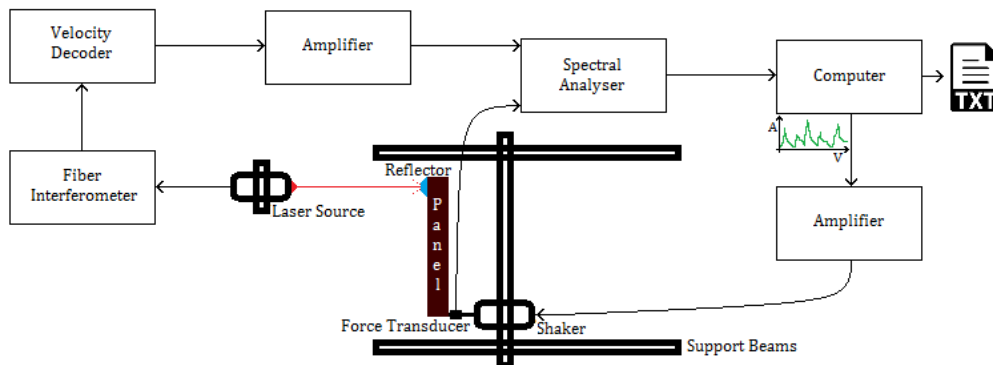


Figure 41: Schematics of the vibration test (considering a top view).

## Results and discussion

To analyse the text document outputted after each test, then a routine on Matlab was created. This routine reads all the points present on the text document and identifies the peaks on the obtained amplitude-frequency diagram, since each one of these peaks means that there is a frequency of vibration there. To confirm these values, also the amplitude-phase diagram is given by the same Matlab routine and for both the flat and the curved panels (see *Appendix A5*). The results obtained for the first frequencies of vibration for the flat panels and for the curved panels tested are presented on *Table 6*. It is important to refer that only frequencies until 400 Hz were simulated and that frequency values around 50 Hz might be inaccurate due to the interference with the network frequency, which is around that value.

*Table 6: First frequencies of vibration (in Hz or cycles per time) obtained for the flat and curved panels tested, where 3 specimens were tested for each type of panel.*

		Flat Panel				Curved Panel			
		1	2	3	Mean	1	2	3	Mean
Frequency [cycles/time or Hz]	1	9.3	6.8	6.3	7.4	11.8	11.3	11.0	11.4
	2	13.3	11.3	10.0	11.5	23.5	20.5	20.5	21.5
	3	78.3	72.8	72.3	74.5	80.0	77.8	75.8	77.9
	4	94.3	92.5	90.3	92.4	174.0	172.0	167.0	171.0
	5	180.0	173.0	174.0	175.7	198.0	198.0	195.0	197.0
	6	250.0	239.0	255.0	248.0	216.0	216.0	208.0	213.3
	7	261.0	260.0	267.0	262.7	229.0	221.0	214.0	221.3
	8	287.0	301.0	304.0	297.3	250.0	256.0	247.0	251.0
	9	341.0	341.0	343.0	341.7	257.0	261.0	256.0	258.0
	10	377.0	378.0	374.0	376.3	289.0	296.0	299.0	294.7

After knowing the values for the vibration frequencies (*Table 6*), the panel was excited with these frequency values and the modes of vibration could be identified experimentally using a diapason and checking whereas the panel vibrated or stood still. This procedure is very useful, since it allows for a better understanding and identification of the further vibration modes given by the simulation results. However, it is important to notice that usually the finite elements programs are more rigid than the reality, therefore the numerical frequencies should be less than the experimental ones. Furthermore, from the experimental results alone, one has no clue over the existence or the absence of rigid body vibration modes, where the vibration frequencies usually have a value of approximately zero. Typically, a body without any applied border conditions and that is free in space should present six rigid body vibration modes, both translation and rotation vibration modes around each one of the three orthogonal axes. Therefore, both panels should have six rigid body modes before the first frequency mode of vibration.

### 3.4. SEM Analysis

In addition to the experimental tests and to the numerical analysis carried out, a look upon the microstructure of the sandwich composite should be performed. The need and will for this observation aroused on early stages of this dissertation and it is because cork is a cellular material, whose singular behavior strongly depends on its microscopic structure. This cellular behavior is easily observed microscopically and is widely available on several references of *Chapter 6*, since agglomerated cork's microstructure is composed of several granules of cork cells, which differ in size, orientation and number of cells. This aleatory behavior turns cork agglomerate into an isotropic material, as it was experimentally verified. Besides this randomness verified on the granules, also the cork cells differ one from another, where some cells are corrugated, others are stretched and it is even possible to observe collapsed cells. Effects like these are not considered by the typically used finite elements software, but play an important role during the experimental compression and vibration tests performed on the previous sections. However, the importance to visualize the sandwich composite microstructure is specially to understand how does the interaction between the skins and the core works. Therefore, the final composite configuration was analysed on a scanning electron microscope (SEM). A deeper analysis on the SEM conclusions is referred at *Appendix A6*, as well as relevant images obtained from the SEM.

Besides some expected behaviors observed on the agglomerated cork's microstructure, a rather unusual effect can be seen, which has a major influence on the core's properties. This effect is the resin impregnation on the core of the sandwich composite (*Figure 42*). Therefore, for further simulation effects, this means that the core has parts where the resin impregnation is almost perfect and one can consider the material as agglomerated cork plus the impregnated resin, but there are also parts where the impregnated resin presence is almost null, which means that the material can be only considered as agglomerated cork. Thus, the interaction between the parts on the numerical model is impossible to be accurately simulated using the available software's functions, on a typically used finite elements software.

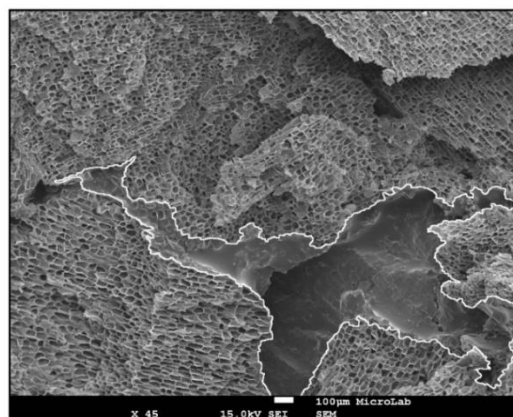


*Figure 42: Detailed view along the composite's thickness and under an amplification of  $\times 45$ , where the cork cells impregnated with resin can be seen (inside of the white border), as well as the cork cells (outside of the white border). Impregnated resin can be identified on other cells on this image, even though on a smaller scale.*

## 4. Numerical Simulation

The main objective of this thesis is the mechanical behavior characterization of a cork core sandwich curved panel. Thus, both a curved and a flat panel were analysed, for a comparison to be performed, and considering the 1:3 scale model of the chosen panels referred on *Figure 16*. For an accurate numerical model, all the needed inputs must be determined in a proper way. Therefore, the materials used on the layers, the interaction between them, the boundary conditions, the loads and the specific requisites of each test have to be carefully studied.

For the numerical analysis of both the flat and the curved panels and for both the compression and the vibration tests, many different FEA software might have been chosen. Most companies use Abaqus, Ansys, Nastran or LS Dyna for FEA. The two last ones are mainly used for dynamic analysis and the two first ones are mainly used for contact analysis. Thus, since contact analysis will be needed and since Abaqus is a more robust software in terms of performance and was highly recommended, Abaqus 6.13<sup>®</sup> software was chosen for the creation of the numerical model.

### 4.1. Compression tests

#### 4.1.1. FE mesh, support and loading conditions

When one opens the software for the first time, eleven Modules with a set of options inside appear chronologically.

The first module is the **Part**, where the several parts that build up the final test are created. The 3D deformable modelling space was chosen for each part, with an extrusion solid or shell base feature, depending on which part was being created. The approximate size dimensions were introduced in millimetres, meaning that all further simulation units have to be introduced according to that. Every time a new part is created, the module **Sketch** is opened and, when the part is finished, the software brings the user back to the Part's module, right after the solid is extruded. Parts were made for the skins and the core and, particularly for the compression test, also a part had to be made for the steel bars that balanced the composite within the machine dimensions.

The next module is the **Property**, where the several needed materials are created. For this thesis, three materials were defined. For the composite's core, the density was introduced directly from the manufacturer tables [29] and was 200 kg/m<sup>3</sup>. However, for the behavior, since it is hyperelastic, Abaqus asks for the set of points that define the behavior curve and no manufacturer data is available. Thus, experimental tests were carried out on section 3.2.2, to obtain the uniaxial test data to be inserted as the input source. Then, the material was defined as isotropic, as it was verified by the experimental tests. Also, the data to define the volumetric response as to be inserted and, due to the lack of available volumetric test data, a Poisson's ratio has to be given. A Poisson's

ratio of 0.5 is exhibited by perfectly incompressible materials under elastic deformation at small strains (such as rubber) and a Poisson's ratio of 0 is exhibited when the lateral displacement under compression is approximately zero (such as pure cork). However, cork agglomerates exhibit a value which is not 0 nor 0.5, but it is in-between both. Although it is known that the Poisson's ratio varies with the level of deformation imposed in cork agglomerates [38], a proper value has to be inserted. "At the beginning of compression, it is approximately 0.15 for all agglomerates and, as deformation takes place, cell walls start to collapse and buckle and the value drops to very low values (circa 0.05). As densification starts to take place, the coefficient value rises again." (adapted from [38]). Therefore, a Poisson's ratio of 0.15 was introduced.

Finally, the strain energy potential must be given and properly justified. There are several particular forms of the strain energy potential available in Abaqus, from the models for incompressible or almost incompressible materials (such as cork agglomerates are), to the hyperelastic model for highly compressible and elastic materials (such as elastomers are). Thus, Abaqus let the user choose from different hyperelastic material models: polynomial and its particular cases (reduced polynomial, neo-Hooke, Mooney-Rivlin and Yeoh), Ogden, Arruda-Boyce and Van der Waals. Each one of these models was widely studied for this dissertation. However, only a brief explanation adapted from Abaqus 6.13® Analysis User's Guide [39] will be given.

First, the polynomial model for the strain energy potential in Abaqus is obtained after a Taylor series expansion is performed and it is given by:

$$U = \sum_{i+j=1}^N C_{ij}(\bar{I}_1 - 3)^i(\bar{I}_2 - 3)^j + \sum_{i=1}^N \frac{1}{D_i}(J - 1)^{2i} \quad (\text{Equation 7})$$

, where the parameter  $N$  goes until six (even though  $N > 2$  is rarely used),  $\bar{I}_1$  and  $\bar{I}_2$  are respectively the first and the second invariants of the Cauchy-Green deformation tensor,  $C_{ij}$  and  $D_i$  are material parameters and  $J$  is the elastic volume strain.

When  $N = 1$ , so that only the linear terms are considered, the Mooney-Rivlin model is obtained:

$$U = C_{10}(\bar{I}_1 - 3) + C_{01}(\bar{I}_2 - 3) + \frac{1}{D_1}(J - 1)^2 \quad (\text{Equation 8})$$

The Mooney-Rivlin model can be seen as an extension of the Neo-Hooke model, where the term that depends on the second invariant  $\bar{I}_2$  is not considered:

$$U = C_{10}(\bar{I}_1 - 3) + \frac{1}{D_1}(J - 1)^2 \quad (\text{Equation 9})$$

The Neo-Hooke model is the simplest hyperelastic model. Thus, the Mooney-Rivlin model will in most cases give a more accurate fit to the experimental data than the Neo-Hooke model. However, both models give similar accuracy, since they use only linear functions of the invariants, which means that they do not allow for the correct representation of for example the hyperelastic upturn when cork is compressed at high strains. Particular forms of the polynomial model are also obtained, whenever specific coefficients are annulated. If all  $C_{ij}$  with  $j \neq 0$  are set to zero, the reduced polynomial model is obtained and, if  $N = 3$ , a special case of the reduced polynomial is obtained, the Yeoh model:

$$U = \sum_{i=1}^3 C_{i0} (\bar{I}_1 - 3)^i + \sum_{i=1}^3 \frac{1}{D_i} (J - 1)^{2i} \quad (\text{Equation 10})$$

Usually, the magnitudes of the  $C_{i0}$  coefficients will create the typical S-shape of the stress-strain behavior of cork agglomerates, meaning that the Yeoh model often provides an accurate fit over a large strain range.

The Ogden model is given by:

$$U = \sum_{i=1}^N \frac{\mu_i}{\alpha_i^2} (\bar{\lambda}_1^{\alpha_i} + \bar{\lambda}_2^{\alpha_i} + \bar{\lambda}_3^{\alpha_i} - 3) + \sum_{i=1}^N \frac{1}{D_i} (J - 1)^{2i} \quad (\text{Equation 11})$$

, where  $\mu_i \alpha_i > 0$ ,  $\forall i = 1, \dots, N$  (no sum over  $i$ ),  $\sum_{i=1}^N \mu_i \alpha_i = 2G$ ,  $\forall G > 0$ ,  $G$  is the Shear Modulus,  $\mu_i$  and  $\alpha_i$  are material parameters determined experimentally or numerically and  $\bar{\lambda}_i$  are the principal stretches of the Cauchy-Green deformation tensor.

Even though the first part of Ogden's strain energy function depends only on the first and second invariants, it cannot be written explicitly in their terms. The value of  $N$  is specified by the user and the values for  $\mu_i$  and  $\alpha_i$  are computed by Abaqus. The Mooney-Rivlin model is obtained when  $N = 2$ ,  $\alpha_1 = 2$  and  $\alpha_2 = -2$  and the Neo-Hooke model is obtained when  $N = 1$  and  $\alpha_1 = 2$ . Therefore, the Ogden model can be seen as a generalization of the two previously referred models.

The Arruda-Boyce model is given by:

$$U = G \sum_{i=1}^5 \frac{C_i}{\lambda_m^{2i-2}} (\bar{I}_1^i - 3^i) + \frac{1}{D} \left( \frac{J^2 - 1}{2} - \ln J \right) \quad (\text{Equation 12})$$

, where  $\lambda_m$  is the coefficient of locking stretch and  $C_i$  are coefficients whose value arises from a series expansion of the inverse Langevin function, which is truncated after the fifth term and which arises in the statistical analysis of non-Gaussian chains.

The Arruda-Boyce potential depends on the first invariant and it can be seen as a fifth-order reduced polynomial, where the five  $C_{10}$  to  $C_{50}$  coefficients are implicit non-linear functions.

Finally, the Van der Waals model is given by:

$$U = G \left\{ -(\lambda_m^2 - 3)[\ln(1 - \eta) + \eta] - \frac{2}{3} a \left( \frac{\bar{I} - 3}{2} \right)^{\frac{3}{2}} \right\} + \frac{1}{D} \left( \frac{J^2 - 1}{2} - \ln J \right) \quad (\text{Equation 13})$$

, where  $\bar{I} = (1 - \beta)\bar{I}_1 + \beta\bar{I}_2$ ,  $\beta$  is the parameter that represents a linear mixture combining both invariants into  $\bar{I}$ ,  $\eta = \sqrt{\frac{\bar{I} - 3}{\lambda_m^2 - 3}}$  and  $a = \frac{2C_{01}}{3G} + \frac{\lambda_m^2}{\lambda_m^3 - 1}$  (Kilian et al., 1986) is the parameter of global interaction between the chains, which is difficult to estimate. Realistic values of  $a$  will contribute to the characteristic S-shape of tensile stress-strain curves in the middle strain range and before the final upturn.

After all the previously referred strain energy potentials available in Abaqus were deeply studied, the test data has to be inserted on Abaqus and, from the nine different hyperelastic material models that were possible to be used, each one of them was inserted and analysed. Through the Evaluate key, it is possible to see that the curve that best fits the experimental curve is the one using the fifth order Ogden's strain energy potential, Ogden N5 (*Figure 43*). It is important to refer that convergence was not achieved for all the available models. The models in which divergence occurred do not appear on *Figure 43* and are the Marlow and the Ogden N2, N3, N4 and N6 models.

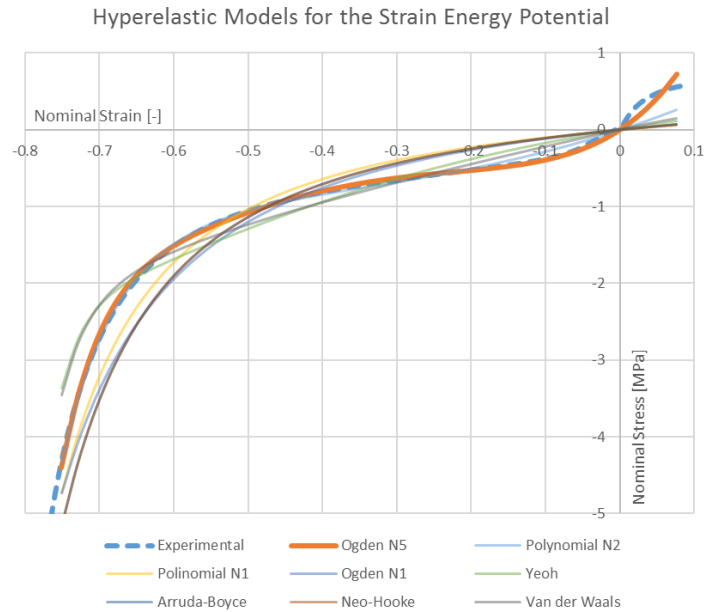


Figure 43: Fitting of all the available hyperelastic models in comparison with the experimental test data curve. It is possible to see that the Ogden N5 curve is the one that best fits the Experimental curve.

For the composite's skins, the density had to be analytically calculated and is  $1\,169\text{ kg/m}^3$ . For the skins, the behavior introduced was elastic but, when choosing its type, eight options are possible in Abaqus: isotropic, engineering constants, lamina, orthotropic, anisotropic, traction, coupled traction and shear. The skins are orthotropic if one consider all directions, but transversally isotropic, as seen in 3.2.1. However, due to the coefficients asked for Abaqus when the orthotropic type is enabled, the chosen type was through the engineering constants. Therefore, the nine independent material coefficients for an orthotropic material ( $E_1, E_2, E_3, G_{23}, G_{13}, G_{12}, \nu_{12}, \nu_{13}, \nu_{23}$ ) were introduced. After this, the material orientation has to be defined for an accurate simulation. The option that was chosen for the orientation definition was the discrete, in which the normal axis was identified as the 3<sup>rd</sup> direction and the primary axis as the 1<sup>st</sup>. The stacking direction was identified as the 3<sup>rd</sup> and, at the end of this process, the correct material axes could be obtained (Figure 44).

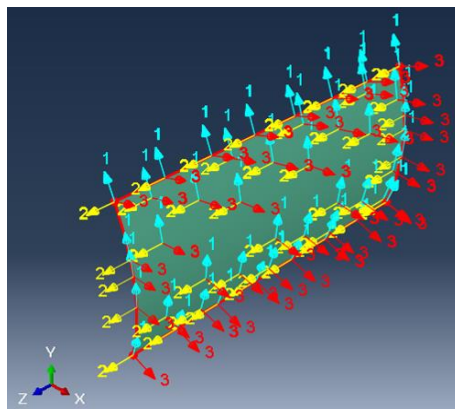


Figure 44: Material orientation axes, as seen in Abaqus 6.13<sup>®</sup> software and for the curved panel.

For the tabs, the material is steel, whose properties were taken directly from the steel manufacturer tables, page 16 [40]. Thus, the density introduced was  $7\,850\text{ kg/m}^3$  and the behavior

introduced was elastic and isotropic, with a Young's modulus of 200 GPa and a Poisson's ratio of 0.3. The Poisson's ratio value inputted was 0.3, due to the fact that most steels and rigid polymers exhibit values of about 0.3 before yield, values that increase periodically after yield and up to 0.5 [40].

After the properties for all materials were introduced, the materials must be assigned to sections and the respective parts. Therefore, for the tabs and flat panels a homogeneous solid was created and for the curved panels a homogeneous shell and, after that, the respective material and its theoretical thickness value were introduced. To finish this part, the thickness integration rule that was chosen was the Gauss rule with 5 integration points.

The next module is the **Assembly**, where all the parts are uploaded independently as instances and then, through mechanisms of translation and rotation, placed on the right position. All the needed reference points were also introduced and the needed partitions were made.

The next module is the **Step**. Here, after the initial step that exists by default, a new step for the wanted analysis was created. For the compression test, knowing that the objective of this simulation is to perform a static analysis, the struggle now is to choose between the General or the Riks analysis. When only material instability exists, the General static analysis is enough. However, when geometric instability also exists, Riks static analysis is best suited due to its arc-length method. On this method, both force and displacement are unknown and the user must define the total arc length (default is 1), the initial arc length increment (default is 1) and the maximum arc length increment (default is  $1 \times 10^{36}$ ). The values were all set on default, due to the coherency verified on the status file's Load Proportionality Factor (LPF). To summarize, Riks static analysis was chosen since it can process the decreasing part of the load-deformation curve (i.e., for zero and negative stiffness), while the General static analysis will diverge in this case.

The next module is the **Interaction**. Here, the interaction between the skins and the core of the composite must be defined, as well as the interaction between the steel bars and the total panel.

The first two constraints define each one of the steel bars as rigid bodies. For this purpose, the top steel bar and the bottom steel bar regions were selected and associated with a reference point, inserted on the interface between each bar and the composite panel. This means that, after the analysis is performed, the user is now able to select the respective reference point and obtain the desired numerical properties. The other two constraints define the interaction between each one of the skins and the core of the composite were tied. On a tie type constraint, first the master surface and then the slave surface were defined, considering always the master surface as the stiffer material surface (i.e., the material with the higher Young's modulus, which is the skin's material). After this, the discretization method and all the other parameters were set on default and also no initial surface was adjusted nor rotational Degrees of Freedom (DOFs) were tied. With the constraints defined, a new interaction was created for each one of the steel bars and the panel. The chosen type was surface-to-surface contact (standard) interactions and, again, the master and the slave surface were defined, knowing that now the steel bars have the highest Young's modulus. All options were set on default, except for the surface smoothing, where the option to automatically smooth 3D surfaces when

applicable was enabled. To finish each interaction, the only thing that is now left is to create an interaction property, which will be the same for both interactions. The type of interaction property chosen was a contact property, whose normal and tangential behavior were the options chosen.

For the normal behavior, the pressure-overclosure was set as hard contact and the constraint enforcement method on default. No separation after contact was allowed. For the tangential behavior, first one might have considered the interface as frictionless, but actually no perfectly frictionless surface exists. When two surfaces are in contact, tangential or friction forces will be created when there is movement. Friction can be divided into fluid friction (which involves the flow of fluids or rigid bodies immersed in fluids or in contact with them) and dry or Coulomb friction (which involves rigid bodies in contact along non-lubricated interfaces) [41]. Since rigid bodies are in contact without any lubricant, only dry friction is present in here. Therefore, for the dry friction to be considered during the analysis, friction formulation was set as penalty. Inside the shear stress and the elastic slip separators, all parameters were set on default but, on the friction separator, the friction coefficient must be given.

There is a difference between static and kinetic friction coefficients, which is easily explained by the example of a block at rest on a horizontal plane and pushed by a force  $F$  (Figure 45). If  $F$  is small, the block will not move because there is the action of a friction force, opposite to  $F$  and which balances it. This is the static friction force ( $F_s = \mu_s N$ ), whose behavior is not exactly known, but it is assumed that it is due to superficial irregularities and to molecular attraction [41]. If  $F$  is increased,  $F_s$  also increases until its magnitude reaches a certain maximum value  $F_m$ . If  $F$  is further increased the block starts to slide. As soon as the block has been set into motion, magnitude drops from  $F_m$  to  $F_k$ , due to the lower verified interpenetration between the superficial irregularities [41]. From this point on, the kinetic friction force ( $F_k = \mu_k N$ ) remains approximately constant, even though the block keeps sliding with increasing velocity [41]. The friction coefficients  $\mu_s$  and  $\mu_k$  do not depend upon the contact surface's dimensions, but depend on several other factors, such as the contact pressure, the velocity of contact and the harder surface roughness. So, since the data may vary significantly, the values used as reference are given in Table 7, from which a value of 0.5 was chosen.

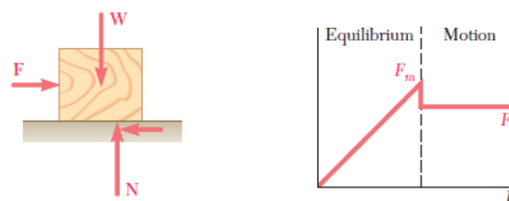


Figure 45: Diagram of forced acting on the block (left) and of the friction force as a function of  $F$  (right) [41].

Table 7: Range of values for the coefficient of static and dynamic friction for dry and lubricated interfaces.

Highlighted are the values used as base for the considered interface (adapted from [41]).

Interface	Dry Friction		Lubricated Friction	
	Static	Dynamic	Static	Dynamic
Steel – Steel	0.5-0.6	0.4-0.6	0.15	0.15
Steel – Wood	0.5-0.6	0.2-0.5	0.1	0.05
Wood – Wood	0.4-0.6	0.2-0.4	0.15	0.15

The next module is the **Load**, where the boundary conditions need to be defined. The first boundary condition was defined for the reference point of the top steel bar and consists on all the six degrees of freedom fixed, with an exception for the vertical axis, where the displacement value needed was introduced. Because it is a compression test, the value introduced was -200, considering the default global axis. The second and last boundary condition was defined for the reference point of the bottom steel bar and consists on all the six degrees of freedom fixed.

Moving on to the **Mesh** module, first the element type was selected for both the total panel parts and the steel bars. For the first, a continuum shell element was considered (since the panel considered was curved), whereas for the second, a 3D stress element was considered (since the steel bars are planar and rigid bodies). The element library chosen was the standard and the geometric order was linear, being all the other parameters for the element type set on default. After the element type is attributed to each one of the assembly parts, then the seed part instance command was used, to assign global seeds to all the parts. On the sizing controls, the approximate global seed size was chosen and this value was changed, to verify the convergence of the FEA. Curvature control was enabled with a maximum deviation factor of 0.1 (it varies from 0 to 1) and the minimum size control was defined by a 0.1 fraction of the global size (it varies from 0 to 1 also). After performing this for all the parts, the assembly is seeded, which means that the mesh parts command can be used to mesh the entire assembly with the chosen finite element type and size (*Figure 46*).

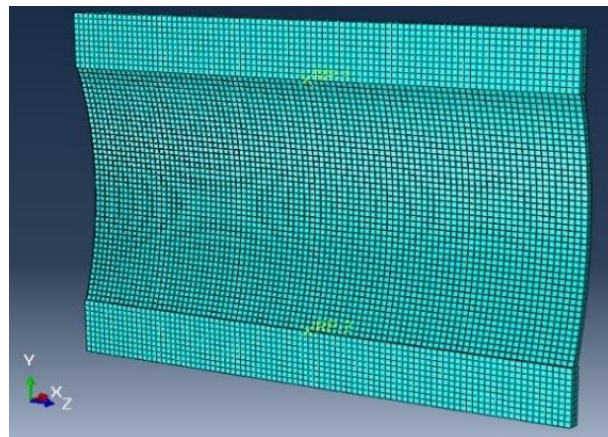


*Figure 46: Mesh with finite elements of 5 mm size, as seen in Abaqus 6.13<sup>®</sup> software and for the curved panel under a compression test.*

The next module is the **Optimization**. However, since it was not used, nothing will be described and one can move to the **Job** module, where a Job was created for the full analysis to be performed. All parameters were left on default and, after the analysis is completed, the software brings us to the last module, where the results are shown.

On the last module, which is called **Visualization**, the output database (ODB) file is generated and read. For the compression test, the data from the visualized 3D graphs must be extracted for both the vertical displacement U2 and the vertical reaction force RF2. Thus, one must select the create XY data button and then the ODB field output option. Here, the variables U2 and RF2 were chosen and the nodal element (from which these variables are extracted) was defined at the elements/nodes set

by one of the reference points created previously. Both reference points will output the same data. Saving the changes and selecting the XY data manager option, the chosen variables for the current session appear with the respective values for each increment, values those that consist in a set of XY points, where X is the time increment value and Y is the chosen variable (so, U2 or RF2 on this case). Taken both Y values and placing them into an excel document, then the numerical displacement-force curve can be seen and further compared with the experimental one.

#### 4.1.2. Results and discussion

Considering the procedure widely described for the creation of the numerical model to properly simulate the compression test, a finite elements analysis was performed. Therefore, the accuracy of the FEA must be verified and, regarding the numerical model, this verification is done through a convergence study. To verify the convergence of the numerical model, the mesh size was changed, by performing a change on the finite elements size that compose the mesh itself. The size of the elements started with elements as big as 100 mm under to elements as small as 5 mm. For both panels, since the behavior of the RF2-U2 curve converges to a specific curve when the mesh size is increasingly more refined, then convergence is verified (*Figure 47*). The final mesh is composed by finite elements of 5 mm size and the results for the vertical displacement (U2) and the vertical load (RF2) are shown on *Figure 48* for the flat panel and on *Figure 49* for the curved panel.

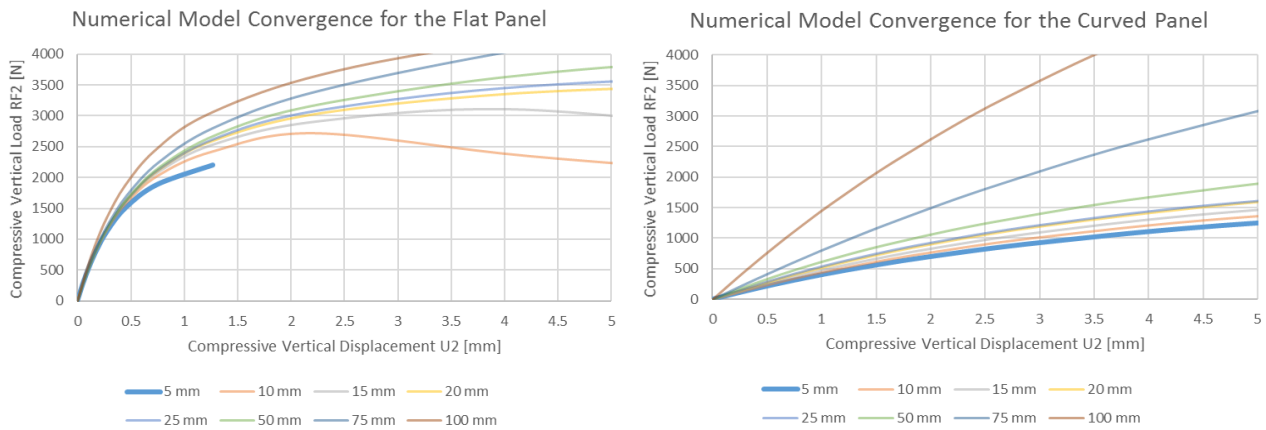


*Figure 47: Numerical model convergence verification for the flat (left) and for the curved (right) panels, where the finite elements size was reduced from 100 mm to 5 mm for both.*

From the convergence curves of *Figure 47* for the numerical model, by choosing the most refined mesh curve (i.e., the one obtained for finite elements with 5 mm size) and performing a linear regression on it, it is again possible to obtain the expected behavior. To raise the correlation accuracy, both linear regressions were performed considering only the first 0.3 mm of the compressive vertical displacement (U2). Thus, it was found that the coefficient of determination ( $R^2$ ) value is 0.981 for the flat panel and 0.999 for the curved panel, from which one can conclude that the linear approximation is valid. On *Table 8* is the value of the slope  $m$  and of the coefficient of correlation  $R^2$ , considering the linear curves defined by  $y = mx$ . For comparison purposes, the same procedure that was described until here and where the experimental properties for the skins were considered, was performed using their analytical properties, whose results are given on *Table 8*.

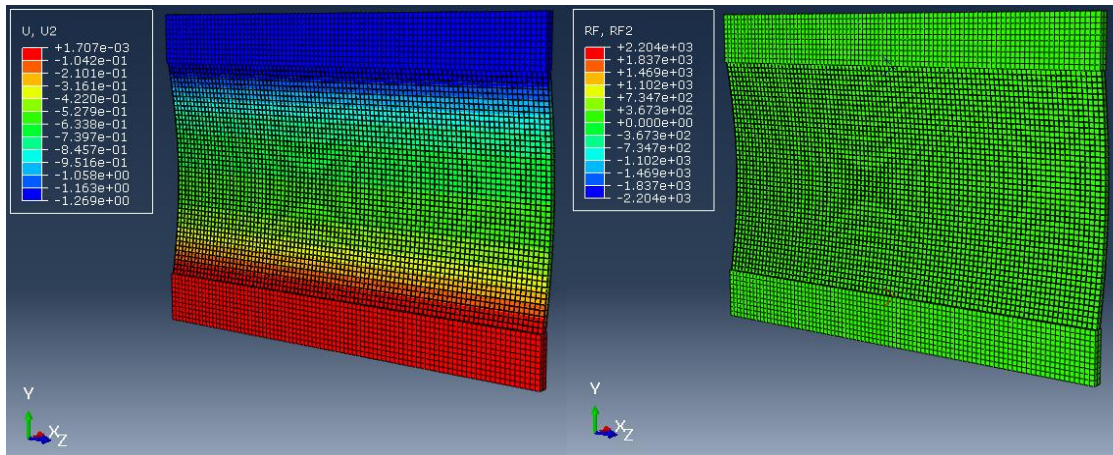


Figure 48: Vertical displacement  $U_2$  (left) and vertical load  $RF_2$  (right) for the flat panel and considering the last increment of the analysis. The size of the finite elements that compose the mesh is 5 mm.

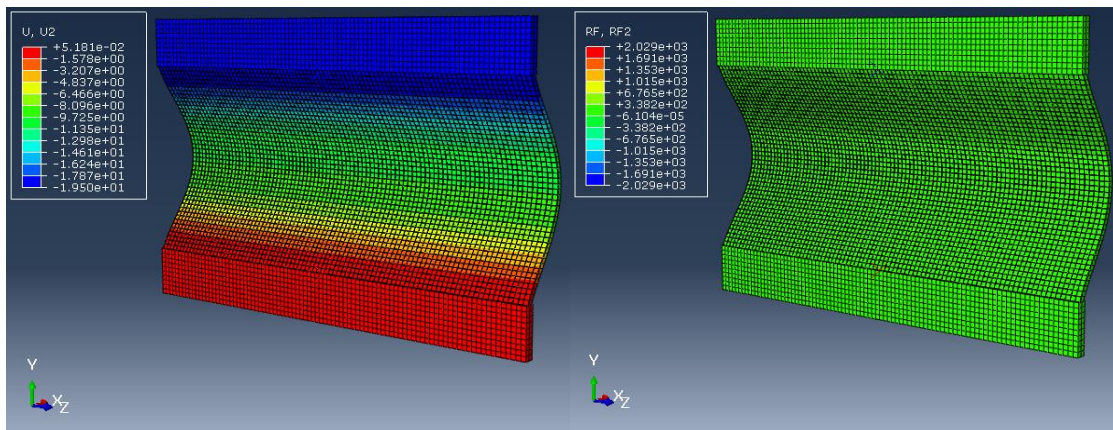


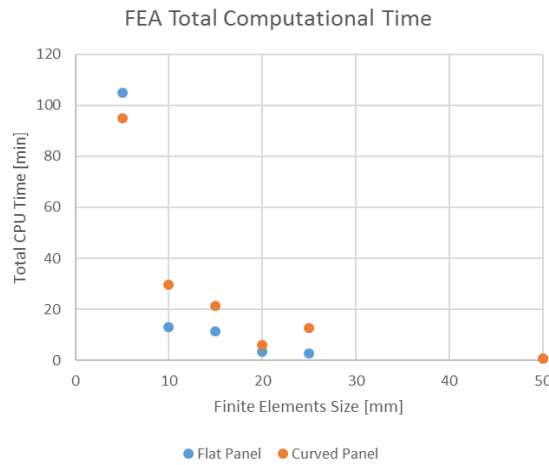
Figure 49: Vertical displacement  $U_2$  (left) and vertical load  $RF_2$  (right) for the curved panel and considering the last increment of the analysis. The size of the finite elements that compose the mesh is 5 mm.

Table 8: Slope ( $m$ ) and coefficient of correlation ( $R^2$ ) of the linear regression curves defined for each panel under a compression test and for a mesh of finite elements with 5 mm size. Results are shown considering the experimental (column A) and the analytical (column B) properties for the skins.

	Flat Panels		Curved Panels	
	A	B	A	B
$m$	4 181.23	4 660.98	440.43	478.04
$R^2$	0.981	0.973	0.999	0.999

Whenever a convergence study is performed on a numerical analysis, also a computational time analysis might be carried out. As it is expected, more refined meshes (i.e., meshes with smaller elements) allocate a bigger amount of computer memory for the analysis when compared to less refined meshes, which was verified, since the computational time increases potentially with the increase of the number of finite elements (Figure 50). However, this behavior means that meshes with finite elements of 1 mm size or lower, due to the high allocation of memory that they request from the CPU, could not be simulated with the means available for this thesis. However, results achieved with finite elements of 5 mm size will be very close to the ones achieved with more refined meshes. It is also relevant to refer that the computational time requested for the curved panel's FEA

is more than the one requested for the flat panel's FEA, which can be seen by the slope of the potency curve of *Figure 50*. This fact is particularly due to the curved panel's geometry that will increase the non-linear effects, which will then involve more processor memory for a proper simulation.



*Figure 50: Total CPU time for the numerical finite elements analysis of both the flat and the curved panels, where the potency tendency curve can be seen for each one of both cases.*

In addition, also a failure mechanisms analysis might be performed in here, by comparison with the experimental results. Comparing both the numerical results of *Figure 48* for the flat panel and of *Figure 49* for the curved panel with the experimental results of *Figure 38*, one might observe that for both panels the behavior is somewhat similar. However, and particularly for the flat panel, the experimental failure mechanism tends to occur in one specific line located in the middle of the panel (which is not perfectly straight), whereas the numerical failure mechanism tends to occur in two parallel lines, located at the same distance from the middle of the panel. This difference is justified particularly because the experimental system is far from being perfect, which means that the experimental failure occurs due to microfractures on the panel's skins which tend to propagate and ultimately lead to the face failure along one roughly straight line. On the other hand, on the numerical FEA, the numerical failure occurs on the specific spots in which the maximum moments are generated, which correspond to the two referred lines, which justifies the visible difference between both cases, specially for the flat panel's numerical model.

### 4.1.3. Comparison between the experimental and the numerical results

Having the FEA results from the numerical model, one is now able to compare the numerical results with the experimental. The behavior of the RF2-U2 curves can be approximated by a linear regression for both panels. Thus, the  $y = mx$  curve was plotted for the experimental behavior (where the value used for  $m$  is the one on the mean columns of *Table 4*) and for the numerical behavior (where the value used for  $m$  is the one on *Table 8*), from which the resultant RF2-U2 curves can be easily compared (*Figure 51*). The numerical results using the properties for the skins determined experimentally are given by the index 'A' and the ones determined analytically by the index 'B'.

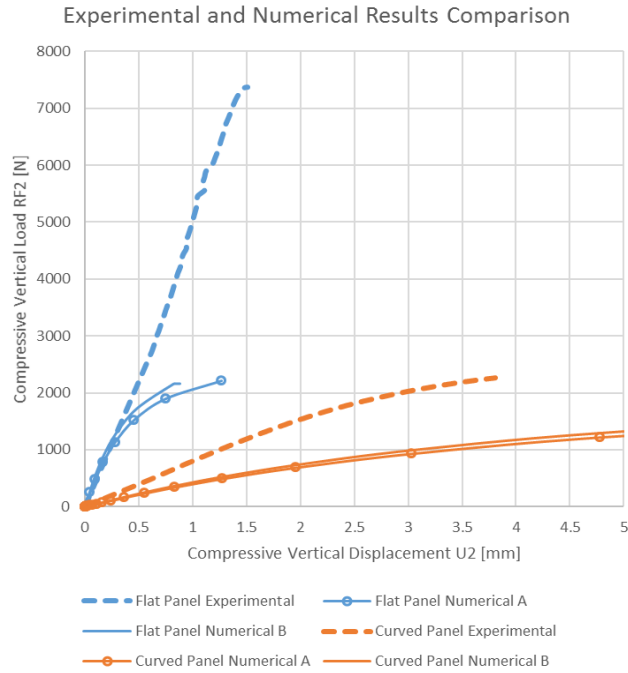


Figure 51: Comparison between the experimental and the numerical curves for the compressive vertical load as a function of the compressive vertical displacement (RF2-U2 curves), obtained for the flat and the curved panels under a compression test.

By performing a linear regression on the curves of *Figure 51*, the deviation of the results can be analysed and further justified. Considering the experimental results as the reference for the deviation, with the  $m$  values of the *A* columns of *Table 8*, the deviation is 7.75% for the flat panel and 34.27% for the curved panel and, with the  $m$  values of the *B* columns of *Table 8*, the deviation is 2.83% for the flat panel and 28.65% for the curved panel. The conclusion that can be almost immediately taken is that the results obtained using the analytical properties for the skins (index 'B') are always more accurate than the ones obtained with their experimental properties (index 'A'). This is inherent to the experimental tests conducted to obtain the experimental properties for the skins.

However, another factor occurs, which explains the differences between the results obtained for each type of panels. The panels simulated numerically with the analytical properties for the skins correspond to the purely analytical result and, since the FE program usually is more rigid than the reality, when the experimental properties for the skins are introduced, the slope of the linear curve is lower (as expected), which means that the panel is less rigid. Following this way of thinking, it would be expected that the linear regression of the experimentally tested panels would have a slope lower than the two numerical results. However, this is not what happens. The slope of the linear regression for the results of the flat panels experimentally tested, has a value in the middle of both numerical results but, for the curved panels, this value is higher than both numerical results. Two major reasons influence this behavior, which only occur experimentally and cannot be properly simulated: the resin impregnation on the cork core and the warp of the panels. During the production method and the cure process, the resin that was laid on the skins flows from them to the cork core, which then tends to get stronger and make the total sandwich composite to be better held together. Thus, the rigidity of the panel increases, as well as the slope of the linear regression, being this a

characteristic experienced by both the flat and the curved panels. Considering now the warp of the panels, if one used advanced techniques to produce sandwich panels, the warp effect would be widely reduced. However, this effect always occurs experimentally, when a structure of this type is produced. Due to the geometry of the flat and the curved panels, warp will decrease their rigidity.

Therefore, the numerical models reproduce the experimental results in terms of initial linear elastic stiffness and initial non-linear behavior. However, when the non-linear behavior is simulated for larger displacements, the numerical model loses accuracy and its validity might be questioned. From the previously obtained results and conclusions, considering that for engineering purposes a deviation of 5 up to 10% can be normally accepted as accurate, one might conclude that the numerical model is valid for the flat panel and only for this one. However, the author of this dissertation states that the numerical model is also valid for the curved panel. The problem lies within the software capabilities to accurately simulate the non-linear and hyperelastic behavior of the agglomerated cork core. For this matter, a stochastic model for the resin impregnation amongst the cork agglomerates of the core should be developed in Fortran and further inserted on the numerical model. Thus, the numerical results would come nearer to the ones obtained experimentally. The curved panel would present more discrepancies due to its geometry (i.e., its curvature), which increases the non-linear effects earlier than they occur for the flat panel.

## 4.2. Vibration

### 4.2.1. FE mesh, support and loading conditions

For the proper simulation of the experimental test, besides the procedure widely described on section 4.1.1. for the creation of the numerical model for the compression test, other aspects must be added to it. Thus, a punctual mass and soft springs must be added to the numerical model to simulate, respectively, the mass that is added to the panel when the force transducer is placed on its surface and the two Nylon ropes that sustain the panel. Both these features are on the special toolbar of the **Interaction** module.

For the punctual mass creation, first a reference point was added to the surface of the panel, located where the force transducer is placed. Then, selecting the inertia special feature and the point mass/inertia type, the value that had to be introduced for the isotropic mass was 0.027 kg divided by two (since the force transducer's active mass is circa half of the accelerometer's mass). So, the value for the punctual mass that was introduced on the reference point RP-1 was 0.135 N (*Figure 52*).

For the soft springs creation, the same procedure was performed for all the four edges, where the springs were connecting the panel to the support beams on the experimental test. Therefore, the spring/dashpots special feature was selected and the connect points to the ground (standard) type was chosen, whereas just the spring direction and spring constant must be defined. For the direction vector of the soft springs, a new datum CSYS referential needs to be created, where the first direction (denoted by  $x$ ) was used for it. This direction is selected by enabling the first degree of freedom and the resultant all the four distinct CSYS referential are shown in yellow on *Figure 52*.

Then, one has to give a spring constant value on the property separator, which can be deduced from the spring equation (Equation 10.14 of [41]), based on the Hooke's Law ( $\sigma = E\varepsilon$ ):

$$K = \frac{F}{L} \quad (\text{Equation 14})$$

Now, one can obtain the value for the constant  $K$  considering that Nylon fishing lines were used to support the panel. Using the experimental results obtained by Shimadzu [42] for several specimens of the same Nylon fishing line, the load-displacement curve can be obtained (Figure 53). As it was performed previously on other sections of this dissertation, by performing a linear regression on the experimental curves, it is possible to obtain the values for the wanted slope  $K$  and to conclude that the linear regression fits properly the obtained experimental results, due to the value of  $R^2$  (Table 9). Through the mean of the obtained slopes for the experimental curves, the obtained value for  $K$  is 0.132 N/mm, which was the value introduced on Abaqus for the spring stiffness.

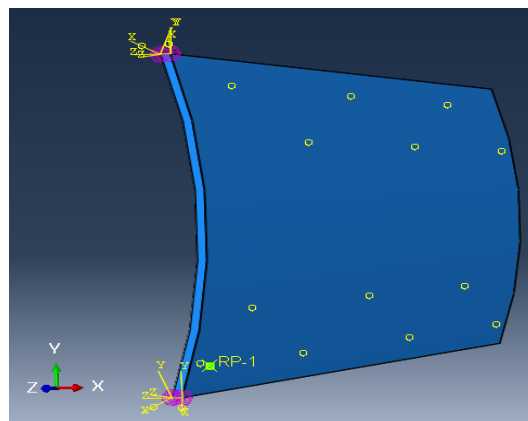


Figure 52: Special features used for the vibration test numerical model, as seen in Abaqus 6.13® software and for the curved panel. The punctual mass is placed on the reference point RP-1 and the soft springs are placed on the four edges with the four distinct CSYS referential.

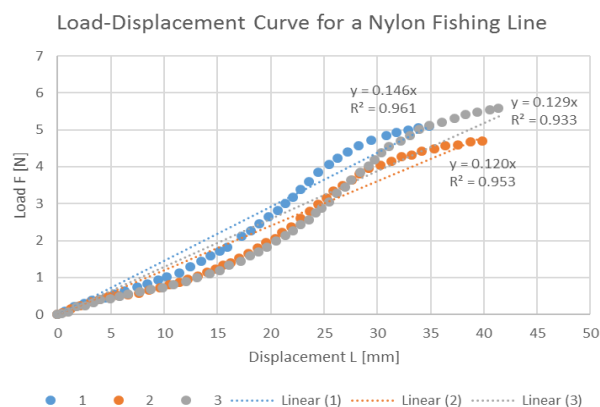


Figure 53: Load-displacement curves obtained for three specimens of a Nylon fishing line and respective linear regressions (adapted from [42]).

Table 9: Slope ( $K$ ) and coefficient of correlation ( $R^2$ ) of the linear regression curves defined for each specimen.

	Nylon Fishing Lines			Mean
	1	2	3	
$K$	0.146	0.120	0.129	0.132
$R^2$	0.961	0.953	0.933	-

Therefore, the value of 0.135 N for the punctual mass and the value of 0.132 N/mm for the soft springs stiffness coefficient were both added to the numerical model.

On the **Step** module, instead of the Riks static analysis chosen for the previous tests, for the vibration test a Frequency analysis must be chosen, with the respective Lanczos eigensolver. The requested number of eigenvalues is introduced, considering that the first 6 frequencies are the rigid body modes and they should have a frequency value of zero, which means an infinite period. This is because the panel does not have any boundary condition, so it can translate or rotate about the three axes, which means that it has 3 rigid body translations and 3 rigid body rotations.

Finally, on the Visualization module, for this vibration test purpose and contrarily to the compression test, the frequency values and the modes of vibration of both panels can be instantly visualized after the ODB file is generated.

#### 4.2.2. Results and discussion

Considering these additions, as well as the procedure to properly simulate the vibration test, a finite elements analysis was performed. Again, the accuracy of the FEA must be verified through a convergence study. To verify the convergence of the numerical model, the mesh size was changed from elements with 100 mm size until elements with 5 mm. Even though divergence phenomena occur for almost all frequencies, the frequencies tend to converge to a specific value when the mesh size is increasingly refined, which verifies the convergence as it was verified for the compression test's numerical model. The results for the first ten frequencies of vibration are shown on *Table 10* for the flat panel and on *Table 11* for the curved panel.

*Table 10: Numerical convergence verification for the first frequencies of vibration (in Hz or cycles per time) obtained for the flat panel, where the finite elements size was reduced from 100 mm to 5 mm. Highlighted are the divergence phenomena.*

		100 mm	75 mm	50 mm	25 mm	20 mm	15 mm	10 mm	5 mm
Frequency [cycles/time or Hz]	1-4	0	0	0	0	0	0	0	0
	5	4.4	4.8	5.2	5.3	5.3	5.3	5.3	5.3
	6	6.0	6.1	6.2	6.2	6.2	6.2	6.2	6.2
	7	78.9	81.0	83.8	85.5	85.7	85.9	86.0	81.0
	8	160.1	166.6	175.7	181.4	182.1	182.6	148.9	86.0
	9	176.1	216.1	245.9	259.1	261.1	262.9	182.8	163.9
	10	223.9	240.8	264.0	278.5	280.4	281.7	264.2	182.8
	11	224.7	290.6	336.7	367.7	371.7	296.9	282.7	253.2
	12	254.6	301.7	386.8	430.9	437.7	374.3	292.0	264.8
	13	261.2	318.8	396.3	452.3	459.7	444.1	370.9	283.1
14	264.7	335.8	440.4	530.9	510.0	464.6	377.9	285.2	

Table 11: Numerical convergence verification for the first frequencies of vibration (in Hz or cycles per time) obtained for the curved panel, where the finite elements size was reduced from 100 mm to 5 mm. Highlighted are the divergence phenomena.

		100 mm	75 mm	50 mm	25 mm	20 mm	15 mm	10 mm	5 mm
Frequency [cycles/time or Hz]	1-4	0	0	0	0	0	0	0	0
	5	4.9	7.8	11.2	12.5	12.5	12.5	12.4	12.3
	6	15.4	15.6	15.5	15.4	15.3	15.3	15.2	15.1
	7	41.0	67.5	120.2	87.5	79.7	73.9	68.5	64.9
	8	87.3	118.6	121.0	163.7	165.3	163.7	154.2	147.7
	9	97.9	149.0	186.7	180.4	174.0	164.4	162.2	160.1
	10	176.0	196.5	203.3	188.0	181.8	183.0	182.0	179.8
	11	182.8	248.1	250.7	212.8	209.5	205.9	199.5	193.8
	12	214.8	288.8	364.2	309.3	289.1	274.5	260.8	251.4
	13	277.7	398.9	364.8	315.6	304.6	294.8	283.0	273.0
	14	278.8	400.0	365.4	335.3	319.3	306.3	290.8	279.3

From the two previous tables and by choosing the most refined mesh curve (i.e., the one obtained for finite elements with 5 mm size), it is possible to obtain the desired first frequencies of vibration and the respective vibration modes. It is important to refer that the dimension of the displacement witnessed by the vibration modes is given by the force and it is related with the amplitude of the sinusoidal function that excites the panel in first place. To obtain the real displacement dimensions on the vibration modes, the numerical model had to be simulated with the amplitude, which means that a Fortran routine had to be inserted, for the force action to be simulated as a function of time and for a set of values, for the final displacement to be presented. However, the shape for the first vibration modes is easily obtained in Abaqus for the flat and for the curved panels, whose results are given at *Appendix A7* and will be further discussed.

By opposition to the experimental results, the rigid body vibration modes and frequencies are easily obtained from the FEA. In respect to the rigid body vibration modes, it can be easily seen that both panels present six vibration modes, as it was expected and previously referred. However, what might be of notice is that, experimentally and numerically, as well as for both panels, two rigid body vibration modes present non-zero frequency values, which have values as high as 15.1 Hz. To explain this phenomenon, one must look to the Nylon fishing lines that support the panel. For reduced frequency values that go up to circa 20 Hz, both panels vibrate as rigid bodies. Experimentally, this fact is explained by the double pendulum vibration modes, which mean that the Nylon springs that hold the panel to the support beams are behaving as a first pendulum, whereas the panel itself is behaving as a second pendulum. Thus, the measured frequency value does not correspond to the real vibration of the structure, but it corresponds to the vibration of the Nylon springs that interferes with the structure itself. The bigger the Nylon spring length is, the lower the frequency of oscillation is. Numerically, the Nylon springs effect was simulated by the creation of soft springs in the numerical model, which are meant for the system to converge, instead of diverge. However, this convergence induces a numerical error on the measurement and presentation of the

frequencies for the rigid body vibration modes, through the solver used by Abaqus, Lanczos. Thus, the rigid body vibration modes assume values that can be higher than zero and go up to 10 Hz, 20 Hz or even more. Therefore, one is now able to accurately conclude that both panels present six rigid body vibration modes, half of them of translation and the other half of rotation along the three orthogonal axes. After these six rigid body vibration modes, the panel's first vibration modes occur.

When complex structures are considered, they might have several different local vibration modes, occurring at the same time and on different parts of the structure. However, when so called simple structures like a panel of this type is, usually the vibration modes can be classified as torsion or flexion on a specific direction. On this case, as the frequencies of vibration tend to increase, the non-linear effects assume also bigger relevancy, as it can be seen by the last vibration modes for each panel at *Appendix A7*. Therefore, only the shape of the first three vibration modes will be here analysed, by order of occurrence and for both panels. For the flat panel, the 1<sup>st</sup> vibration mode is the first torsion on the z or length axis, the 2<sup>nd</sup> is the first flexion on the y or width axis and finally the 3<sup>rd</sup> is the second torsion on the z or length axis. For the curved panel, the 1<sup>st</sup> vibration mode is again the first torsion on the z or length axis, the 2<sup>nd</sup> is the second torsion on the z or length axis and finally the 3<sup>rd</sup> is the first flexion on the y or width axis. Comparing both panels (and if one would analyse the remaining vibration modes), they experience the same vibration modes but sometimes by a different order of occurrence, as it happened with the 2<sup>nd</sup> and 3<sup>rd</sup> vibration modes, which are swapped. This is mainly due to the geometry of the panel, whereas the curved panel introduces directions in which it is easier to vibrate than the flat panel. Thus, the curved panel will experience earlier, vibration modes that occur later on the flat panel. Particularly on the curved panel and due to its geometry, on the 3<sup>rd</sup> vibration mode, a phenomenon called "saddle effect" occurs, whereas the flexion on the y or width axis occurs but it is not propagated to the middle of the panel, which creates a vibration mode shape similar to a horse saddle. This effect occurs due to the curvature of the panel (as it was already referred), but it occurs also particularly when the panel is thinner and the Poisson's Coefficient of the core material assumes values near to zero, which is this case.

Once again, since a convergence study was performed, a computational time analysis should also be carried out. However, since the behavior would be similar to one obtained for the compression test with the computational time increasing potentially with the increase of the number of finite elements, no detailed analysis will be referred.

### **4.2.3. Comparison between the experimental and the numerical results**

Having the FEA results from the numerical model, one is now able to compare the numerical results with the experimental, for both the flat (*Table 12*) and the curved (*Table 13*) panels. Since the first frequency of vibration occurs around 80 Hz for both panels and that, before this value, are the rigid body frequencies, on the further tables only the frequencies of vibration are compared.

Table 12: Comparison between the first frequencies of vibration (in Hz or cycles per time) obtained for the flat panels, where the deviation is shown, considering the experimental results as reference. Results are shown considering the experimental (column A) and the analytical (column B) properties for the skins.

		Experimental	Numerical A	Deviation [%]	Numerical B	Deviation [%]
Frequency [cycles/time or Hz]	3	74.5	81.0	8.71	76.8	3.11
	4	92.4	86.0	6.90	105.9	14.61
	5	175.7	163.9	6.70	164.8	6.21
	6	248.0	182.8	26.29	204.6	17.49
	7	262.7	253.2	3.62	259.4	1.24
	8	297.3	264.8	10.95	289.4	2.67
	9	341.7	283.1	17.15	304.8	10.79
	10	376.3	285.2	24.21	305.9	18.71

Table 13: Comparison between the first frequencies of vibration (in Hz or cycles per time) obtained for the curved panels, where the deviation is shown, considering the experimental results as reference. Results are shown considering the experimental (column A) and the analytical (column B) properties for the skins.

		Experimental	Numerical A	Deviation [%]	Numerical B	Deviation [%]
Frequency [cycles/time or Hz]	3	77.9	64.9	16.70	65.1	16.46
	4	171.0	147.7	13.61	158.5	7.29
	5	197.0	160.1	18.76	175.3	11.03
	6	213.3	179.8	15.73	187.0	12.35
	7	221.3	193.8	12.43	198.1	10.48
	8	251.0	251.4	0.16	266.1	6.01
	9	258.0	273.0	5.80	288.5	11.83
	10	294.7	279.3	5.23	291.8	0.99

From the results presented on *Table 12* and *Table 13*, it is possible to see that the deviation (considering the experimental results as reference) is generally lower for the first frequencies of vibration and higher for the last ones, when the flat panels are considered, whereas the opposite occurs for the curved panels. Even though the mean of the deviation considering all the numerical results is circa 14%, which is a high value, the numerical model validation can be seen through the behavior of the vibration modes. As it was stated before, the first 5 vibration modes were identified experimentally using a diapason and this procedure was performed for both panels. Thus, after the comparison with the first 5 vibration modes obtained numerically, one could see that the order in which the vibration modes occur, as well as their behavior and shape, was the same for all the first 5 frequencies of vibration and for both panels. Therefore, it is possible to conclude that, even though some numerically obtained frequency values presented a very high deviation when compared with their experimental value, the numerical model is again valid.



# 5. Conclusions

Planar and non-planar sandwich panels, with epoxy and glass fibers skins and agglomerated cork core, were tested experimentally and simulated numerically using Abaqus 6.13<sup>®</sup> FE program. For the simulation, both the core and the skins properties were determined analytically and experimentally. For the validation of the numerical model, compression and vibration tests were conducted and the experimental and numerical results were compared. Therefore, a study on the numerical model was conducted and the main conclusion that can be taken is that the final numerical model that was achieved is proved to be valid, when a flat or a curved panel with an agglomerated cork core are considered, though it has some limitations. As future developments, the numerical model and the panel configuration might be adapted to meet the specific requirements of the needed application. In this chapter, a few final considerations regarding the overall process of the current dissertation are explained and relevant further studies proposed by the author are given.

## 5.1. Achievements

The use of sandwich composites on engineering and particularly on aerospace has seen a major increase on the past few years. The use of different materials as new cores for sandwich composites is a matter still under development and certainly one of the most important quests into achieving the best sandwich configuration for the chosen application. Natural materials and its derivatives are of extreme importance, since they are eco-friendly and present rather special properties, such are the ones of agglomerated cork, particularly know for its hyperelastic behavior under compression, which was analysed on this dissertation. Cork and agglomerated cork composites are of extreme importance particularly for aerospace engineering, since they are already being used for the TPS of space vehicles and since they could replace the currently used foams or honeycomb cores on aircraft sandwich composites.

On an early stage of this dissertation, experimental tests were performed. First, the mechanical properties of both the skins and the core material were determined, when the material was subjected to different types of solicitations, following the applicable standards for the effect. After this tests were carried out, the results were compared with the available analytical solutions and one might conclude that the determined properties are according to what was expected, i.e., the skins are orthotropic and the core is isotropic. The discrepancies that exist between the experimental and the analytical solutions are mainly explained by the method of production and by the VIC software, from which the mean strains are computed.

After the determination of the material properties, the mechanical behavior of the total sandwich composite configuration was experimentally tested. Therefore, flat and curved panels were produced and they were subjected to compression and vibration tests. The available standards for the effect were reviewed, but they could not be entirely applied to these tests, due to the dimensions

of the panels and to the specific test requirements. From the experimental compression test, one might conclude that the flat panels are 6.75 times stiffer than the curved panels, but they withstand approximately 15% of the total displacement withstood by the curved panels (*Figure 51*). Since this test was performed until the panel's catastrophic failure, an analysis on the failure mechanisms could also be carried out and their behavior was identical, despite the type of panel tested. From the experimental vibration test, the frequencies of vibration for both panels were obtained and the vibration modes were determined experimentally using a diapason.

With the experimental tests performed, the numerical model was progressively developed until it has reached the final configuration widely described on this dissertation. The material properties determined analytically and experimentally were inserted on it, the conditions and interactions between the parts were defined and the FEA was carried out for both panels and for both tests. With the available software's functions, it is impossible to proper and accurately simulate the real non-linear mechanical behavior of agglomerated cork, used as core of the sandwich composite configuration.

Further more, the author of this dissertation states that it is impossible using the software's available functions to proper and accurately simulate the real behavior of materials similar to agglomerated cork, such as wood or bone, due to their non-linear and hyperelastic behavior, but particularly and mainly due to their cellular structure. Natural materials present random effects which are hardly to predict by the FE software. However, the achieved numerical model is proved to be valid for small displacements for both panels. For larger displacements, the non-linear effects are dominant and the geometry of the panel plays an important role on the results. With the available models provided by Abaqus and considering agglomerated cork, the best available hyperelastic model that fits the experimental data is the fifth order Ogden's strain energy potential (*Figure 43*). The software is unable to accurately account for the resin impregnation from the skins to the agglomerated cork core, which means that the real experimental core properties are different from the ones simulated by the FE software.

From the compression test, the numerical results obtained using the analytical properties for the skins are always more accurate than the ones obtained with their experimental properties. The panels with the analytical properties for the skins correspond to the purely analytical result and, since the FE program usually is more rigid than the reality, when the experimental properties are introduced, the slope of the linear curve is lower, which means that the panel is less rigid. When using the experimental properties for the skins, the resin impregnation and the warp of the panels play an important role.

From the vibration test, both panels present six rigid body vibration modes before the first vibration mode. Numerically and for both panels, two rigid body vibration modes present non-zero frequency values, which have values as high as 15.1 Hz, which is explained by the double pendulum vibration modes. The first 5 vibration modes were identified experimentally using a diapason and they appeared numerically on the same sequence for each type of panels. For the frequency values, the experimental and the numerical results were coherent, even though some numerically obtained frequency values presented a relatively high deviation when compared with their experimental

value. The curved panel presents its first vibration mode for frequencies lower than the ones witnessed for the flat panel, which is due to their geometry. Also for higher frequencies of vibration, the shape of the vibration modes changes from the flat to the curved panels, which is due to the curvature. When a panel is curved on one direction, it tends to vibrate easier on the direction of its curvature. Also, both panels tend to vibrate easier and for lower frequencies on the length direction than on the width, since their length is the double of their width.

Thus, the conclusion that can be taken from the compression and the vibration tests is that the achieved numerical model is proved to be valid for these types of tests and for both the flat and the curved panels. On a compression test, the behavior for smaller displacements is better simulated than it is for larger displacements. Improvements on the hyperelastic model to characterize the mechanical behavior of the agglomerated cork core should be taken, to achieve a better correlation between the experimental and the numerical results. However, the obtained results show the potential for the creation of numerical models to determine the mechanical behavior of these type of sandwich structures with cellular and non-linear cores, as a mean of validation of data obtained experimentally and, furthermore, as an alternative to the experimental tests themselves.

## 5.2. Future developments

As future developments on this topic, the author of this dissertation states the following aspects as the key issues that should be considered:

- The panel's production method could be improved, to reduce inaccuracies inherent to it. The hand lay-up process is a simple method, but a sandwich composite with the configuration of the one used should be expected to be symmetric and to present similar properties on its skins and core. However, this does not happen. As it can be seen from *Figure 38*, one skin of the panel tends to always get thicker than the other one. Besides this, effects such as the alignment of the glass fibers along the cork core, the amount of resin that is measured and even the warp of the panels are few of several effects that occur during both panel's production and which might lead to discrepancies between the experimentally tested panels and the ones simulated numerically.
- The analysis using VIC could be improved. The VIC software calculates the mean strain values in a way in which sometimes the strains appear noisy and with a higher projection error value. Factors such as the brightness of the images, the variation of the pattern and the presence of hot light sources have an important role on the accuracy of the strains calculated by the VIC. Even though these effects were minimized from the first experimental tests to the last ones, the author of this dissertation would like to deeply reduce this effects to their almost completely elimination.
- The numerical model could also be improved. A stochastic model for the resin impregnation on the agglomerated cork core should be created using Fortran and then inserted on the numerical model. This stochastic model would not be purely, but partially stochastic, since some variables present a fixed or easy to predict behavior, while others must be classified as non-deterministic, since their behavior can only be determined probabilistically and based on experimental results.

The author identifies the cellular structure of the cork cells and the resin impregnation amongst them as the key variables to be inserted on the stochastic model.

- A small-scale test correlation could be established, to achieve for the 1:1 scale panels, the same results that were achieved for the 1:3 scale panels, by extrapolation of the results given on this dissertation and by their proper validation.
- A parametric study on the best curvature configuration for the panel to be used on the referred application would also be of interest. For these type of studies, the author recommends the use of numerical models, since they allow for a faster and more comprehensive analysis.

Finally, while this dissertation has focused on the mechanical characterization of a curved panel, whose configuration was obtained from the inner fuselage of a jet plane, the proposed technology holds great promise for the real implementation on aircraft, as well as for the potential implementation on other types of applications. Therefore, the numerical model that was developed might be used and further improved to meet the requirements of the needed applications, whereas a flat or a curved panel is considered and whose core is made of a cellular, hyperelastic and non-linear material.

## 6. Bibliographic References

- [1] Lucas, A.; "Ancient Egyptian materials and industries about 1350 B.C."; *Summer Meeting, North of England Section* vol.58 (1933): 654-664.
- [2] Petras, A.; *Design of Sandwich Structures*, 1998.
- [3] "Some Failure Modes of Sandwich Walls" [Online].  
Available: <http://www.shellbuckling.com/> [Accessed: 17-Out-2016].
- [4] Broughton, W. R.; Crocker, L. E.; Gower, M. R. L.; (2002) *Design Requirements for Bonded and Bolted Composite Structures* (NPL Report MATC(A)65); Teddington, Middlesex; NPL Materials Centre, National Physical Laboratory.
- [5] Silva, S. P.; Sabino, M. A.; Fernandes, E. M.; Correlo, V. M.; Boesel, L. F.; Reis, R. L.; "Cork: properties, capabilities and applications"; *International Materials Reviews* vol.50 no.6 (2005): 345-365.
- [6] Gibson, L. J.; Easterling, K. E.; Ashby, M. F.; "The Structure and Mechanics of Cork"; *Proceedings of the Royal Society of London A* vol.377 no.1769 (1981): 99-117.
- [7] APCOR; *Cork Information Bureau*, 2015.
- [8] Mourão, T.; *Extraction of added value products from black condensate*, 2012.
- [9] Pereira, H.; *Cork: Biology, Production and Uses*, Lisbon: Elsevier Science, 2007.
- [10] Inwood, S.; *The Forgotten Genius: The Biography of Robert Hooke 1635-1703*, San Francisco, CA: Macadam Cage Pub, 2005.
- [11] Pereira, H.; Rosa, M. E.; Fortes, M. A.; "The Cellular Structure of Cork from *Quercus Suber* L."; *International Association of Wood Anatomists Journal* vol.8 no.3 (1987): 213-218.
- [12] Costa, A.; Pereira, H.; "Caracterização e Análise de Rendimento da Operação de Traçamento na Preparação de Pranchas de Cortiça para a Produção de Rolhas"; *Silva Lusitana* vol.12 no.1 (2004): 51-66.
- [13] Silva, J. M.; Gamboa, P. V.; Nunes, C.; Paulo, L.; Franco, N.; "Cork: Is it a good material for aerospace structures?"; *52nd AIAA/ASME/ASCE/AHS/ASC Structures, Structural Dynamics and Materials Conference* 2011-2159 (2011): 1-11.
- [14] "Main Applications" [Online].  
Available: <http://www.amorim.com/> [Accessed: 29-Sep-2016].
- [15] Bianchi, D.; *Modeling of ablation phenomena in space applications*, 2007.
- [16] "Shuttle's Cork From Portugal" [Online].  
Available: <http://www.nytimes.com/> [Accessed: 25-Mar-2016].
- [17] Thirkettle, A.; Steinkopf, M.; Joseph-Gabriel, E.; "The Mission and Post-flight Analysis of the Atmospheric Re-entry Demonstrator (ARD)"; *Esa Bulletin* vol.109 no.31 (2002): 55-63.
- [18] Tran, P.; Paulat, J. C.; Boukhobza, P.; "Re-entry Flight Experiments Lessons Learned – The Atmospheric Re-entry Demonstrator ARD"; *Nato RTO-EN-AVT-130* (2007): 1-46.

- [19] "ExoMars - 2016 Mission" [Online].  
Available: <http://www.russianspaceweb.com/> [Accessed: 24-Mar-2016].
- [20] "ExoMars Trace Gas Orbiter and Schiaparelli Mission (2016)" [Online].  
Available: <http://www.exploration.esa.int/> [Accessed: 24-Mar-2016].
- [21] "ExoMars 2016 – The heat is on!" [Online].  
Available: <https://www.airbusdefenceandspace.com/> [Accessed: 23-Mar-2016].
- [22] "ExoMars 2016 Schiaparelli Descent Sequence" [Online].  
Available: <http://www.exploration.esa.int/> [Accessed: 24-Mar-2016].
- [23] "Premières images des boucliers thermiques d'ExoMars 2016" [Online].  
Available: <http://www.futura-sciences.com/> [Accessed: 25-Mar-2016].
- [24] "Put a cork in it" [Online].  
Available: <http://www.udel.edu/> [Accessed: 27-Apr-2016].
- [25] Castro, O.; Silva, J. M.; Devezas, T.; Silva, A.; Gil, L.; "Cork agglomerates as an ideal core material in lightweight structures"; *Elsevier Materials and Design* vol.31 no.1 (2010): 425–432.
- [26] "Design of Environment Friendly Structures for Aircraft" [Online].  
Available: <http://www.desair.inegi.up.pt/> [Accessed: 07-Nov-2016].
- [27] "Design of Environment Friendly Structures for Aircraft" [Online].  
Available: <http://www.almadesign.pt/> [Accessed: 07-Nov-2016].
- [28] "Amorim Cork Composites" [Online].  
Available: <http://www.amorimcorkcomposites.com/> [Accessed: 14-Mar-2016].
- [29] Amorim Cork Composites; *Technical Data Core Cork*; 2009.
- [30] "Resinas Castro" [Online].  
Available: <http://www.resinascastro.es/> [Accessed: 04-Sep-2016].
- [31] "Epoxy Systems" [Online].  
Available: <http://www.resoltech.com/> [Accessed: 04-Sep-2016].
- [32] "Resoltech 1050 Resin" [Online].  
Available: <http://www.resoltech.com/> [Accessed: 04-Sep-2016].
- [33] "Steel CNC Router" [Online].  
Available: <http://www.ouplan.net/> [Accessed: 17-Aug-2016].
- [34] US Department of Defense; *Composite Materials Handbook - Volume 1: Polymer Matrix Composites - Guidelines for Characterisation of Structural Materials*; Composite Materials Handbook Series vol. 1; 2002.
- [35] Reddy, J. N.; *Mechanics of Laminated Composite Plates and Shells - Theory and Analysis*; Boca Raton, FL: CRC Press, 2<sup>nd</sup> edition; 2004.
- [36] Chamis, C. C.; Sinclair, J. H.; "Ten-deg Off-axis Test for Shear Properties in Fiber Composites"; *Society for Experimental Mechanics Journal* vol.17 no.9 (1977): 339–346.
- [37] Chandy, R.; Pattison, G.; "Using ASTM Method C297, Flatwise Tensile Strength, as an Indicator of Resin Acrylic-Bonding-Potential for Tub and Shower Laminates"; Composites 2006 Convention and Trade Show, St. Louis, MO (2006).

- [38] Jardin, R.; Pereira, A. B.; "Static and dynamic mechanical response of different cork agglomerates"; Elsevier Materials and Design vol.68 (2015): 121-126.
- [39] "Abaqus 6.13 Analysis User's Guide" [Online].  
Available: <http://www.129.97.46.200:2080.com/> [Accessed: 06-Nov-2016].
- [40] "Stainless Steel : Tables of Technical Properties" [Online].  
Available: <http://www.worldstainless.org/> [Accessed: 06-Oct-2016].
- [41] Johnston, B.; Cornwell, M.; Beer, F. P.; *Vector Mechanics for Engineers Statics and Dynamics*; New York, NY: McGraw-Hill, 9th edition; 2010.
- [42] "Strength Testing of Various Fishing Lines for River Fishing" [Online].  
Available: <http://www.shimadzu.com/> [Accessed: 30-Oct-2016].
- [43] "HexForce™ 7725 Product Data" [Online].  
Available: <http://www.hexcel.com/> [Accessed: 22-Nov-2016].
- [44] Walleberger, F. T.; Watson, J. C.; Li, H.; "Glass Fibers"; *ASM Handbook Composites* vol.21 no.19 (2001): 27-34.
- [45] Clarke, J.; *Structural Design of Polymer Composites: Eurocomp Design Code and Background Document*; London: E & FN Spon, Chapman & Hall, 1<sup>st</sup> edition; 1996.
- [46] "MicroLab" [Online].  
Available: <http://microlab.ist.utl.pt/> [Accessed: 19-Sep-2016].
- [47] Ricardo, J.; *Structural Modelling Validation of Cork Composites for Aeronautical Applications*; 2009.



# 7. Appendixes

## 7.1. Appendix A1

On this section an overview is given on the INSTRON machines and its software, the VIC cameras and its software and the correlation program.

For the mechanical testing of the composites, two different machines were used: **INSTRON 3369** and **INSTRON 5566**. The two different machines were used only due to the availability of the tabs and needed equipment. However, both machines operate on the same way and provide the same software, **BLUEHILL**. After turning the machine on, placing the right tabs and the specimen and opening the software, the test method is created, where parameters as the velocity of the test or the end of test criterions are chosen. None of the values inputted for these parameters will be explained on this section, since they vary according to the type of test performed. Also, the test method developed depends on the type of test needed. It is however important to refer that raw data files, the test curves and other needed values are outputted from the program, as soon as the test is performed, and they will be the ones used for further analysis.

Visual Image Correlation or **VIC** is a method, which consists of a set of digital cameras that capture consecutive images of a specimen undergoing a mechanical test, to evaluate how the characteristics of its surface change. The images taken by the cameras consist then on the data that is going to be analysed by the software, which runs a mathematical correlation analysis. It is important to refer that, whenever a two-dimensional view of the specimen is needed, just one camera has to be used and the software used was **VIC-2D 2009**. On the other hand, whenever a three-dimensional view of the specimen is needed, two cameras have to be used and the software used was **VIC-3D 2012**. The method followed for the set-up, calibration and focusing of the cameras, as well as for all the needed cable connections between them, the power source and the laptop, were performed according to the manufacturer's *Testing Guide*. The post-analysis and the understanding of the user interface, were entirely conducted according to the best options justified on the manufacturer's *Reference Manual*. Therefore, these topics will be only shortly discussed.

To prepare the specimen for this method, a random pattern of points (also known as speckle pattern) has to be created on the surface of the specimen that is going to be visible by the cameras. This process was made by painting the entire specimen with a white colour spray and then by placing dots with a black colour spray. After this, the specimen is ready to be tested on the machine. For calibration purposes (and after the application of the preload, if needed), five snaps of the specimen are taken using the VIC software. However, when using VIC-3D, the calibration process is slightly different from the one used in VIC-2D. Thus, a grid that approximately fills the field of view must be used and ten to twenty snaps of its translations and rotations along the three axes have to be taken. For this purpose, it was used a 12×9 dots grid, where the horizontal and the vertical distance between any two points is 15 mm (*Figure 54*). On the program, after calibrating the scale, the obtained score must be equal or less to 0.099 in order for the calibration to be accurate.

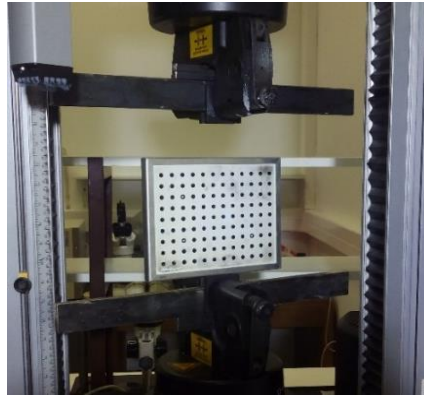


Figure 54: Grid pattern used for the VIC-3D analysis.

After this, the **VIC-Snap** software is open and the timed capture option selected, where the acquisition interval for the snaps is chosen. Then, the start button is pressed and snaps start to be taken according to the time interval inputted, at the same time as the INSTRON machine performs the desired test on the specimen. At the end of the test, a set of ten to twenty calibration images are obtained, as well as five initial images that will correspond to the reference images and all the deformed images taken throughout the test. All the deformed images, by comparison with the reference images, present different dot patterns. Using the computer software to correlate all the pixels of the deformed images with the ones from the first reference images, a strain map is generated for the previously selected area of interest (*Figure 55*). Several aspects were taken into consideration, such as the step and the subset values, as well as the correlation and post-processing options. For the effect, Gaussian weights were used for the subset, with an optimized 8-tap interpolation using normalized squared differences. The Von-Mises strain was also computed using a Lagrange deformation tensor, with a decay filter of size 15. It is important to refer that the analysis using VIC is performed using the Newton-Raphson method, whereas the deformation of image speckles is calculated by the change in the vertical and in the horizontal distance between two points, from the current image in relation to the previous one. This concept is performed to all points inside the area of interest created and it corresponds to the strain. During the analysis, the projection error was kept inferior to 0.1, which means that the correlation from one snap to the next one is accurate. After the analysis, the statistics can be exported as an Excel file and used for further calculations.

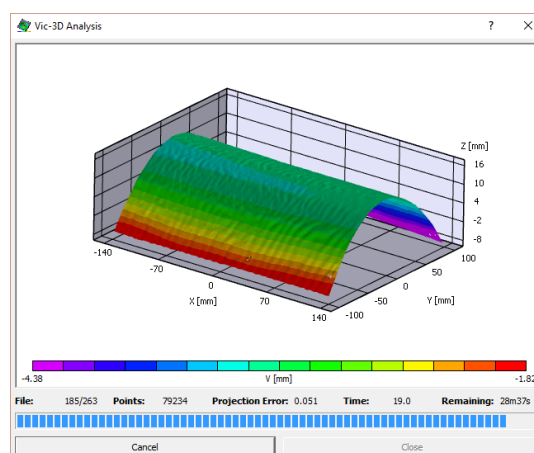


Figure 55: VIC-3D analysis for one of the curved panel's specimens.

Nowadays, video image correlation using digital cameras is one of the best options for strain measurement. For this thesis, VIC is the best option for two main reasons. The first one is the fact that it is a non-intrusive method, which means that there is no need for example to place an extensometer on the specimen, which would introduce uncertainties and create a rigid zone on the specimen. In addition, an extra concentrated force is not applied on the specimen. The second one is that it allows for a wide range of analysis, which are impossible with, for example, an extensometer. Its easy set-up and easy transport are also an advantage that reinforces the choice of this method.

Finally, the **Python 3.5 correlation program** connects the results from the INSTRON with the ones from the VIC. From VIC, one obtains a file with values of mean displacements and strains, calculated from one snap to the other, and with a determined time interval. On the other hand, from INSTRON, one obtains a file with values of the machine displacement and applied load, with a different time interval. Thus, the time correlation program synchronizes both values of time and outputs the load-displacement or the stress-strain curves. After the analysis, an excel file and a graph with the introduced load-displacement or stress-strain values already synchronized are outputted.

## 7.2. Appendix A2

On this section the determination of the skins properties is given, whose purpose is for them to be introduced on the numerical model, for the FEA to be as accurate as possible.

### 7.2.1. Analytical Values

Considering the referred theory for an orthotropic material from [35], for the determination of the analytical values for the nine independent material coefficients, since we are considering a slender bar which is axially loaded, the resulting stress and strain satisfy the Hooke's Law, until the elastic limit of the material is reached. As first approximation, the material is considered as both homogeneous and isotropic, i.e., its mechanical properties are independent of both position and direction. From this consideration, the strains must have the same value for any transverse direction. Thus, considering the data provided by the manufacturer as the foundation for the analytical results obtinence, the needed main properties stated before might be determined (*Table 14*).

*Table 14: Properties of the matrix and the fibers, according to the manufacturers [32] [43] [44].*

Matrix, index 'M' (Epoxy Resin 1050/1058S)		Fibers, index 'F' (300 g/m <sup>2</sup> Glass Fibers)	
$W_M$ [kg]	$1.632 \times 10^{-3}$	$W_F$ [kg]	$1.192 \times 10^{-3}$
$\rho_M$ [kg/m <sup>3</sup> ]	1 120	$\rho_F$ [kg/m <sup>3</sup> ]	1 242
$E_M$ [MPa]	3 460	$E_F$ [MPa]	69 000
$\nu_M$	0.30	$\nu_F$	0.22

First, the volume of both the fibers and the matrix can be calculated:

$$\begin{cases} V_F = \frac{W_F}{\rho_F} = \frac{1.192 \times 10^{-3}}{1\,242} = 0.96 \times 10^{-6} \text{ m}^3 \\ V_M = \frac{W_M}{\rho_M} = \frac{1.632 \times 10^{-3}}{1\,120} = 1.45 \times 10^{-6} \text{ m}^3 \end{cases} \quad (\text{Equation 15})$$

The analytical density of the composite can now be calculated from the previous results:

$$\rho_C = \frac{W_C}{V_C} = \frac{W_F + W_M}{V_F + V_M} = \frac{(1.192 + 1.632) \times 10^{-3}}{(0.96 + 1.45) \times 10^{-6}} = 1\,169 \text{ kg/m}^3 \quad (\text{Equation 16})$$

It is known that, in each layer of fabric, the total volume fraction rarely exceeds 40%. However, for bidirectional twill weave fabrics and other similar fabrics, the effective fibre fraction in either the warp or the weft directions is unlikely to exceed 20% [45]. Therefore, for one direction, the volume fraction of the fibers  $f$  must be divided by two:

$$f = \frac{\left(\frac{V_F}{V_F + V_M}\right)}{2} = \frac{\frac{0.96 \times 10^{-6}}{(0.96 + 1.45) \times 10^{-6}}}{2} = 0.199 \quad (\text{Equation 17})$$

According to [35] and from pages 86-89, the analytical Young's Modulus is calculated from the rule of mixtures, where nor the effect of voids nor the interface effects are considered, i.e., they assume that the interface between the matrix and the load is perfect. Therefore, the Young's Modulus can be calculated by the Voigt Model (also known as the Rule of Mixture "ROM" model), which is based on the isodeformation condition. It considers that the deformation of the matrix (index 'M') and the deformation of the fibers (index 'F') are equal to the deformation of the total composite

(index 'C'), meaning that  $\varepsilon_M = \varepsilon_F = \varepsilon_C$ . So, the stresses are given by  $\sigma_C = \sigma_F V_F + \sigma_M V_M$  and, by the Hooke's Law, the analytical Young's Modulus of the composite (along the longitudinal direction, index 'x') can be calculated from the Young's Modulus of each component and the volumetric fraction:

$$E_x = E_F f + E_M(1 - f) = 69\,000 \times 0.199 + 3\,460 \times (1 - 0.199) = 16\,533 \text{ MPa} \quad (\text{Equation 18})$$

Also, the analytical Shear Modulus for the fibers and the resin matrix can be calculated from:

$$\begin{cases} G_F = \frac{E_F}{2(1+\nu_F)} = \frac{69\,000}{2 \times (1+0.22)} = 28\,279 \text{ MPa} \\ G_M = \frac{E_M}{2(1+\nu_M)} = \frac{3\,460}{2 \times (1+0.30)} = 1\,331 \text{ MPa} \end{cases} \quad (\text{Equation 19})$$

Now the analytical Shear Modulus can be calculated from the previous results:

$$G_{xy} = \frac{G_F G_M}{G_F(1-f) + G_M f} = \frac{28\,279 \times 1\,331}{28\,279 \times (1-0.199) + 1\,331 \times 0.199} = 1\,643 \text{ MPa} \quad (\text{Equation 20})$$

Also, the analytical Poisson's Coefficient can be calculated from:

$$\nu_{xy} = \nu_F \cdot f + \nu_M \cdot (1 - f) = 0.22 \times 0.199 + 0.30 \times (1 - 0.199) = 0.284 \quad (\text{Equation 21})$$

## 7.2.2. Experimental Values

### *Tensile test*

For the tensile test performed using the skins material, the dimensions and respective densities of the specimens are given on *Table 15*.

*Table 15: Dimensions, weight and density calculation of the tangentially oriented specimens (T1 to T7) and of the axially oriented specimens (A1 to A7), sectioned for the skins material tensile test. The relative error for the calculated density is shown on the last column, by comparison with the analytical value of 1 169 kg/m<sup>3</sup>.*

Specimen	Length <i>l</i> [mm]	Width <i>w</i> [mm]	Thickness <i>t</i> [mm]	Area <i>A</i> [mm <sup>2</sup> ]	Weight <i>W</i> [g]	Density $\rho$ [kg/m <sup>3</sup> ]	Relative Error [%]
T1	200	20.29	0.46	9.33	2.78	1 487	27.20
T2	200	20.16	0.54	10.89	2.76	1 266	8.30
T3	200	20.13	0.51	10.27	2.48	1 207	3.25
T4	200	20.32	0.53	10.77	2.57	1 193	2.05
T5	200	20.41	0.50	10.14	2.78	1 372	17.37
T6	200	19.86	0.51	10.13	2.97	1 468	25.58
T7	200	19.72	0.53	10.52	2.96	1 407	20.40
A1	200	19.96	0.52	10.38	2.78	1 337	14.37
A2	200	19.93	0.51	10.17	2.76	1 356	16.00
A3	200	20.28	0.49	10.01	2.48	1 238	5.90
A4	200	20.17	0.52	10.56	2.57	1 217	4.11
A5	200	19.52	0.53	10.34	2.78	1 345	15.06
A6	200	20.30	0.47	9.61	2.96	1 540	31.74
A7	200	20.47	0.45	9.28	2.85	1 534	31.22

After the tensile test is performed, the stress-strain curves for the tangential and axial directions are obtained (*Figure 56*) and the Young's Modulus can be determined through a linear regression on each one of the obtained curves (*Table 16*).

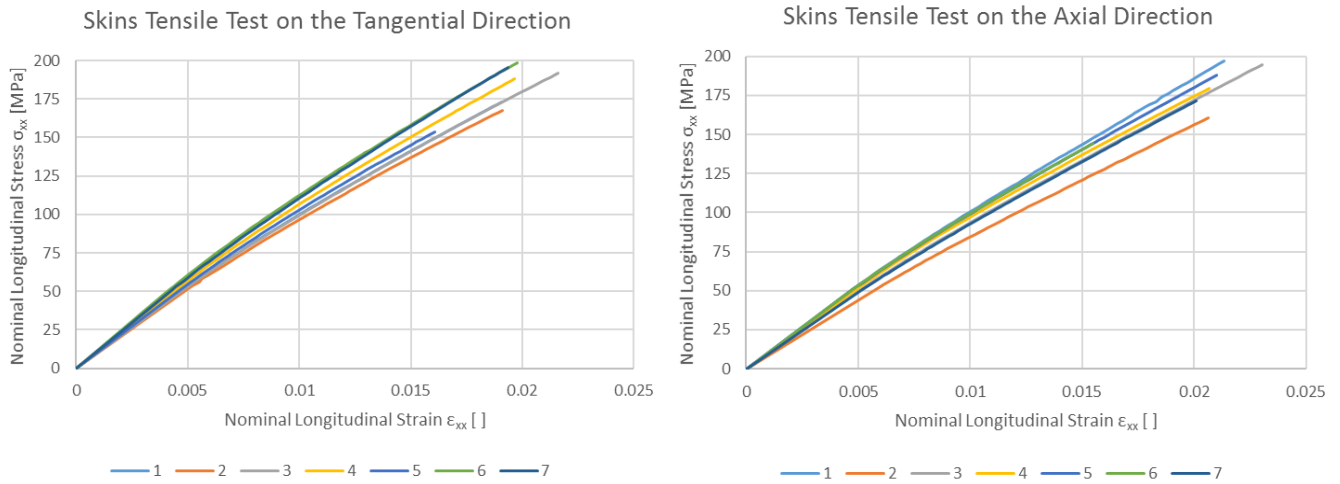


Figure 56: Stress-strain curves obtained for the tensile tested specimens oriented on the tangential axis (left) and on the axial axis (right).

Table 16: Young's Modulus ( $E_x$ ) and Coefficient of Determination ( $R^2$ ) values obtained for each specimen and for both the tangential (up) and the axial (down) directions. Mean values are shown in the last column.

	T1	T2	T3	T4	T5	T6	T7	Mean
$E_x$ [MPa]	9 406	9 217	9 280	10 038	9 961	10 551	10 510	9 852
$R^2$	0.983	0.984	0.983	0.982	0.985	0.980	0.987	-
	A1	A2	A3	A4	A5	A6	A7	Mean
$E_x$ [MPa]	9 520	8 025	8 774	9 085	9 338	9 700	8 853	9 042
$R^2$	0.981	0.980	0.982	0.969	0.980	0.980	0.980	-

After the tensile test is performed, also the transversal strain-longitudinal strain curves for the tangential and axial directions can be obtained (*Figure 57*) and the Poisson's Coefficient can be again determined through a linear regression on each one of the obtained curves (*Table 17*).

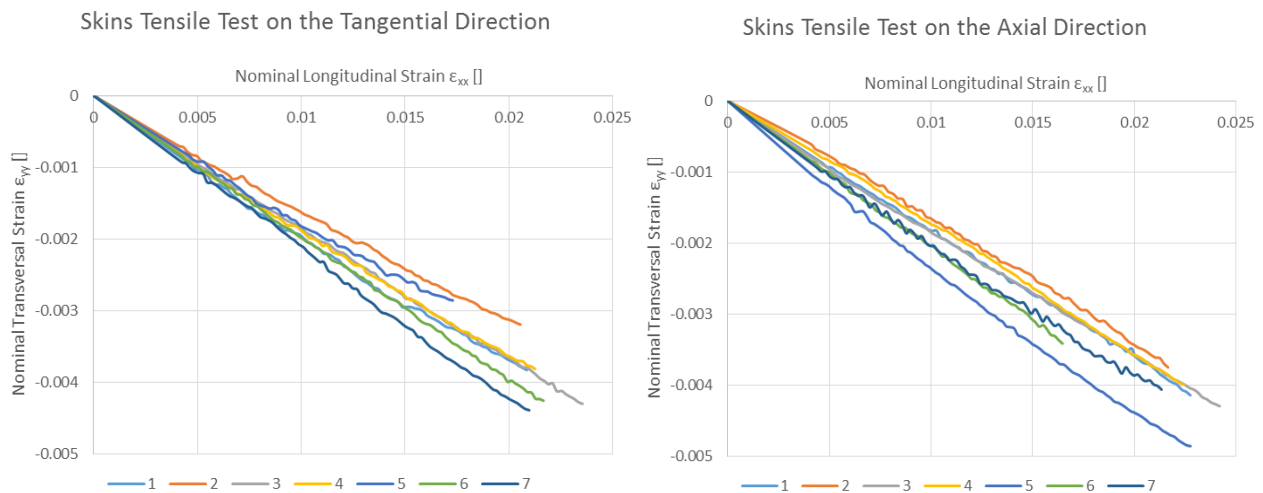


Figure 57: Transversal strain-longitudinal strain curves obtained for the tensile tested specimens oriented on the tangential axis (left) and on the axial axis (right).

Table 17: Poisson's Coefficient ( $\nu_{xy}$ ) and Coefficient of Determination ( $R^2$ ) values obtained for each specimen and for both the tangential (up) and the axial (down) directions. Mean values are shown in the last column.

	T1	T2	T3	T4	T5	T6	T7	Mean
$\nu_{xy}$ [ ]	0.1926	0.1601	0.1844	0.1849	0.1744	0.1981	0.2131	0.1916
$R^2$	0.990	0.997	0.999	0.997	0.990	0.999	0.999	0.999
	A1	A2	A3	A4	A5	A6	A7	Mean
$\nu_{xy}$ [ ]	0.1807	0.1681	0.1799	0.1762	0.2242	0.2061	0.1974	0.1911
$R^2$	0.999	0.997	0.998	0.998	0.992	0.999	0.995	0.999

### Ten-deg off-axis tensile test

For the 10° off-axis tensile test performed using the skins material, the dimensions and respective densities of the specimens are given on Table 18.

Table 18: Dimensions, weight and density calculation of the 10° off the tangential axis oriented specimens (10oT1 to 10oT7) and of the 10° off the axial axis oriented specimens (10oA1 to 10oA7), sectioned for the skins material tensile test. The relative error for the calculated density is shown on the last column, by comparison with the analytical value of 1 169 kg/m<sup>3</sup>.

Specimen	Length $l$ [mm]	Width $w$ [mm]	Thickness $t$ [mm]	Area $A$ [mm <sup>2</sup> ]	Weight $W$ [g]	Density $\rho$ [kg/m <sup>3</sup> ]	Relative Error [%]
10oT1	200	20.39	0.52	10.60	2.65	1 250	6.93
10oT2	200	20.77	0.54	11.29	2.71	1 202	2.82
10oT3	200	20.53	0.52	10.75	2.71	1 263	8.04
10oT4	200	20.81	0.57	11.86	2.71	1 140	2.48
10oT5	200	20.93	0.51	10.60	2.62	1 236	5.73
10oT6	200	20.83	0.5	10.41	2.50	1 202	2.82
10oT7	200	20.45	0.51	10.36	2.58	1 246	6.59
10oA1	200	20.32	0.5	10.16	2.59	1 276	9.15
10oA2	200	20.27	0.43	8.65	2.62	1 517	29.77
10oA3	200	19.55	0.44	8.60	2.42	1 407	20.36
10oA4	200	20.45	0.54	10.97	2.58	1 176	0.60
10oA5	200	20.27	0.51	10.41	2.57	1 233	5.47
10oA6	200	19.21	0.45	8.58	2.35	1 371	17.28
10oA7	200	20.02	0.47	9.47	2.43	1 280	9.50

After the 10° off-axis tensile test is performed, the stress-strain curves for the tangential and axial directions are obtained (Figure 58) and the Shear Modulus can be determined through a linear regression on each one of the obtained curves (Table 19).

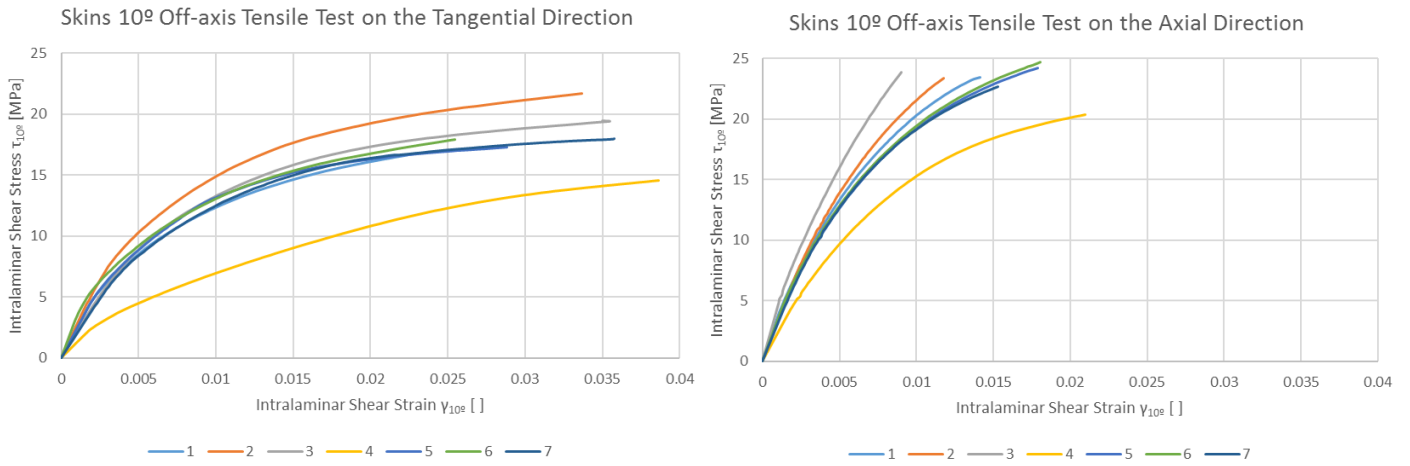


Figure 58: Stress-strain curves obtained for the specimens oriented  $10^\circ$  off the tangential axis (left) and  $10^\circ$  off the axial axis (right).

Table 19: Shear Modulus ( $G$ ) and Coefficient of Determination ( $R^2$ ) values obtained for each specimen and for both the tangential (up) and the axial (down) directions. Mean values are shown in the last column.

	T1	T2	T3	T4	T5	T6	T7	Mean
$G_{xy}$ [MPa]	1 942	2 301	1 906	1 013	1 983	2 195	1 809	1 878
$R^2$	0.886	0.942	0.983	0.932	0.912	0.770	0.976	-
	A1	A2	A3	A4	A5	A6	A7	Mean
$G_{xy}$ [MPa]	2 901	2 988	3 498	2 066	2 753	2 813	2 726	2 821
$R^2$	0.949	0.974	0.946	0.972	0.959	0.944	0.969	-

## 7.3. Appendix A3

On this section the determination of the core properties is given, whose purpose is again for them to be introduced on the numerical model, for the FEA to be as accurate as possible.

### 7.3.1. Experimental values

#### *Compression test*

For the compression test performed using the core material, the dimensions and respective densities of the specimens are given on *Table 20*.

*Table 20: Dimensions, weight and density calculation of the radially oriented specimens (R1 to R7), of the tangentially oriented specimens (T1 to T7) and of the axially oriented specimens (A1 to A7), sectioned for the core material compression test. The relative error for the calculated density is shown on the last column, by comparison with the analytical value of 200 kg/m<sup>3</sup> [29].*

Specimen	Length $l$ [mm]	Width $w$ [mm]	Thickness $t$ [mm]	Area $A$ [mm <sup>2</sup> ]	Weight $W$ [g]	Density $\rho$ [kg/m <sup>3</sup> ]	Relative Error [%]
R1	19.38	21.82	22.44	489.53	1.65	173	13.30
R2	19.44	22.62	19.96	451.28	1.53	174	13.08
R3	19.56	20.43	20.69	422.49	1.41	170	14.99
R4	19.51	20.53	21.12	433.49	1.51	179	10.73
R5	19.43	21.24	20.44	434.04	1.49	176	11.96
R6	19.46	20.55	20.39	419.01	1.51	185	7.71
R7	19.45	20.24	21.44	433.74	1.56	184	7.81
T1	19.63	20.18	20.14	395.35	1.56	200	0.18
T2	19.62	20.07	21.54	422.41	1.67	202	0.78
T3	19.52	19.69	21.56	420.65	1.65	200	0.20
T4	19.58	19.97	21.32	417.35	1.60	195	2.41
T5	19.58	20.66	21.47	420.18	1.73	210	4.86
T6	19.60	19.63	21.78	426.68	1.68	200	0.17
T7	19.69	20.26	22.23	437.50	1.75	203	1.31
A1	19.42	19.56	21.45	379.76	1.69	229	14.27
A2	19.32	21.62	21.26	417.59	1.85	229	14.68
A3	19.24	21.20	20.63	407.79	1.55	198	1.22
A4	19.54	21.80	20.60	425.97	1.56	187	6.59
A5	19.58	20.92	20.73	409.41	1.58	197	1.74
A6	19.64	21.05	20.13	413.32	1.46	179	10.36
A7	19.48	21.60	20.90	420.77	1.56	190	5.14

After the compression test is performed, the stress-strain curves for all directions are obtained (*Figure 59*). The average stress-strain curve for each direction is simply obtained through the mean of the stress-strain curve obtained for each one of the seven tested specimens (*Figure 60*).

Comparing the obtained curves and using the Final curve as reference, for the first values the deviation is around 30% for both the radial and axial directions and less than 10% for the tangential direction. However, this value decreases considerably and for nominal compressive strains higher than 17% for the axial direction and 22% for the radial direction, this error is less than 10%. Therefore, the material is isotropic and the Final stress-strain curve from *Figure 60* can be accurately used for simulating the core material properties under compression.

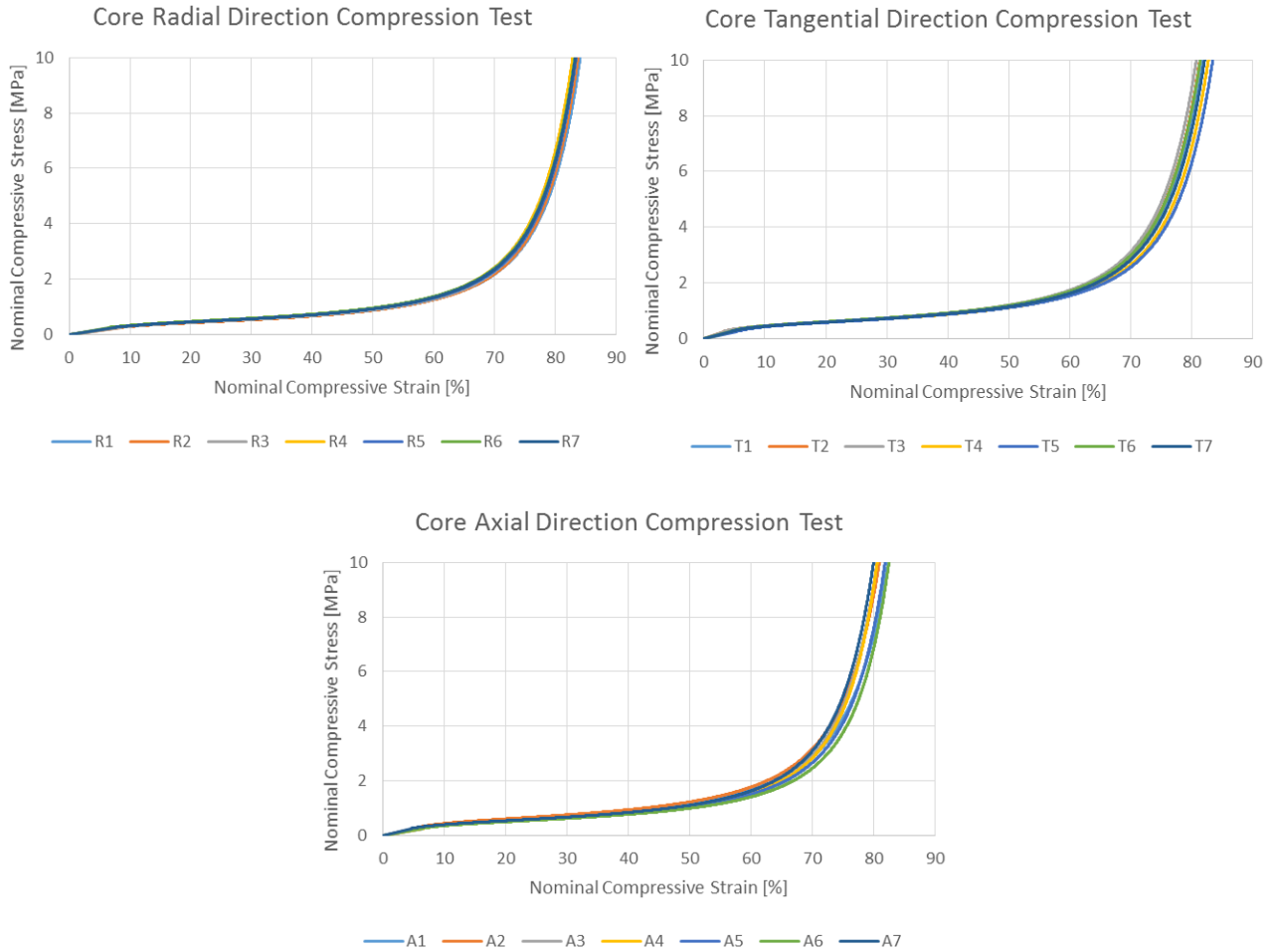


Figure 59: Stress-strain curves obtained for the specimens oriented on the radial axis (up, left), on the tangential axis (up, right) and on the axial axis (down, centre).

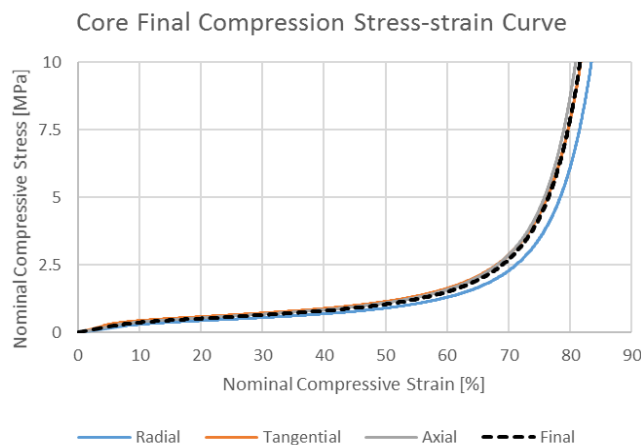


Figure 60: Average stress-strain curves obtained from Figure 59 and for each one of the three directions.

## Tensile test

For the tensile test performed using the core material, the dimensions and respective densities of the specimens are given on *Table 21*.

*Table 21: Dimensions, weight and density calculation of the radially oriented specimens (R1 to R7), of the tangentially oriented specimens (T1 to T5) and of the axially oriented specimens (A1 to A5), sectioned for the core material tensile test. The relative error for the calculated density is shown on the last column, by comparison with the analytical value of 200 kg/m<sup>3</sup> [29].*

Specimen	Length $l$ [mm]	Width $w$ [mm]	Thickness $t$ [mm]	Area $A$ [mm <sup>2</sup> ]	Weight $W$ [g]	Density $\rho$ [kg/m <sup>3</sup> ]	Relative Error [%]
R1	51.31	49.96	19.40	2563.28	9.21	185.26	7.37
R2	51.57	51.62	19.58	2662.04	9.66	185.31	7.34
R3	51.47	51.03	19.68	2626.86	9.63	186.37	6.82
R4	51.40	50.22	19.64	2581.31	9.72	191.86	4.07
R5	51.68	52.11	19.62	2693.04	10.38	196.45	1.77
R6	51.07	50.60	19.49	2584.14	10.01	198.84	0.58
R7	50.94	51.94	19.52	2646.00	9.50	183.89	8.05
T1	200	19.68	5.00	98.30	4.73	240.38	20.19
T2	200	20.42	5.03	102.59	4.93	240.12	20.06
T3	200	19.75	5.03	99.36	4.82	242.76	21.38
T4	200	20.21	5.03	101.56	4.94	243.22	21.61
T5	200	19.27	4.99	96.16	4.73	245.95	22.98
A1	200	20.11	5.02	100.94	4.74	234.95	17.48
A2	200	19.54	5.02	98.09	4.51	229.69	14.84
A3	200	19.59	5.02	98.24	4.45	226.48	13.24
A4	200	20.12	4.975	100.08	4.462	222.92	11.46
A5	200	20.20	4.99	100.81	4.609	228.59	14.29

After the tensile test is performed, the stress-strain curves for all directions are obtained (*Figure 61*). The average stress-strain curve for each direction is simply obtained through the mean of the stress-strain curve obtained for each one of the seven tested specimens (*Figure 62*). Comparing the obtained curves and using the Final curve as reference, here occurs the opposite that happens for the core compression curves: for the first values, the deviation is under 10% for all directions and, the higher the nominal strain value, the bigger the deviation verified. For nominal strains, higher than 2%, the error is already higher than 10% for all directions and it is around 30% for the radial direction for nominal strains higher than 7%, whereas it is only circa half of this value for the other two directions. Therefore, it is possible to conclude that the strain calculation on the radial direction is not accurately made using the vertical displacement of the machine. Therefore, and due to the already verified isotropy of the core material under compression and due to the almost perfect correlation verified between the tensile tests performed along the tangential and axial directions, the radial curve can be excluded from the final average stress-strain curve calculation. With this conclusion, the deviation is always less than 10% for all nominal strains previously referred.

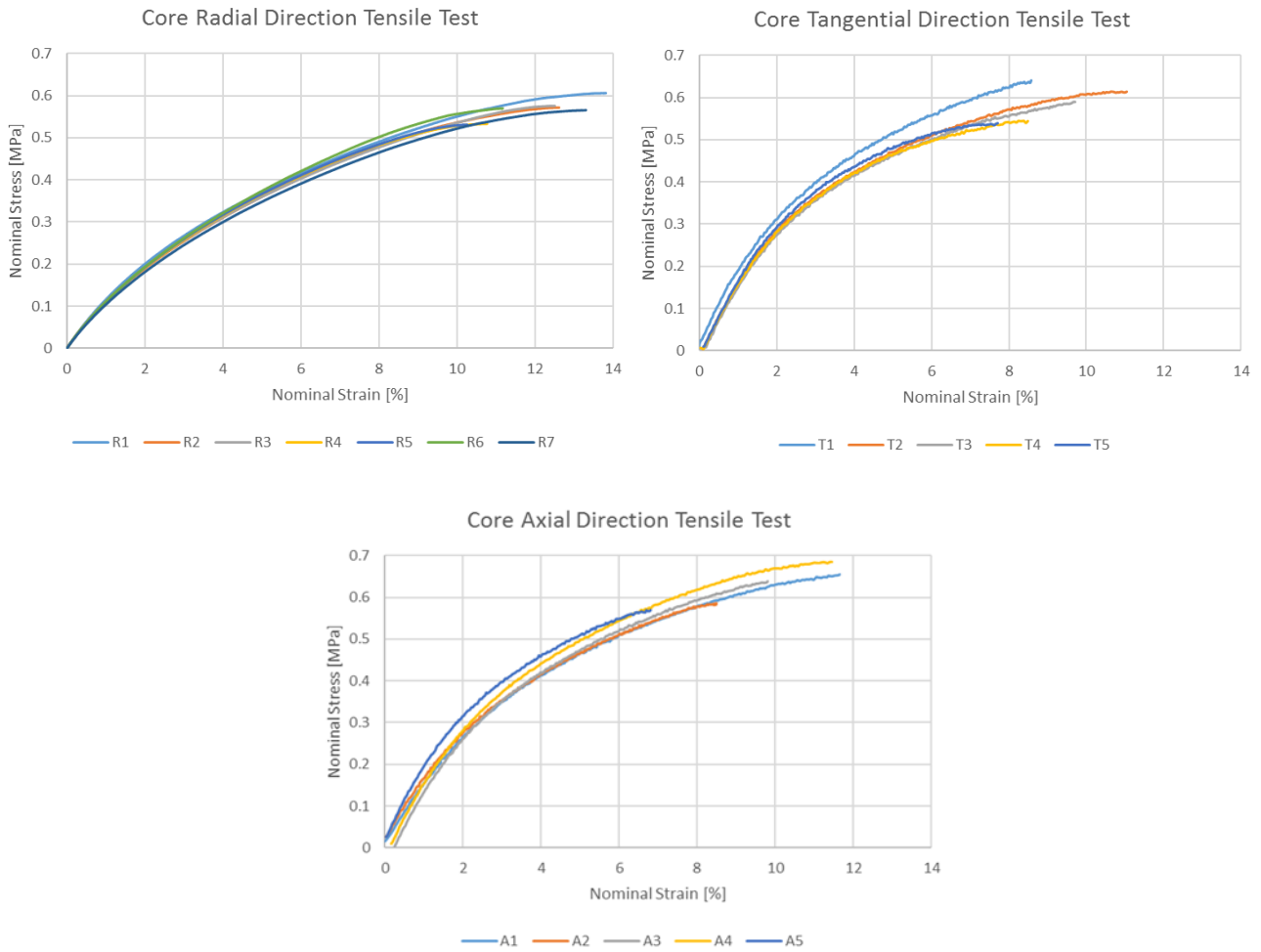


Figure 61: Stress-strain curves obtained for the specimens oriented on the tangential axis (left) and on the axial axis (right).

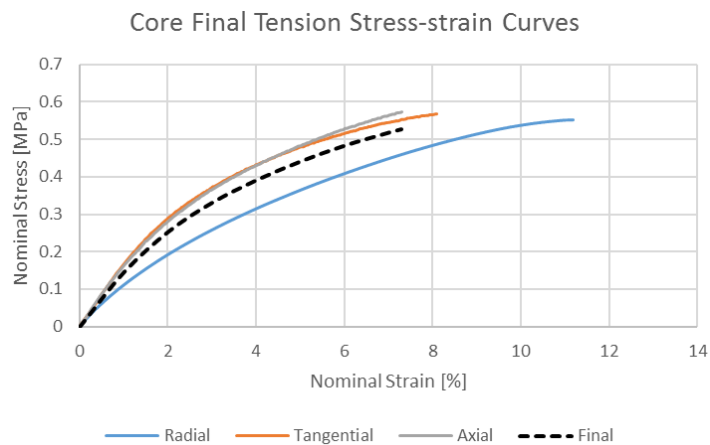


Figure 62: Average stress-strain curves obtained for each one of the three directions.

## 7.4. Appendix A4

On this section are presented the flat and curved panels dimensions and densities, analytically and experimentally determined (*Table 22*).

Knowing that the density of the skins is  $\rho_s = 1\,169\text{ kg/m}^3$  (see *Appendix A2* for details) and the density of the core is  $\rho_c = 200\text{ kg/m}^3$  (see *Appendix A3* for details), considering a flat panel the volume is given by:

$$V = lwt \quad (\text{Equation 22})$$

So, the volume of the skins is  $V_s = 0.450 \times 0.225 \times 5 \times 10^{-4} = 5.063 \times 10^{-5}\text{ m}^3$  and the volume of the core is  $V_c = 0.450 \times 0.225 \times 5 \times 10^{-3} = 5.063 \times 10^{-4}\text{ m}^3$ . The weight is given by:

$$W = \rho V \quad (\text{Equation 23})$$

So, the weight of the skins is  $W_s = 1\,169 \times 5.063 \times 10^{-5} = 5.919 \times 10^{-2}\text{ kg}$  and the weight of the core is  $W_{core} = 200 \times 5.063 \times 10^{-4} = 1.013 \times 10^{-1}\text{ kg}$ . The total weight and volume of the panel are given respectively by  $W_p = W_c + 2W_s = 2.196 \times 10^{-1}\text{ kg}$  and  $V_p = V_c + 2V_s = 6.076 \times 10^{-4}\text{ m}^3$ .

Therefore, the analytical density of the panel is given by:

$$\rho_p = \frac{W_p}{V_p} = \frac{2.196 \times 10^{-1}}{6.076 \times 10^{-4}} = 361.50\text{ kg/m}^3 \quad (\text{Equation 24})$$

*Table 22: Dimensions, weight and density calculation of flat panel's (0-1 to 0-3) and the curved panel's (38-1 to 38-3) specimens, sectioned for the vibration and compression tests. The relative error for the calculated density is shown on the last column, by comparison with the analytical value of  $361.50\text{ kg/m}^3$  [29].*

Specimen	Length $l$ [mm]	Width $w$ [mm]	Thickness $t$ [mm]	Area $A$ [mm <sup>2</sup> ]	Weight $W$ [g]	Density $\rho$ [kg/m <sup>3</sup> ]	Relative Error [%]
0-1	451.17	225.50	5.40	1217.70	267.10	486.18	34.49
0-2	452.33	226.83	5.11	1159.12	271.78	518.35	43.39
0-3	453.67	227.67	5.02	1142.89	271.36	523.37	44.78
38-1	451.83	224.33	5.73	1285.43	272.07	468.44	29.58
38-2	450.50	224.33	5.57	1249.54	272.72	484.48	34.02
38-3	450.67	224.17	5.53	1239.64	270.15	483.56	33.77

From the results of *Table 22*, it is important to refer that the experimental densities are usually higher than the analytical ones and that the relative error is relatively high for its values. This occurs essentially due to several analytical assumptions, such as the assumption that all the tested specimens are rectangular and have fixed dimensions, which experimentally does not occur.

## 7.5. Appendix A5

On this section, the experimental amplitude and phase diagrams are shown for the first flat panel (*Figure 63*) and for the first curved panel (*Figure 64*), obtained after the vibration test.

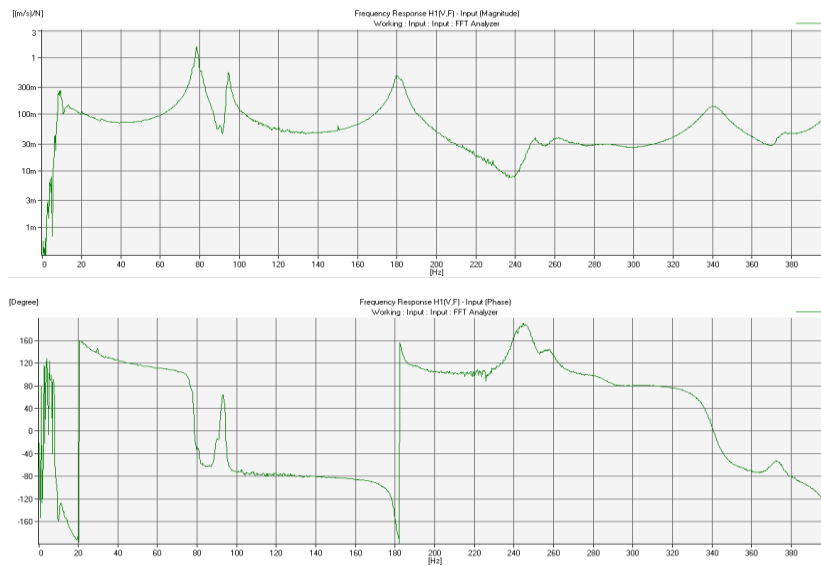


*Figure 63: Amplitude (up) and phase (down) diagrams, obtained for the first flat panel specimen under a vibration test.*

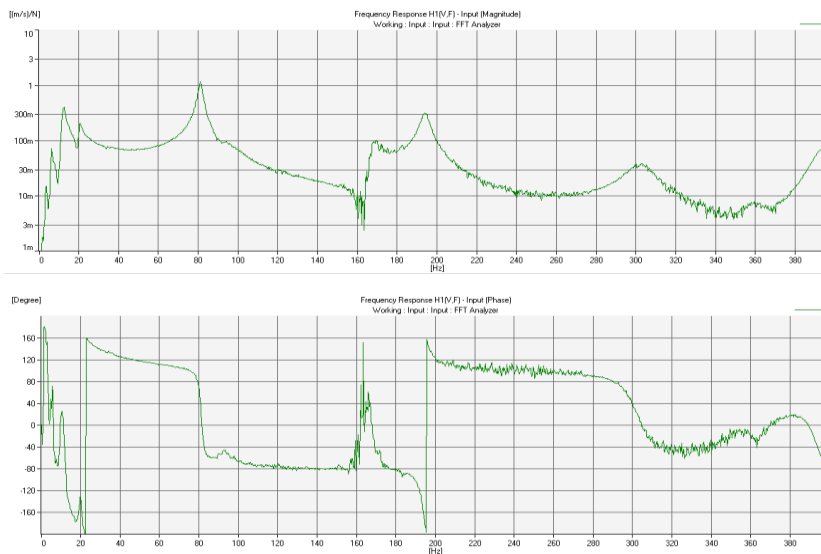


*Figure 64: Amplitude (up) and phase (down) diagrams, obtained for the first curved panel specimen under a vibration test.*

## 7.6. Appendix A6

On this section, an overview of the sandwich composite microstructure is performed, using the data obtained from the analysis using the scanning electron microscope (SEM).

For the SEM analysis, small specimens of the final sandwich composite with a length  $\times$  width of  $15 \times 5$  mm were produced. The SEM possesses a focused beam of electrons, which interact with the specimen's atoms. The result of these multiple interactions are signals that contain information about the specimen's topography and composition, which are then shown in the computer (*Figure 65*).



*Figure 65: Analytical SEM Hitachi S2400 at IST's MicroLab [46].*

From the SEM images, which were taken with amplifications from  $\times 25$  up to  $\times 800$ , it is possible to identify clearly the glass fibers, the epoxy resin and the cork cells that compose the agglomerated cork core (*Figure 66*). The difference between some nucleuses of several cork cells can also be seen, as well the corrugated cells at their border. These nucleuses are the macroscopically seen granules. Also, the orientation of the several nucleuses of cork cells is aleatory and different from one granule to the other, which is a result of the manufacturing process of the agglomerated cork described at *Chapter 2* and which sustains the core's isotropy. Although these conclusions were already referred on *Chapter 3*, the images obtained from the SEM are their definite confirmation.

With a major influence on the core's properties, the resin impregnation on the agglomerated cork core of the sandwich composite might also be observed. Resin impregnation has already been identified as a possible effect occurring on sandwiches with cork core, where its thickness was circa 6 mm [47]. However, the author of this dissertation does not know of any other research work, in which the existence or the absence of this effect is actually proved. However, by analysing the SEM results, one is able to see clearly that the epoxy resin introduced on the skins during the composite's production process, flows into the empty interstices between the cork granules and into some cork cells, strengthening the core of the composite and changing its properties. This phenomenon occurs mainly during the cure process and the pressure application, where the impregnation thickness and ratio is completely aleatory and hard to predict. Thus, what really happens is that the core is no longer made only of agglomerated cork, but of agglomerated cork plus the impregnated epoxy resin, whose distribution is aleatory and non-uniform. In addition, due to the composite's reduced thickness of

circa 6 mm, there are parts where the resin impregnates throughout the entire composite's thickness, which means that all the cells on the core are filled with impregnated resin.

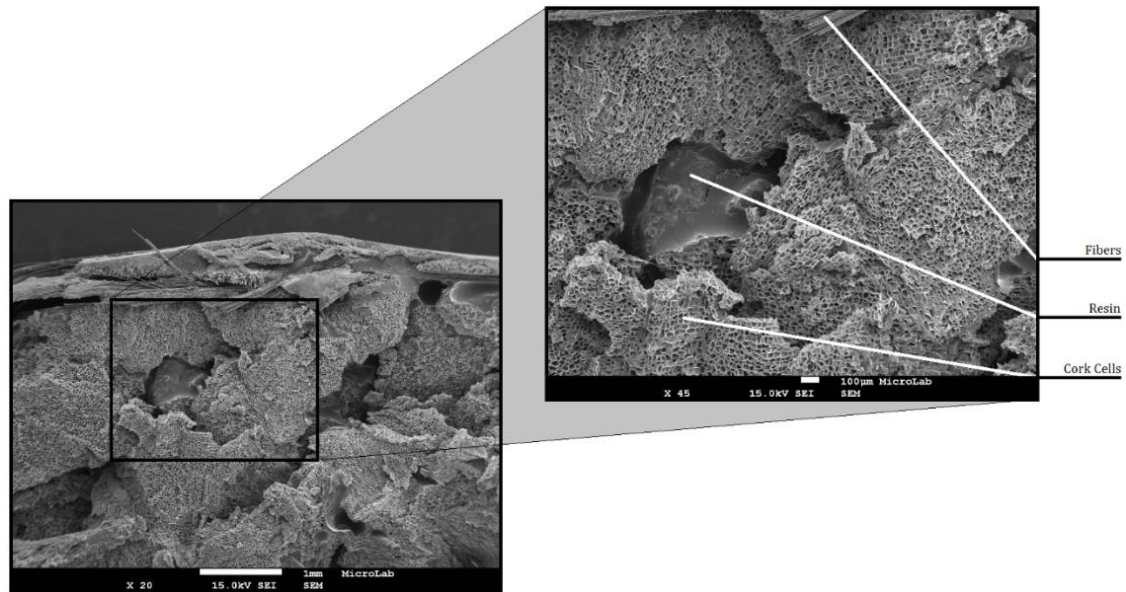


*Figure 66: Overview along the composite's thickness next to the top skin and under an amplification of  $\times 20$  and  $\times 45$ , where the fibers, the resin and the cork cells are identified.*

The bigger the core thickness is, the more random the impregnation effects tend to be, which means that more difference will exist between the experimental and the numerical results. On the other hand, when the thickness of the core is way smaller than 5 mm, the resin impregnates easier from one skin to the other, which means that the core will be mainly made of agglomerated cork with impregnated epoxy resin. This conclusion is somewhat opposite to the one given to the specimens tested with a core thickness of 0.8 mm on reference [47], in which it is stated that “the overall results (...) indicate less pronounced discrepancies, which suggests a less pronounced effect of epoxy resin upon the core”. For the author of this dissertation, the conclusion given at reference [47] is the opposite from what in reality happens. The smaller the thicknesses of the core are, the more pronounced the resin impregnation on the core's cells is, which makes the core almost homogeneously and completely made of agglomerated cork impregnated with epoxy resin. This homogeneity will then reduce the random effects that introduce discrepancies between the experimental and the numerical results, which assume more importance as the core gets thicker.

## 7.7. Appendix A7

On this section, the six rigid body and the first eight vibration modes are represented for both the flat (*Figure 67 to Figure 73*) and the curved (*Figure 74 to Figure 80*) panels, with the respective numerical frequency value. It is important to refer that the further results were simulated using the experimentally determined properties for the skins on the numerical model. All the vibration modes further referred present meshes with elements of 5 mm, where the panel with the grey mesh and common to all figures, is the one representing the panel at its initial state.

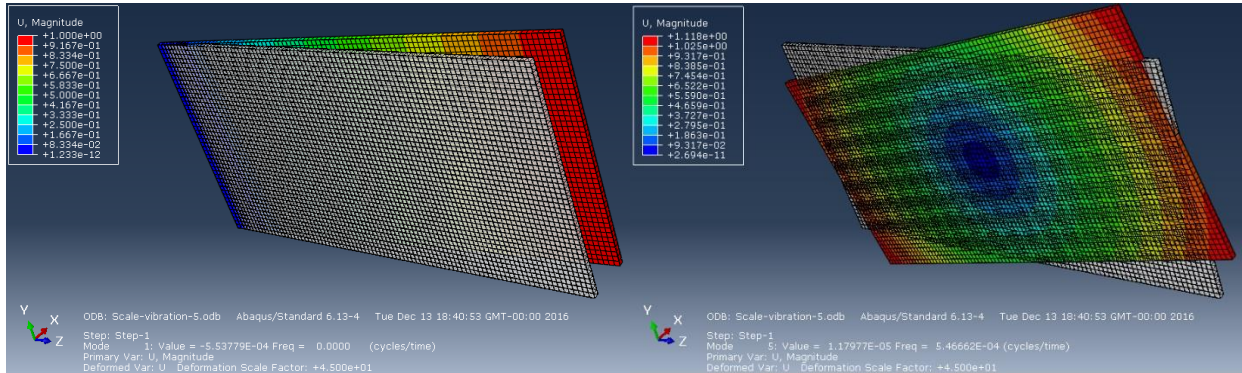


Figure 67: x axis translation (left) and x axis rotation (right), rigid body vibration modes for the flat panel.

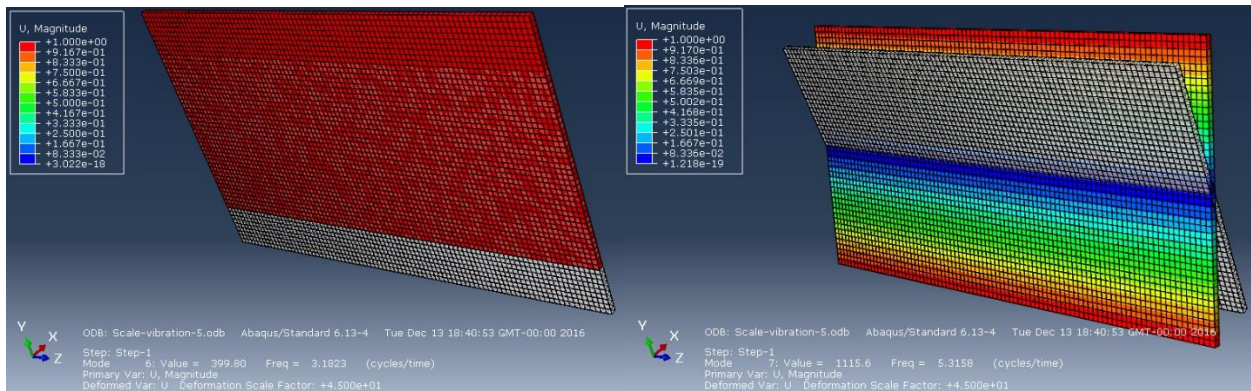


Figure 68: y axis translation (left) and z axis rotation (right), rigid body vibration modes for the flat panel.

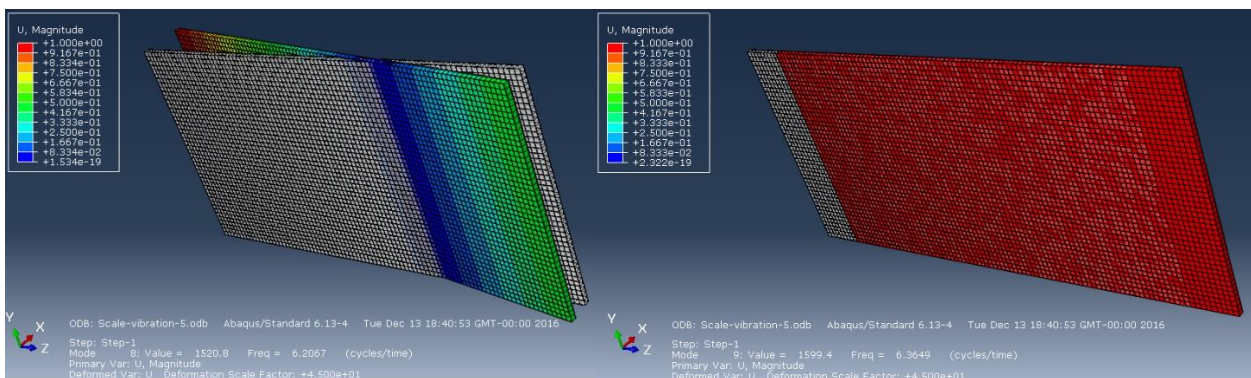


Figure 69: y axis rotation (left) and z axis translation (right), rigid body vibration modes for the flat panel.

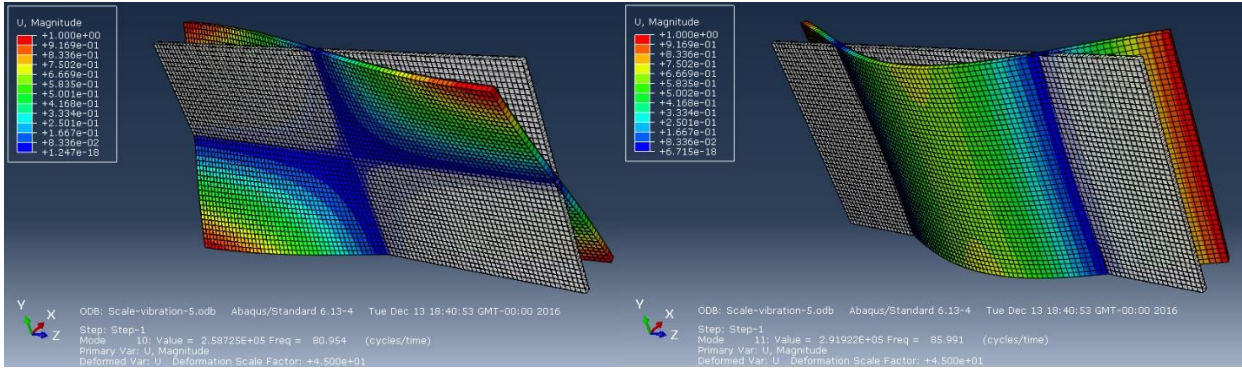


Figure 70: 1<sup>st</sup> (left) and 2<sup>nd</sup> (right) vibration modes for the flat panel.

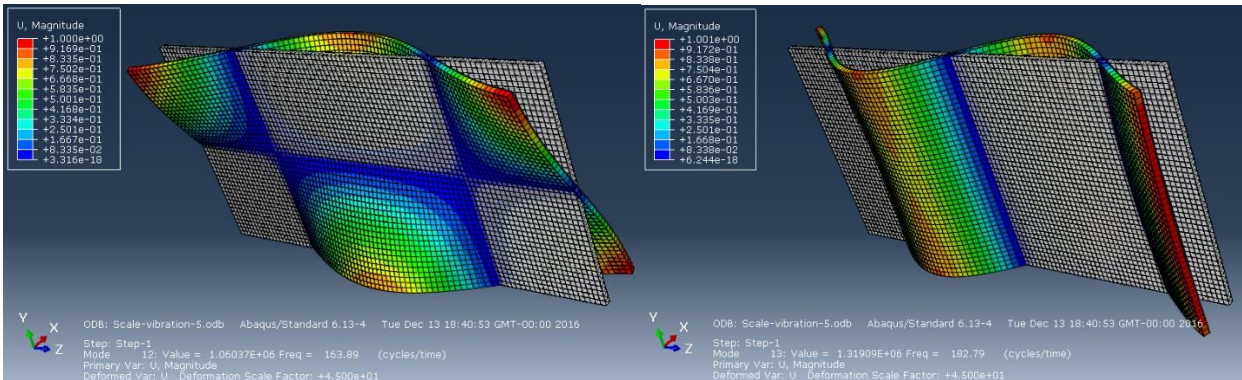


Figure 71: 3<sup>rd</sup> (left) and 4<sup>th</sup> (right) vibration modes for the flat panel.

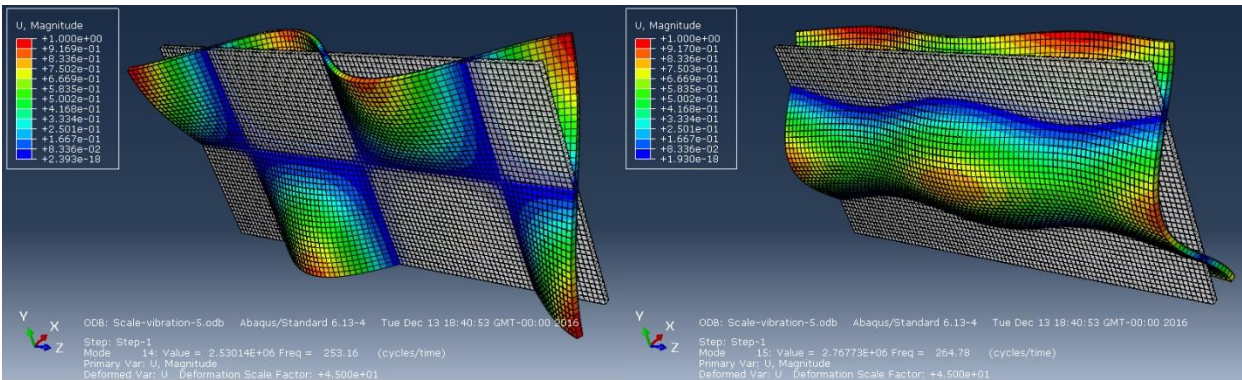


Figure 72: 5<sup>th</sup> (left) and 6<sup>th</sup> (right) vibration modes for the flat panel.

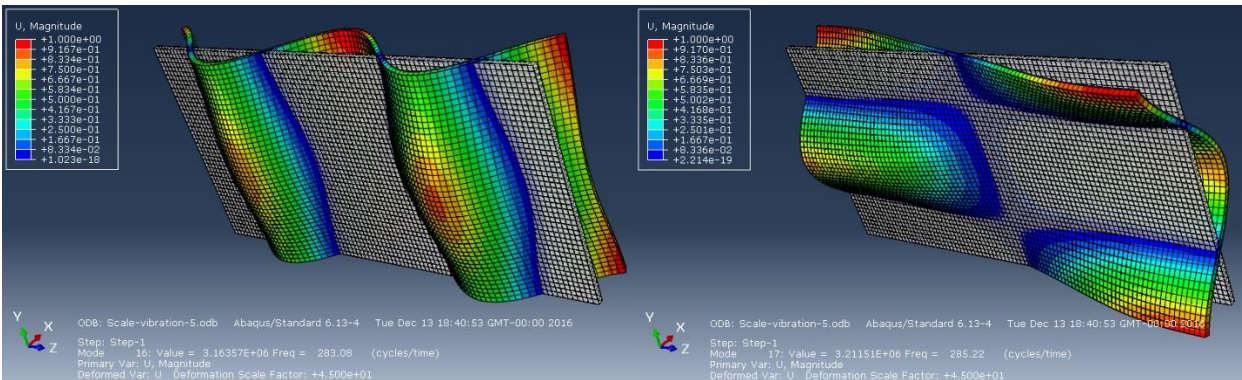


Figure 73: 7<sup>th</sup> (left) and 8<sup>th</sup> (right) vibration modes for the flat panel.

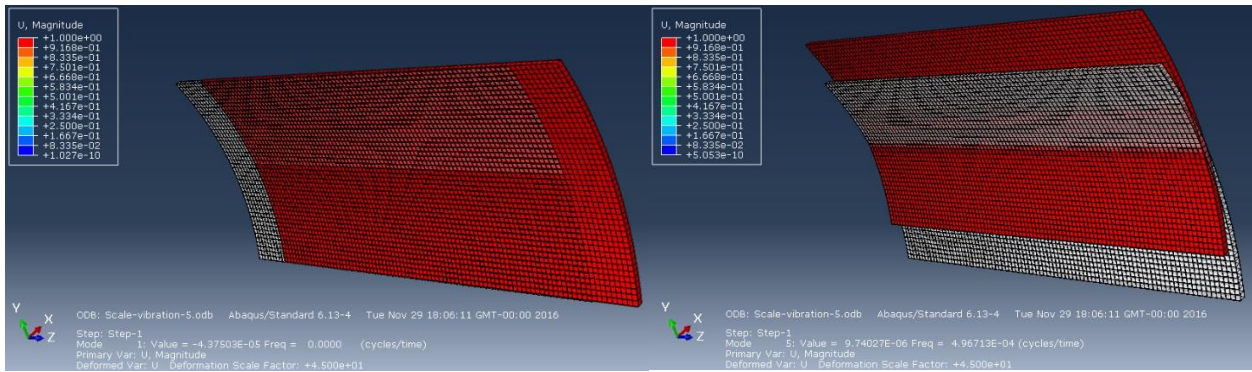


Figure 74: z axis translation (left) and y axis translation (right), rigid body vibration modes for the curved panel.

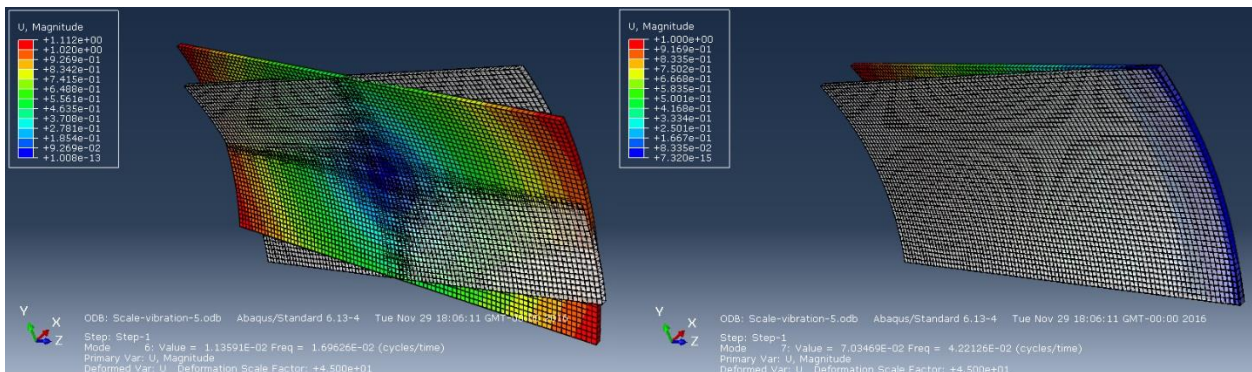


Figure 75: x axis rotation (left) and x axis translation (right), rigid body vibration modes for the curved panel.

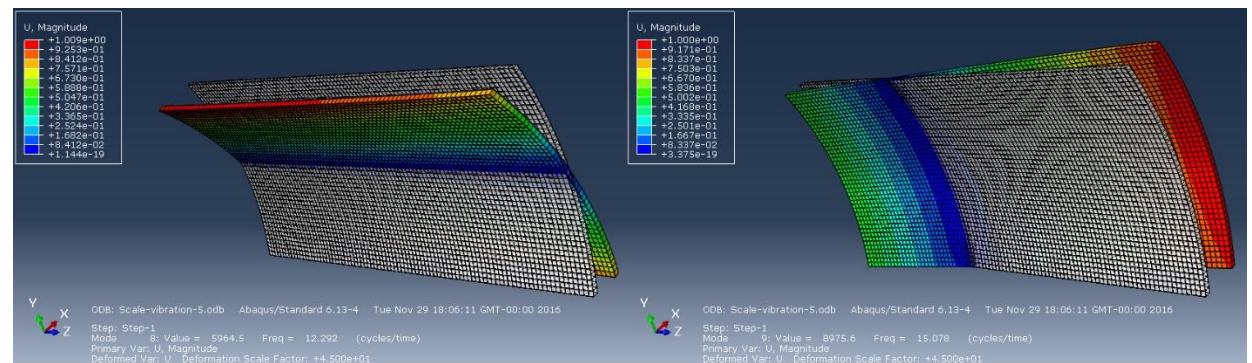


Figure 76: z axis rotation (left) and y axis rotation (right), rigid body vibration modes for the curved panel.

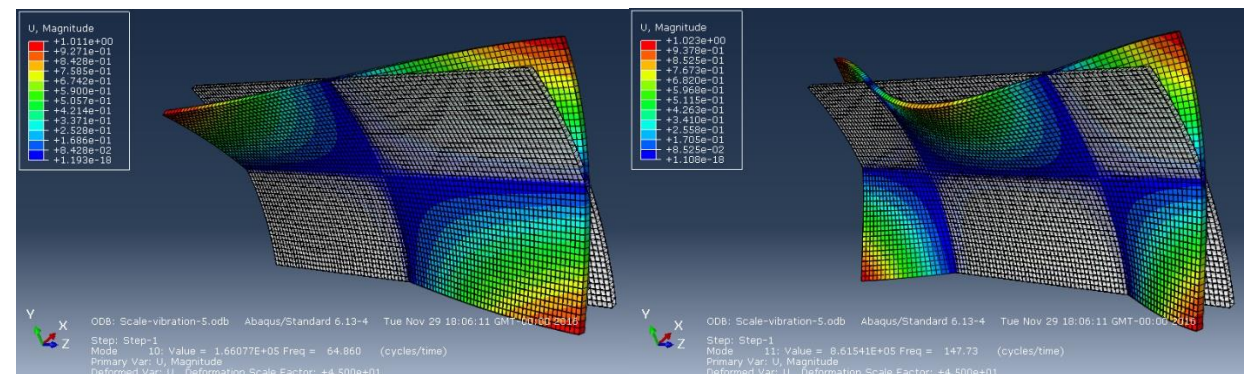


Figure 77: 1<sup>st</sup> (left) and 2<sup>nd</sup> (right) vibration modes for the curved panel.

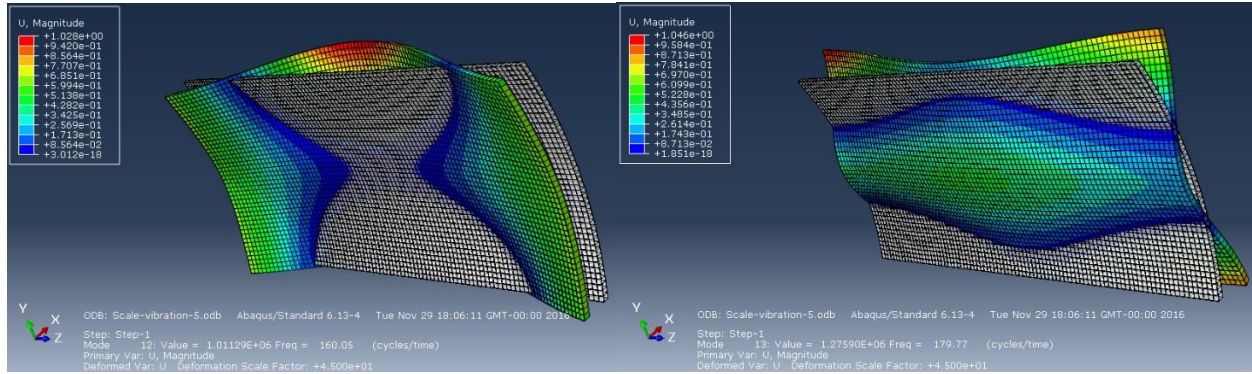


Figure 78: 3<sup>rd</sup> (left) and 4<sup>th</sup> (right) vibration modes for the curved panel.

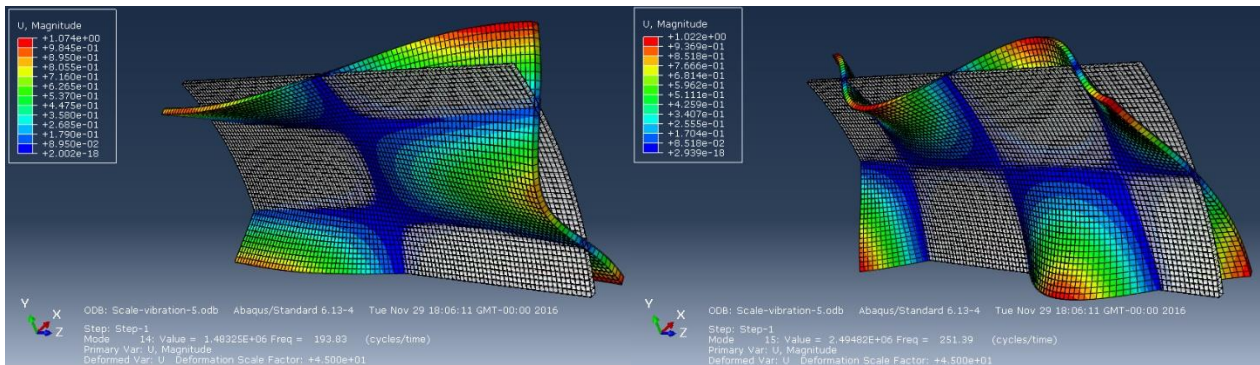


Figure 79: 5<sup>th</sup> (left) and 6<sup>th</sup> (right) vibration modes for the curved panel.

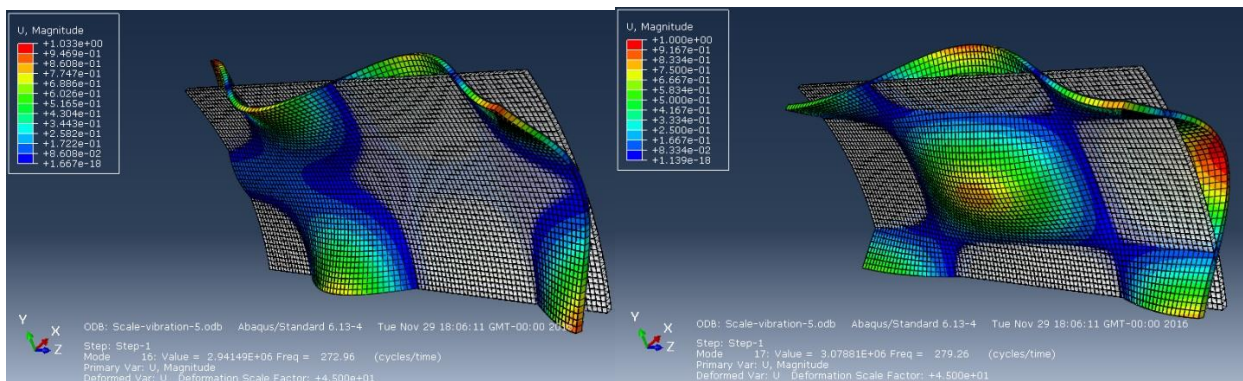


Figure 80: 7<sup>th</sup> (left) and 8<sup>th</sup> (right) vibration modes for the curved panel.



